

École doctorale n° 364 : Sciences Fondamentales et Appliquées

Doctorat ParisTech

THÈSE

pour obtenir le grade de docteur délivré par

l'École Nationale Supérieure des Mines de Paris

Spécialité doctorale “Science et Génie des Matériaux”

présentée et soutenue publiquement par

Ali SAAD

le xx juin 2015

NUMERICAL MODELLING OF MACROSEGREGATION FORMED DURING SOLIDIFICATION WITH SHRINKAGE USING A LEVEL SET APPROACH

Directeurs de thèse: **Michel BELLET**
Charles-André GANDIN

Jury

M. Blablabla ,	Professeur, MINES ParisTech	Rapporteur
M. Blablabla ,	Professeur, Arts Et Métiers ParisTech	Rapporteur
M. Blablabla ,	Chargé de recherche, ENS Cachan	Examinateur
M. Blablabla ,	Danseuse, en freelance	Examinateur
M. Blablabla ,	Ingénieur, MIT	Examinateur

T
H
E
S
S
E

Acknowledgement

Dedicated to humanity ...

Contents

1 General Introduction	1
1.1 Solidification notions	2
1.1.1 Solute partitioning	2
1.1.2 Dendritic growth	4
1.1.3 Mush permeability	6
1.2 Macrosegregation	7
1.2.1 Liquid thermosolutal convection	8
1.2.2 Solidification shrinkage	8
1.2.3 Movement of equiaxed grains	9
1.2.4 Solid deformation	9
1.3 Other defects	9
1.4 Industrial Worries	11
1.5 Project context and objectives	12
1.5.1 Context	12
1.5.2 Objectives and outline	13
2 Modelling Review	17
2.1 Modelling macrosegregation	18
2.1.1 Macroscopic solidification model: monodomain	19
2.2 Eulerian and Lagrangian motion description	25
2.2.1 Overview	25
2.2.2 Interface capturing	28
2.3 Solidification models with level set	28
2.4 The level set method	29
2.4.1 Diffuse interface	30
2.4.2 Mixing Laws	32
2.5 Interface motion	33
2.5.1 Level set transport	34

Contents

2.5.2	Level set regularisation	35
2.6	Mesh adaptation	39
2.6.1	Metrics and anisotropy	39
2.6.2	<i>Remesh2</i> : Interface remeshing	41
2.6.3	<i>Remesh4</i> : Multi-criteria remeshing	42
3	Energy balance with thermodynamic tabulations	43
3.1	State of the art	44
3.2	Thermodynamic considerations	44
3.2.1	Volume averaging	44
3.2.2	The temperature-enthalpy relationship	45
3.2.3	Tabulation of properties	46
3.3	Numerical method	48
3.3.1	Enthalpy-based approach	51
3.3.2	Temperature-based approach	52
3.3.3	Convergence	52
3.4	Validation	54
3.4.1	Pure diffusion	54
3.4.2	Convection and diffusion	54
3.5	Application: multicomponent alloy solidification	60
3.5.1	Tabulations	62
3.5.2	Discussion	63
4	Macrosegregation with liquid metal motion	69
4.1	Introduction	70
4.2	Formulation stability	70
4.2.1	Stable mixed finite elements	70
4.2.2	Variational multiscale (VMS)	71
4.3	Navier-Stokes solver	72
4.3.1	Strong and weak formulations	72
4.3.2	Stabilisation parameters	76
4.3.3	Implementation	77
4.4	Application to multicomponent alloys	77
4.4.1	Results	80
4.5	Macroscopic prediction of channel segregates	83
4.5.1	Introduction	83
4.5.2	Experimental work	84
4.5.3	Macroscopic scale simulations	84

4.6	Meso-Macro prediction of channel segregates	91
4.6.1	Numerical method	91
4.6.2	Configuration	93
4.6.3	Effect of vertical temperature gradient	97
4.6.4	Effect of cooling rate	99
4.6.5	Effect of lateral temperature gradient	101
4.6.6	Mono-grain freckles	102
5	Macrosegregation with solidification shrinkage	105
5.1	Solidification shrinkage	107
5.2	Choice of interface tracking	107
5.3	Multidomain formalism	109
5.3.1	Assumptions	110
5.4	FE partitioned model	111
5.4.1	In the metal	112
5.4.2	In the air	115
5.5	FE monolithic model	118
5.5.1	Monolithic equations	118
5.5.2	Darcy term in the air	121
5.5.3	Interface motion and stability	121
5.6	1D application: solidification with inverse segregation	125
5.6.1	Geometry and boundary conditions	125
5.6.2	Shrinkage without macrosegregation	126
5.6.3	Shrinkage with macrosegregation	135
5.7	2D application: controlled solidification benchmark	143
5.7.1	Absence of convection	144
5.8	3D application: reduced-gravity solidification	144
5.8.1	Previous work	144
5.8.2	Computational configuration	147
5.8.3	Texus binary alloy	152
5.8.4	Texus ternary alloy	152
5.8.5	Texus quaternary alloy	152
5.8.6	TODO	152
Bibliography		155

Contents

List of Acronyms

Acronym	Standing for
ALE	Arbitrary Lagrangian-Eulerian
BTR	Brittleness temperature range
CAFD	Cellular Automata Finite Difference
CAFE	Cellular Automata Finite Element
CBB	Circumventing Babuška-Brezzi
CCEMLCC	Chill Cooling for the Electro-Magnetic Levitator in relation with Continuous Casting of steel
CEMEF	Center for Material Forming
CFL	Courant–Friedrichs–Lewy
C.FL	Computing and FLuids
CSF	Continuum Surface Force
DLR	Deutsches Zentrum für Luft- und Raumfahrt
DSPG	Darcy-Stabilising/Petrov-Galerkin
EML	Electromagnetic levitation
ESA	European Space Agency
FEM	Finite Element Method
FVM	Finite Volume Method
GMAW	Gas Metal Arc Welding
ISS	International Space Station
IWT	Institut für Werkstofftechnik
LHS	Left-hand side
LSIC	Least squares on incompressibility constraint
LSM	Level set method
MAC	Marker-and-cell
PF	Phase field
PSPG	Pressure-Stabilising/Petrov-Galerkin
RHS	Right-hand side
RUB	Ruhr Universität Bochum
RVE	Representative Elementary Volume
SBB	Satisfying Babuška-Brezzi
SUPG	Streamline-Upwind/Petrov-Galerkin
VMS	Variational MultiScale
VOF	Volume Of Fluid

Contents

Chapter 1

General Introduction

Casting is one the earliest production techniques created by human civilisation since the Bronze Age, dated to circa 3000 BC. From ancient swords to nowadays toys, the need for alloys has never decreased. The key phenomenon behind this technique is solidification, or the transformation of matter from liquid to solid state. With this phase change, many phenomena, not visible to the naked eye, take place with a very complex interaction, in order to form a solid. However, the combination of thermal phenomena, like release of latent heat of solidification, and chemical phenomena like redistribution of chemical element atoms (also known as solute) with other atoms, often lead to *segregation*. The origins of this word from Latin, *segregatus*, has a social meaning of "separating a group from the dominant majority", while in metallurgy it means a non uniform distribution of chemical species. Depending on the scale, we may speak of *microsegregation* when the heterogeneity spans some few hundred microns, whereas the term *macrosegregation* refers to a much coarser length scale, ranging from some millimetres to some meters! The final solid structure is has intrinsic thermophysical and thermomechanical properties directly influenced by the segregation pattern. In casting processes, such as continuous casting (fig. 1.7) and ingot casting, it is crucial to apprehend these intricate phenomena leading to macrosegregation as well as the influence on the final product, at each step of the process.

In this introductory chapter, we give a quick overview of solidification phenomena and microstructure, then present the factors which promote segregation, on both microscopic and macroscopic scales. Aside from macrosegregation, others defects are also briefly presented. In a continuous casting process (fig. 1.1a), the partially solidified slab is carried through a series of rolls that exert contact forces to straighten it. As the mushy part of a slab enters through these rolls, interdendritic liquid is expelled backwards, i.e. in regions with lower solid fraction. Since the slab edges solidify ear-

Chapter 1. General Introduction



Fig. 1.1 – Main steelmaking processes by (a) continuous casting or (b) ingot casting

lier than the centre, the enriched liquid accumulates halfway in thickness, forming a centreline macrosegregation as shown in [fig. 1.2](#). Other types of segregates (channels, A-segregates ...) can also be found but remain more specific to ingot casting. A variety of segregation patterns can be encountered while casting heavy ingots, as in [fig. 1.1b](#):

- the lower part is characterized by a negative segregation cone promoted by the sedimentation of equiaxed crystals and settling of dendrite fragments,
- positive segregation channels, known as A-segregates, form along the columnar dendritic zones, close to the vertical contact with the mould,
- positive V-segregates can be identified in the centre of the ingot,
- a positive "hot-top" macrosegregation in the upper zone where the last rich liquid solidifies, caused by solidification shrinkage and thermosolutal buoyancy forces.

[Combeau et al. \[2009\]](#) state that A-segregates and V-segregates formation is mainly attributed to local flow phenomena. As such, their scale is finer than macrosegregation, hence called "mesosegregates".

1.1 Solidification notions

1.1.1 Solute partitioning

The simplest definition is of this phenomenon is an uneven distribution of solute between the liquid and the growing solid, at the microscopic scale of the interface separating these phases. If we consider a binary alloy, then the solubility limit is the key factor that dictates the composition at which a primary solid phase exists

1.1. Solidification notions



Fig. 1.2 – Zoom on a sulphur print of a continuously cast high carbon steel billet at a longitudinal section, showing high positive centreline segregation [Choudhary et al. 2007].



Fig. 1.3 – Sulphur print (left) of a 65-ton steel ingot [Lesoult 2005] showing various patterns (right) of macrosegregation [Flemings 1974]

Chapter 1. General Introduction

at equilibrium. The segregation (or partition) coefficient k determines the extent of solute rejection into the liquid during solidification:

$$k = \frac{w^{s^*}}{w^{l^*}} \quad (1.1)$$

where w^{s^*} and w^{l^*} are the compositions of the solid and liquid respectively, at the interface. When the segregation coefficient is less than unity (such is the case for most alloys during dendritic solidification), the first solid forms at the liquidus temperature, T , with a composition $w^{s^*} = kw^{l^*} = kw_0$ less than the liquid's composition w_0 , the latter being initially at the nominal composition, w_0 . [Figure 1.4](#) illustrates a typical binary phase diagram where the real solidus and liquidus are represented by solid lines, while the possible linear approximations are in grey dashed lines. For most binary alloys, this linearisation simplifies derivation of microsegregation models, as k becomes independent of temperature.

For each phase, the relationship between the composition at the interface and that in the bulk depends on the chemical homogenisation (i.e. solute diffusivity) of the phase. The more homogeneous a phase, the closer the concentrations between the interface and the bulk, hence closer to equilibrium. It is thus essential to study the effect of homogenisation on the segregation behaviour and the subsequent effect on solidification, which is seen by a non-uniform composition through the cast product on a microscopic scale, better known as microsegregation. This phenomenon is essential in a casting process inasmuch as it affects the microstructure and grain morphology, hence the final mechanical properties of the alloy.

1.1.2 Dendritic growth

In a casting process, the chill surface i.e. the contact between the molten alloy and relatively cold moulds, is the first area to solidify. Thermal gradient, G , and cooling rate, R , are two crucial process parameters that define the solid-liquid interface velocity, \vec{v}^* , which in turn affects the initial microstructure. Although it may be not easy to control them, their crucial role in solidification is well established.

The solid-liquid interface fluctuates when solidifying, thus perturbations may appear on the front, locally destabilizing it. Two outcome scenarios are possible. The first scenario is characterized by low values of \vec{v}^* where the interface maintains a planar shape, hence we speak of *planar growth*. With this kind of growth, a random protuberance appearing at the interface, has a low tip velocity (low driving force of solidification). As such, the rest of the interface catches up, maintaining the planar geometry. In another scenario more representative of a real casting, the interface speed is greater in general,



Fig. 1.4 – Typical eutectic phase diagram of a binary alloy showing the real solidus and liquidus at full equilibrium, with the corresponding linear approximations (grey dashed lines). T_m and T_E are respectively the melting point of the solvent and the eutectic temperature.



Fig. 1.5 – Time evolution of a solidifying Al-4 wt.% Cu sample, showing interface destabilisation and subsequent dendritic solidification [Buffet et al. 2010]. The liquid far from the interface and having a blue color is at nominal composition, while the one near the dendritic structure with the yellow and red colors, is richer in solute.

due to high solidification rate. The protuberance tip will be pulled into a liquid less rich in solute than the interface, as shown in the time frames of [fig. 1.5](#). The zone ahead of the solid-liquid interface is constitutionally undercooled [[Tiller et al. 1953](#)], giving a greater driving force for the protuberance to grow in the direction of the thermal gradient. As the solid-liquid interface adopts a tree-like shape, we speak of *dendritic growth*. Near the chill surface, dendrites are columnar, with a favourable growth in the $<100>$ direction for alloys with cubic lattices, but different orientations are also reported in the literature [see [Dantzig et al. 2009](#), p. 289]. Far from mould walls, a similar dendritic growth phenomenon occurs where temperature is uniform, but with an equiaxed morphology. [Figure 1.6](#) shows both columnar and equiaxed morphologies. Columnar dendrites are characterised by a primary spacing, λ_1 , between the main trunks, and a secondary spacing, λ_2 , for the arms that are perpendicular to the trunks. It should be noted that λ_1 and λ_2 , together with the grain size, are three important microstructural parameters in the as-cast microstructure [[Easton et al. 2011](#)]. Further branching may occur but will not be discussed here.



Fig. 1.6 – In situ observation by X-ray radiography of the (a) columnar microstructure for Al-4 wt.% Cu alloy [[Buffet et al. 2010](#)] and (b) equiaxed microstructure during solidification of Al-10 wt.% Cu alloy [[Bogno et al. 2013](#)].

1.1.3 Mush permeability

The dendritic geometry is crucial in solidification theory as it exhibits lower solid fraction compared to a microstructure formed by planar growth. This fact has consequences on the fluid-structure interaction in the mushy zone, namely the liquid flow through dendrites. At the chill surface, the solid grows gradually from dispersed growing nuclei to a permeable solid skeleton, until finally grains have fully grown at the end of phase change. In the intermediate state, the liquid flow in and out of the mushy zone through the dendrites is a key phenomenon from a rheological perspective. The flow through the solid skeleton is damped by primary and secondary dendrites, result-

ing in momentum dissipation just like in saturated porous media. The famous [Darcy \[1856\]](#) law relates the pressure gradient ($\vec{\nabla}p$) to the fluid velocity \vec{v} (assuming a the solid phase is fixed), through the following equation [[Rappaz et al. 2003](#)]:

$$\vec{v} = \frac{\mathbb{K}}{\mu^l} \vec{\nabla}p \quad (1.2)$$

where μ^l is the liquid dynamic viscosity and \mathbb{K} is the permeability tensor. The latter parameter has been the subject of numerous studies that aimed to predict it from various microstructural or morphological parameters. Some of these studies have started even before the first attempts to model macrosegregation by [Flemings et al. \[1967\]](#), [Flemings et al. \[1968a\]](#), and [Flemings et al. \[1968b\]](#). Basically, all models include the solid fraction, g^s , as input to predict mush permeability along with empirical data. An instance of such models is the work of [Xu et al. \[1991\]](#). Some models rely additionally on the primary dendrite arm spacing λ_1 like Blake-Kozeny [[Ramirez et al. 2003](#)], or the secondary dendrite arm spacing λ_2 like Carman-Kozeny, as a meaningful parameter to determine an isotropic permeability. Other models like [Poirier \[1987\]](#) and [Felicelli et al. \[1991\]](#) derive an anisotropic permeability based on both λ_1 and λ_2 .

The present work uses Carman-Kozeny as a constitutive model for the isotropic permeability scalar (zero order tensor):

$$\mathbb{K} = \frac{\lambda_2^2 g^l{}^3}{180 (1 - g^l)^2} \quad (1.3)$$

1.2 Macrosegregation

Macrosegregation generally stems from a solubility difference between a liquid phase and one or more solid phases, along with a relative velocity between these phases. While the former is responsible for local solute enrichment or depletion, the latter will propagate the composition heterogeneity on a scale much larger than just a few dendrites. This is why macrosegregation could be observed on the scale of a casting, up to several meters in length. While microsegregation can be healed by heat treatments, the alloy to speed up the diffusion process and allow homogenization, heterogeneities spanning on larger distances cannot be treated after solidification. It is obvious that macrosegregation is an irreversible defect. Failure to prevent it, may lead to a substantial decline in the alloy's mechanical behaviour and its serviceability. Experimental investigations of macrosegregation in steels were the subject of numerous studies in the past, like the work of [Suzuki et al. \[1973\]](#), [Shah et al. \[1989\]](#), and [Lesoult \[2005\]](#). They were mainly motivated by industrial research that aimed at reducing defective

Chapter 1. General Introduction

production caused by macrosegregation. However, steel was not the only alloy that was investigated, probably because of its high melting point. Instead, many studies in the past relied on other metallic alloys as a replacement recourse, for their low melting points, also for their well-known thermophysical and mechanical properties, such as aluminium-based alloys (aluminium-copper or aluminium-silicon) [Lesoult et al. 2001; Ferreira et al. 2004; Ferreira et al. 2009] and lead-tin/tin-lead alloys[Hebditch et al. 1974; Prescott et al. 1994; Hachani et al. 2012]. Investigating macrosegregation was not only limited to metallic alloys, but also to organic compounds like the well-known sodium chloride [Wanqi et al. 1989].

Four main factors can (simultaneously) cause fluid flow leading to macrosegregation: thermosolutal convection in the liquid, solidification and thermal shrinkage, movement and sedimentation of equiaxed crystals and finally solid deformation.

1.2.1 Liquid thermosolutal convection

During solidification, the liquid density undergoes changes due to temperature gradients. Generally for steels, an increasing temperature results in a lighter liquid phase and vice-versa. These variations create a driving force of thermal convection in the melt, during which chemical species are redistributed by convective transport. While a uniform composition is usually maintained throughout the liquid phase, solute gradients may appear in zones where thermal convection currents are not sufficient to homogenise the liquid solution. Similarly to thermal gradient, a solute gradient is behind liquid density variations. Nevertheless, the relationship between the liquid's composition and its density is a characteristic of the alloy. While for some alloys, a positive solute gradient creates a positive density gradient, for others the opposite is true, due to a heavier solute. Whether convection is solute or temperature dominated, convection currents are important in the formation of macrosegregation, especially that phase densities vary considerably upon cooling the superheated alloy to room temperature.

1.2.2 Solidification shrinkage

Solid alloys generally have a greater density than the liquid phase ($\rho^s > \rho^l$), thus occupy less volume, with the exception of silicon where the opposite is true. Upon solidification, the liquid moves towards the solidification front to compensate for the volume difference caused by the phase change, as well as the thermal contraction. When macrosegregation is triggered by solidification shrinkage, we speak of *inverse segregation*: while one would naturally expect negative macrosegregation near the

contact with the chill, shrinkage-induced flow promotes the opposite phenomenon, by bringing solute-richer liquid towards the solidifying areas, thus raising their solute content, and resulting in a positively segregated solid. In contrast to liquid convection, shrinkage flow may cause macrosegregation even without gravity.

1.2.3 Movement of equiaxed grains

Globular and equiaxed dendritic grains nucleate and grow in the liquid bulk where thermal gradients are weak, or in the presence of inoculants. Consequently, they are transported by the flow, thus floating or sedimenting depending on their density [Beckermann 2002]. During their movement, the nearby liquid is driven away before the grains finally settle in the end of solidification. Since solute-rich liquid is expelled, a negative macrosegregation zone (often referred to as *negative segregation cone* in cast ingots) is detected in their final position.

1.2.4 Solid deformation

Stresses of thermal and mechanical nature are always found in casting processes (e.g. bulging between rolls in continuous casting). Deformation of the semi-solid in the mushy zone causes a relative solid-liquid flow in the inward (tensile stresses) or outward (compressive stresses) direction, causing macrosegregation.

1.3 Other defects

Apart from macrosegregation, other defects are also encountered in industrial processes. In the casting industry, defects like pores and cracks can be disastrous causing the cast product to be rejected. If possible, the product is reheated, remelted and then cast again. Otherwise it is scrapped. From an economic point view, these operations are very expensive.

Hot tearing

Hot tearing, also denoted solidification cracking or hot cracking, occurs in the mushy zone at high solid fractions when a failure or crack appears at vulnerable locations known as the *hot spots*. They refer to liquid regions enclosed in the solid, where feeding stops, thus creating preferential sites for crack initiation and propagation, as in fig. 1.7a. The temperature range in which the steel is vulnerable to hot tearing is known as the brittleness temperature range (BTR). It corresponds to solid fractions greater



Fig. 1.7 – Three instances of solidification-related defects found in cast products: (a) internal crack in continuous casting [Arcelormittal] (b) surface cavities in ingot casting [Carlson et al. 2002] and (c) freckle in the form of a chain of equiaxed crystals in Ni-base superalloy investment casting [Giamei et al. 1970].

than 90%. Many factors can initiate the failure, but the main origin is a lack of liquid feeding required to compensate for the solidification shrinkage, while the mushy region is exposed to tensile stresses arising from thermal gradients or due to an applied mechanical force.

Porosity

Porosity is a void defect formed inside the casting or at the outer surface. It may be attributed to two different factors. Firstly, we speak of *shrinkage porosity*, when a void forms as a result of density differences between the liquid and its surrounding dendritic solid network, the latter being generally denser than the former. After solidification is complete, the casting surface may look like [fig. 1.7b](#). The second factor is the presence of dissolved gaseous phases in the melt. According to [Dantzig et al. \[2009\]](#), these gases may be initially in the melt, or created by the reaction between the metal and water found in the air or trapped in grooves at the moulds surface. Providing sufficient cooling and pressure drop in the liquid, the latter becomes supersaturated. The nucleation of a gaseous phase is then triggered.

Freckles or segregated channels

The origin of this defect, shown in [fig. 1.7c](#), is a combined effect of microsegregation and buoyancy forces. Upon solidification, solid forms while exchanging solutes with the liquid due to partitioning. For a solute species that preferentially segregates into the liquid (partition coefficient less than unity) and locally reduce the liquid density, a solutal driving force is created inside the mushy zone, generating convection currents, with "plume" shapes as often reported in the literature [[Sarazin et al. 1992](#); [Schneider et al. 1997](#); [Saad et al. 2015](#)]. Temperature gradient is often an additional force of

convection as the liquid density depends also temperature-dependent, the resulting driving force is then qualified as "thermosolutal".

1.4 Industrial Worries

Steel production has continuously increased over the years to meet the industrial needs. [Figure 1.8](#) shows this increase between 1980 and 2013 with a clear dominance of the Chinese production. Quality constraints have also increased where specific grades of steel are needed in critical applications such as mega-structures in construction and heavy machinery. Therefore, alloys with defects are considered vulnerable and should be avoided as much as possible during the casting process. As such, steelmakers have been investing in research, with the aim of understanding better the phenomena leading to casting problems, and improve the processes when possible.

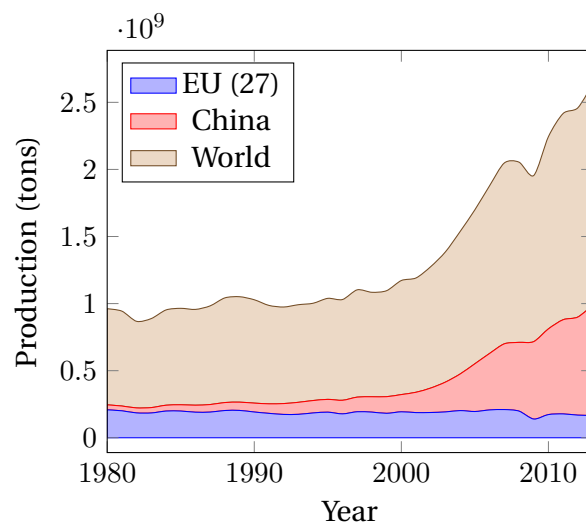


Fig. 1.8 – Evolution curves of crude steel worldwide production from 1980 to 2013 [[WSA 2014](#)].

Simulation software dedicated to alloy casting is one of the main research investments undertaken by steelmakers. These tools coming from academic research are actively used to optimize the process. However, few are the tools that take into account the casting environment. For instance, the continuous casting process, in [fig. 1.7](#), is a chain process where the last steps involve rolls, water sprays and other components. A dedicated software is one that can provide the geometric requirements with suitable meshing capabilities, as well as respond to metallurgical and mechanical requirements, mainly by handling:

- moulds and their interaction with the alloy (thermal resistances ...)

Chapter 1. General Introduction

- alloy filling and predicting velocity in the liquid and mushy zone
- thermomechanical stresses in the solid
- multicomponent alloys and predicting macrosegregation
- microstructure and phases
- finite solute diffusion in solid phases
- real alloy properties (not just constant thermophysical/thermomechanical properties)

1.5 Project context and objectives

1.5.1 Context

The European Space Agency (ESA) has been actively committed, since its foundation in 1975, in the research field. Its covers not only exclusive space applications, but also fundamental science like solidification. This thesis takes part in the ESA project entitled *CCEMLCC*, abbreviating "Chill Cooling for the Electro-Magnetic Levitator in relation with Continuous Casting of steel". The three-year contract from 2011 to late 2014 denoted *CCEMLCC II*, was preceded by an initial project phase, *CCEMLCC I*, from 2007 to 2009. The main focus is studying containerless solidification of steel under microgravity conditions. A chill plate is used to extract heat from the alloy, simulating the contact effect with a mould in continuous casting or ingot casting. A partnership of 7 industrial and academic entities was formed in *CCEMLCC II*. Here is a brief summary of each partner's commitment:

Academic partners

- Center for Material Forming (CEMEF) - France: numerical modelling of microgravity chill cooling experiments
- Deutsches Zentrum für Luft- und Raumfahrt (DLR or German Aerospace Centre) and Ruhr Universität Bochum (RUB) university - Germany: preparation of a chill cooling device for electromagnetic levitation (EML), microgravity testing and investigation of growth kinetics in chill-cooled and undercooled steel alloys
- University of Alberta - Canada: impulse atomization and spray deposition of the D2 tool steel
- University of Bremen - Institut für Werkstofftechnik (IWT) institute - Germany: study of D2 tool steel melt solidification in atomization processing

Industrial partners

- ARCELORMITTAL (France): elaboration of a series of steel grades used in microgravity and ground-based studies
- METSO Minerals Inc. (Finland): material production with D2 tool steel for spray forming
- TRANSVALOR (France): development and marketing of the casting simulation software *Thercast*[®]

CEMEF as an academic partner, contributed to the work by proposing numerical models in view of predicting the chill cooling of steel droplets. A first model was developed by [Rivaux \[2011\]](#). The experimental work by DLR considered various facilities and environments to set a droplet of molten alloy in levitation: EML ([fig. 1.9](#)) for ground-based experiments, microgravity during parabolic flight or sounding rockets and last, microgravity condition on-board the International Space Station (ISS).



Fig. 1.9 – Electromagnetic levitation [[DLR 2014](#)].

1.5.2 Objectives and outline

The main focus of the present thesis is predicting macrosegregation with liquid dynamics assuming a fixed solid phase, i.e. no account of solid transport (e.g. equiaxed crystals sedimentation) and no account of solid deformation. At CEMEF this scope has been adopted in previous studies by [Gouttebroze \[2005\]](#), [Liu \[2005\]](#), [Mosbah \[2008\]](#), [Rivaux \[2011\]](#), and [Carozzani \[2012\]](#). Nevertheless, many modelling features evolved with time such as going from two-dimensional to three-dimensional modelling, resolution schemes for each of the conservation equations: energy, chemical species and liquid momentum, Eulerian or Lagrangian descriptions, modelling of grain structure and others. In this thesis, we propose a numerical model that takes into account i) the energy conservation in a temperature formulation based on a thermodynamic database mapping, ii) the liquid momentum conservation with thermosolutal convection and solidification shrinkage as driving forces, iii) solute mass conservation with

Chapter 1. General Introduction

solidification shrinkage (to predict inverse segregation) and iv) solidification paths at full equilibrium for multicomponent alloys. Moreover, all equations are formulated in a pure Eulerian description while using the level set method to keep implicitly track of the interface between the alloy and the surrounding gas.

To the author's knowledge, this work combining macrosegregation prediction using the level set methodology to track the metal-air interface during shrinkage has no precedent in casting and solidification literature. The model couples in a weak fashion, all four conservation equations presented in [fig. 1.10](#), showing on the one hand, that microsegregation is an essential common link between these equations, while on the other hand, the level set interacts with conservations equations by giving the interface position.

Numerical tools

The current thesis developments are done using C++ language as a part of the in-house code, known as *CimLib* [[Mesri et al. 2009](#)]. It's a finite element library with an object-oriented hierarchy consisting of global finite element solvers for physical differential equations, also point-wise and element-wise solvers for preprocessing and postprocessing the finite element solution. It is also highly parallelised with MPICH2, which makes it possible to handle large meshes with heavy operations like mesh partitioning and adaptation. Side utilities for plotting and analysis are also developed, using python language.

Content outline

This manuscript consists of 5 chapters. In **chapter 2**, a short review introduces the state-of-art in the literature of macroscopic modelling of solidification with transport of energy, species, mass and momentum. **Chapter 3** provides details of the energy conservation equation then introduces a new temperature-based solver compatible with thermodynamic databases **Chapter 4** focuses on the mass and momentum conservation equations and their derivation in the context of a single metallic domain (i.e. without the level set method) where the solid is assumed a fixed and rigid body. As an application, this chapter shows a breakthrough comparison between purely macroscopic and mesoscopic-macroscopic approaches in predicting the hydrodynamic instabilities that lead to channel segregation. The derived energy, mass and momentum equations for the monodomain model are revisited in **chapter 5** in the context of the level set method to predict solidification shrinkage. The influence of shrinkage on macrosegregation is then studied in two different applications.



Fig. 1.10 – A graphical representation of the main elements of the numerical approach, for a macrosegregation model with the level set methodology, when no solid deformation or movement are considered. The dashed lines represent the possible interaction between the components.

Chapter 1. General Introduction

Chapter 2

Modelling Review

Contents

2.1 Modelling macrosegregation	18
2.1.1 Macroscopic solidification model: monodomain	19
2.2 Eulerian and Lagrangian motion description	25
2.2.1 Overview	25
2.2.2 Interface capturing	28
2.3 Solidification models with level set	28
2.4 The level set method	29
2.4.1 Diffuse interface	30
2.4.2 Mixing Laws	32
2.5 Interface motion	33
2.5.1 Level set transport	34
2.5.2 Level set regularisation	35
2.6 Mesh adaptation	39
2.6.1 Metrics and anisotropy	39
2.6.2 <i>Remesh2</i> : Interface remeshing	41
2.6.3 <i>Remesh4</i> : Multi-criteria remeshing	42

2.1 Modelling macrosegregation

Microsegregation models

Solid formation depends greatly on the ability of chemicals species to diffuse within each of the solid and liquid phases, but also across the solid-liquid interface. Furthermore, chemical diffusion like all other diffusional processes, is a time-dependent phenomenon. One can thus conclude that two factors influence the amount of solid formation: cooling rate and diffusion coefficients. However, convection and other mechanical mixing sources, homogenise the composition much faster than atomic diffusion. As such, *complete mixing* in the liquid is always an acceptable assumption, regardless of the solidification time. We may speak of infinite diffusion in the liquid. Nevertheless, diffusion in the solid, also known as *back diffusion*, is the only transport mechanism with very low diffusion coefficients. Therefore, chemical species require a long time, i.e. low cooling rate, to completely diffuse within the solid. The difference in diffusional behaviour at the scale of a secondary dendrite arm, is summarized by two limiting segregation models of perfect equilibrium and nonequilibrium, which are the lever rule and Gulliver-Scheil models, respectively. Afterwards, models with finite back diffusion are presented.

Lever rule

The lever rule considers an ideal equilibrium in all phases, i.e. solidification is extremely slow, hence phase compositions are homogeneous ($w^{l*} = w^l$ and $w^{s*} = w^s$) at all times as a consequence of complete mixing. These compositions are given by:

$$w^l = w^{l*} = k^{-1}w^{s*} = k^{-1}w^s \quad (2.1)$$

$$w^s = w^{s*} = \frac{kw_0}{kf^s + (1 - f^s)} \quad (2.2)$$

At the end of solidification, the composition of the solid phase is equal to the nominal composition, $w^s = w_0$

Gulliver-Scheil

The other limiting case is the absence of diffusion in the solid. That includes also the diffusion at the interface, so nothing diffuses in or out. The consequence is a steady increase of the homogeneous liquid composition while the solid composition remains non-uniform. Compared to a full equilibrium approach, higher fractions of liquid will remain until eutectic composition is reached, triggering a eutectic solidification. The

phase compositions are given by:

$$w^l = w^{l*} = k^{-1}w^{s*} \quad (2.3)$$

$$w^{s*} = kw_0(1 - f^s)^{k-1} \quad (2.4)$$

Finite back diffusion

It has been concluded that the assumption of a negligeable back diffusion overestimates the liquid composition and the resulting eutectic fraction. Therefore, many models studied the limited diffusion in the solid. One of the earliest models is the Brody-Flemings models [Khan et al. 2014] that is a based on a differential solute balance equation for a parabolic growth rate, as follows:

$$w^l = w^{l*} = k^{-1}w^{s*} \quad (2.5)$$

$$w^{s*} = kw_0 [1 - (1 - 2\text{Fo}^s k) f^s]^{\frac{k-1}{1-2\text{Fo}^s k}} \quad (2.6)$$

where Fo^s is the dimensionless *Fourier number* for diffusion in the solid [Dantzig et al. 2009]. It depends on the solid diffusion coefficient D^s , solidification time t_s and the secondary dendrite arm spacing, as follows:

$$\text{Fo}^s = \frac{D^s t_s}{(\lambda_2/2)^2} \quad (2.7)$$

Several other models were since suggested and used. The interested reader is referred to the following non exhaustive list of publications: Clyne et al. [1981], Kobayashi [1988], Ni et al. [1991], Wang et al. [1993], Combeau et al. [1996], Martorano et al. [2003], and Tourret et al. [2009]. It is noted that some of these publications consider also a finite diffusion in the liquid phase.

2.1.1 Macroscopic solidification model: monodomain

In this section, we will present the macroscopic conservations equations that enable us to predict macrosegregation in the metal when the latter is the only domain in the system.

Volume averaging

It is crucial for a solidification model to represent phenomena on the microscale, then scale up to predict macrscopic phenomena. Nevertheless, the characteristic length of a small scale in solidification may represent a dendrite arm spacing, for instance

the mushy zone permeability, as it may also represent an atomic distance if one is interested, for instance, in the growth competition between diffusion and surface energy of the solid-liquid interface. Modelling infinitely small-scale phenomena could be prohibitively expensive in computation time, if we target industrial scales.

The volume averaging is a technique that allows bypassing this barrier by averaging small-scale variations on a so-called *representative volume element* (RVE) [Dantzig et al. 2009] of volume V_E , with the following dimensional constraints: the element should be large enough to "see" and average microscopic fluctuations whilst being smaller than the scale of macroscopic variations. Solid and liquid may exist simultaneously in the RVE, but no gas phase is considered (volume saturation: $V^s + V^l = V_E$). Moreover, temperature is assumed uniform and equal for all the phases. The formalism, introduced by Ni et al. [1991], is summarized by the following equations for any physical quantity ψ :

$$\langle \psi \rangle = \frac{1}{V_E} \int_{V_E} \psi \, d\Omega = \langle \psi^s \rangle + \langle \psi^l \rangle \quad (2.8)$$

where $\langle \psi \rangle^s$ and $\langle \psi \rangle^l$ are phase averages of ψ . Then, for any phase ϕ , one can introduce the *phase intrinsic average* of ψ , denoted $\langle \psi \rangle^\phi$, by writing:

$$\langle \psi^\phi \rangle = \frac{1}{V_E} \int_{V_\phi} \psi \, d\Omega = g^\phi \langle \psi \rangle^\phi \quad (2.9)$$

where g^ϕ is the volume fraction of phase ϕ with $g^\phi = V_\phi/V_E$. To finalize, the averaging is applied to temporal and spatial derivation operators:

$$\left\langle \frac{\partial \psi^\phi}{\partial t} \right\rangle = \frac{\partial \langle \psi^\phi \rangle}{\partial t} - \int_{\Gamma^*} \psi^\phi \vec{v}^* \cdot \vec{n}^\phi \, dA \quad (2.10)$$

$$\left\langle \vec{\nabla} \psi^\phi \right\rangle = \vec{\nabla} \langle \psi^\phi \rangle + \int_{\Gamma^*} \psi^\phi \vec{n}^\phi \, dA \quad (2.11)$$

where \vec{v}^* is the local relative interface velocity and Γ^* is the solid-liquid interface, while \vec{n}^ϕ is the normal to Γ^* , directed outwards. The surface integral terms in eqs. (2.10) and (2.11) are *interfacial averages* that express exchanges between the phases across the interface. The previous equations will be used to derive a set macroscopic conservation equations. It is noted that the intrinsic average $\langle \psi \rangle^\phi$ may be replaced by ψ^ϕ for notation simplicity, whenever the averaging technique applies.

Macroscopic equations

A monodomain macroscopic model relies on four main conservation equations to predict macrosegregation in a single alloy, i.e. the latter is considered without any interaction with another alloy or ambient air. The general form of an averaged conservation equation of any physical quantity ψ is given by:

$$\frac{\partial \langle \psi \rangle}{\partial t} + \nabla \cdot \langle \psi \vec{v} \rangle + \nabla \cdot \left\langle \vec{j}_\psi \right\rangle = \langle Q_\psi \rangle \quad (2.12)$$

The first LHS term in eq. (2.12) represents the time variation of ψ , the second term accounts for transport by advection while the third is the diffusive transport and the RHS term represents a volume source. The considered equations are mass, energy, species conservation and momentum, all summarized in table 2.1. The latter equation is averaged only for the liquid phase, as we assume a fixed and rigid solid phase ($\vec{v}^s = \vec{0}$), thus the corresponding equation vanishes. We develop the ingredients of these

Table 2.1 – Summary of conservation equations with their variables.

Conservation Equation	ψ	\vec{j}_ψ	Q_ψ
Mass	ρ	—	—
Energy	ρh	\vec{q}	—
Species	ρw_i	\vec{j}_i	—
Liquid momentum	$\rho^l \vec{v}^l$	$-\overline{\sigma^l}$	\vec{F}_v^l

equations using the averaging technique, as follows:

$$\langle \rho \rangle = g^l \rho^l + g^s \rho^s \quad (2.13)$$

$$\langle \rho \vec{v} \rangle = g^l \rho^l \vec{v}^l + g^s \rho^s \vec{v}^s \quad (2.14)$$

$$\langle \rho h \rangle = g^l \rho^l h^l + g^s \rho^s h^s \quad (2.15)$$

$$\langle \rho h \vec{v} \rangle = g^l \rho^l h^l \vec{v}^l + g^s \rho^s h^s \vec{v}^s \quad (2.16)$$

$$\langle \rho w_i \rangle = g^l \rho^l w_i^l + g^s \rho^s w_i^s \quad (2.17)$$

$$\langle \rho w_i \vec{v} \rangle = g^l \rho^l w_i^l \vec{v}^l + g^s \rho^s w_i^s \vec{v}^s \quad (2.18)$$

$$\left\langle \rho^l \vec{v}^l \right\rangle = \left\langle \rho^l \vec{v}^l \right\rangle^l = g^l \rho^l \vec{v}^l \quad (2.19)$$

$$\left\langle \rho^l \vec{v}^l \times \vec{v} \right\rangle = g^l \rho^l \vec{v}^l \times \vec{v}^l + g^s \rho^s \vec{v}^l \times \vec{v}^s \quad (2.20)$$

Chapter 2. Modelling Review

Next, we define the average diffusive fluxes, \vec{q} for energy and \vec{j}_i for solutes, using Fourier's conduction law and Fick's first law, respectively [Rappaz et al. 2003]:

$$\langle \vec{q} \rangle = -g^l \langle \kappa \rangle^l \vec{\nabla} T - g^s \langle \kappa \rangle^s \vec{\nabla} T = -\langle \kappa \rangle \vec{\nabla} T \quad (2.21)$$

$$\langle \vec{j}_i \rangle = -g^l \rho^l D^l \vec{\nabla} w_i^l - g^s \rho^s D^s \vec{\nabla} w_i^s \quad (2.22)$$

In eq. (2.22), the macroscopic diffusion coefficient in the solid is neglected, by considering that for macroscopic scales, the average composition of the alloy is much more influenced by advective and diffusive transport in the liquid. In eq. (2.21), we assume that phases are at thermal equilibrium, that is, temperature is uniform in the RVE.

Now that the main conservation equations ingredients are properly defined, we may write each averaged conservation equation as the sum of two local conservation equations for each phase in the RVE, hence introducing also interfacial average terms. For instance, the local mass balance in each phase is given by:

$$\frac{\partial}{\partial t} (g^l \rho^l) + \nabla \cdot (g^l \rho^l \vec{v}^l) = S_V \langle \rho^l \vec{v}^{l*} \cdot \vec{n} \rangle^* - S_V \langle \rho^l \vec{v}^* \cdot \vec{n} \rangle^* \quad (2.23a)$$

$$\frac{\partial}{\partial t} (g^s \rho^s) + \nabla \cdot (g^s \rho^s \vec{v}^s) = -S_V \langle \rho^s \vec{v}^{s*} \cdot \vec{n} \rangle^* + S_V \langle \rho^s \vec{v}^* \cdot \vec{n} \rangle^* \quad (2.23b)$$

where $S_V = A_{sl}/V_E$ is the specific surface area, \vec{v}^{l*} and \vec{v}^{s*} are respectively, the liquid and solid phase velocity at the interface and \vec{v}^* is the previously introduced solid-liquid interface velocity. For instance, the first interfacial exchange term in the RHS of eq. (2.23a) is expanded as follows [Dantzig et al. 2009]:

$$S_V \langle \rho^l \vec{v}^{l*} \cdot \vec{n} \rangle^* = \frac{A_{sl}}{V_E} \left(\frac{1}{A_{sl}} \int_{A_{sl}} \rho^l \vec{v}^{l*} \cdot \vec{n} \, dA \right) \quad (2.24a)$$

$$= \frac{1}{V_E} \int_{A_{sl}} \rho^l \vec{v}^{l*} \cdot \vec{n} \, dA \quad (2.24b)$$

Summing equations (2.23a) and (2.23b), results in the overall mass balance in the RVE:

$$\begin{aligned} \frac{\partial}{\partial t} (g^l \rho^l + g^s \rho^s) + \nabla \cdot (g^l \rho^l \vec{v}^l + g^s \rho^s \vec{v}^s) &= \\ S_V \left\langle \rho^l \left(\vec{v}^{l*} - \vec{v}^* \right) \cdot \vec{n} \right\rangle^* - S_V \left\langle \rho^s \left(\vec{v}^{s*} - \vec{v}^* \right) \cdot \vec{n} \right\rangle^* & \end{aligned} \quad (2.25)$$

where the RHS cancels to zero as shown by Ni et al. [1991]. Moreover, the authors show that with their averaging technique, interfacial exchanges for energy, chemical species and momentum cancel out as they are equal in absolute value but opposite in sign. Using eqs. (2.13) to (2.22) and following the same procedure done in eq. (2.25), the

averaged mass balance hence writes:

$$\frac{\partial \langle \rho \rangle}{\partial t} + \nabla \cdot \langle \rho \vec{v} \rangle = 0 \quad (2.26)$$

whereas the averaged energy balance writes:

$$\frac{\partial \langle \rho h \rangle}{\partial t} + \nabla \cdot \langle \rho h \vec{v} \rangle - \nabla \cdot (\langle \kappa \rangle \vec{\nabla} T) = 0 \quad (2.27)$$

and finally the species balance writes:

$$\frac{\partial \langle \rho w_i \rangle}{\partial t} + \nabla \cdot \langle \rho w_i \vec{v} \rangle - \nabla \cdot (g^l \rho^l D^l \vec{\nabla} w_i^l) = 0 \quad (2.28)$$

As stated previously, the momentum balance in the solid phase is not taken into consideration, hence we do not sum the corresponding local conservation equations. This has consequences on the advection terms in energy and species conservation, and later on we will show the consequences on the momentum conservation in the liquid. First, the advection terms in [eqs. \(2.27\)](#) and [\(2.28\)](#) shall be redefined by considering that the fluid is incompressible ($\nabla \cdot \langle \vec{v}^l \rangle = 0$), which yields:

$$\nabla \cdot \langle \rho h \vec{v} \rangle = \langle \vec{v}^l \rangle \cdot \vec{\nabla} (\rho^l h^l) \quad (2.29)$$

$$\nabla \cdot \langle \rho w_i \vec{v} \rangle = \langle \vec{v}^l \rangle \cdot \vec{\nabla} (\rho^l w_i^l) \quad (2.30)$$

As for the liquid momentum balance, we write:

$$\frac{\partial}{\partial t} (\rho^l g^l \vec{v}^l) + \vec{\nabla} \cdot (\rho^l g^l \vec{v}^l \times \vec{v}^l) = \vec{\nabla} \cdot (g^l \vec{\sigma}^l) + g^l \vec{F}_v^l + \vec{\Gamma}^l \quad (2.31)$$

where \vec{F}_v^l is the vector of external body forces exerted on the liquid phase. In our case, it accounts for the fluid's weight:

$$\vec{F}_v^l = \rho^l \vec{g} \quad (2.32)$$

The interfacial momentum transfer between the solid and liquid phases in [eq. \(2.31\)](#) is modelled by a momentum flux vector $\vec{\Gamma}^l$, consisting of hydrostatic and deviatoric

parts, such that:

$$\vec{\Gamma}^l = \vec{\Gamma}_p^l + \vec{\Gamma}_{\mathbb{S}}^l \quad (2.33)$$

$$\vec{\Gamma}_p^l = p^{l*} \vec{\nabla} g^l = p^l \vec{\nabla} g^l \quad (2.34)$$

$$\vec{\Gamma}_{\mathbb{S}}^l = -g^{l2} \mu^l \mathbb{K}^{-1} (\vec{v}^l - \vec{v}^s) \quad (2.35)$$

where p^{l*} is the pressure at the interface, considered to be equal to the liquid hydrostatic pressure p^l , \mathbb{K} is a permeability scalar (isotropic) computed using eq. (1.2) and μ^l is the liquid's dynamic viscosity. The general form of the Cauchy liquid stress tensor in eq. (2.31) is decomposed as follows:

$$\langle \overline{\sigma}^l \rangle = g^l \overline{\sigma}^l = - \left(\langle p^l \rangle - \lambda \nabla \cdot \langle \vec{v}^l \rangle \right) \bar{\mathbb{I}} + \langle \overline{\mathbb{S}}^l \rangle \quad (2.36)$$

where λ is a dilatational viscosity [Dantzig et al. 2009] and $\overline{\mathbb{S}}^l$ is the liquid strain deviator tensor. In the literature, the coefficient λ is taken proportional to the viscosity: $\lambda = \frac{2}{3} \mu^l$. However, as we consider an incompressible flow, the divergence term vanishes, thus rewriting eq. (2.36) as follows:

$$\langle \overline{\sigma}^l \rangle = - \langle p^l \rangle \bar{\mathbb{I}} + \langle \overline{\mathbb{S}}^l \rangle \quad (2.37a)$$

$$\langle \overline{\sigma}^l \rangle = - \langle p^l \rangle \bar{\mathbb{I}} + 2\mu^l \langle \overline{\dot{\epsilon}}^l \rangle \quad (2.37b)$$

where the transition from eq. (2.37a) to eq. (2.37b) is made possible by assuming a Newtonian behaviour for the liquid phase. The strain rate tensor, $\langle \overline{\dot{\epsilon}}^l \rangle$, depends on the average liquid velocity:

$$\langle \overline{\dot{\epsilon}}^l \rangle = \frac{1}{2} \left(\overline{\nabla} \langle \vec{v}^l \rangle + \overline{\nabla^t} \langle \vec{v}^l \rangle \right) \quad (2.38)$$

Finally, we obtain the final form of momentum conservation in the liquid phase coupled with the averaged mass balance, by injecting eqs. (2.32), (2.34), (2.35), (2.37b) and (2.38) in eq. (2.31):

$$\begin{aligned} \frac{\partial}{\partial t} \left(\rho^l \langle \vec{v}^l \rangle \right) + \frac{1}{g^l} \vec{\nabla} \cdot \left(\rho^l \langle \vec{v}^l \rangle \times \langle \vec{v}^l \rangle \right) = \\ - g^l \vec{\nabla} p^l - 2\mu^l \vec{\nabla} \cdot \left(\overline{\nabla} \langle \vec{v}^l \rangle + \overline{\nabla^t} \langle \vec{v}^l \rangle \right) - g^l \mu^l \mathbb{K}^{-1} \langle \vec{v}^l \rangle + g^l \rho^l \vec{g} \end{aligned} \quad (2.39)$$

where we intentionally employed the *superficial velocity*, $\langle \vec{v}^l \rangle = g^l \vec{v}^l$, as the main unknown, together with the liquid pressure p^l . This system, when modelled in 3D,

2.2. Eulerian and Lagrangian motion description

has a total of 4 unknowns (velocity vector and pressure) and 3 equations (X, Y and Z projections for the velocity vector). A fourth equation provided by the mass balance (eq. (2.26)) is therefore added for closure, giving the following system of equations :

$$\left\{ \begin{array}{l} \frac{\partial}{\partial t} \left(\rho^l \langle \vec{v}^l \rangle \right) + \frac{1}{g^l} \vec{\nabla} \cdot \left(\rho^l \langle \vec{v}^l \rangle \times \langle \vec{v}^l \rangle \right) = \\ - g^l \vec{\nabla} p^l - 2\mu^l \vec{\nabla} \cdot \left(\bar{\nabla} \langle \vec{v}^l \rangle + \bar{\nabla}^t \langle \vec{v}^l \rangle \right) - g^l \mu^l \mathbb{K}^{-1} \langle \vec{v}^l \rangle + g^l \rho^l \vec{g} \\ \nabla \cdot \langle \vec{v}^l \rangle = 0 \end{array} \right. \quad (2.40)$$

Last, the Boussinesq approximation allows taking a constant density in the inertial terms of eq. (2.40) while the variations responsible for buoyancy forces can be computed using ??, if the system is incompressible. Hence, the final set of equations is better known as the incompressible *Navier-Stokes* equations, applied to a solidifying melt:

$$\left\{ \begin{array}{l} \rho_0^l \left(\frac{\partial \langle \vec{v}^l \rangle}{\partial t} + \frac{1}{g^l} \vec{\nabla} \cdot \left(\langle \vec{v}^l \rangle \times \langle \vec{v}^l \rangle \right) \right) = \\ - g^l \vec{\nabla} p^l - 2\mu^l \vec{\nabla} \cdot \left(\bar{\nabla} \langle \vec{v}^l \rangle + \bar{\nabla}^t \langle \vec{v}^l \rangle \right) - g^l \mu^l \mathbb{K}^{-1} \langle \vec{v}^l \rangle + g^l \rho^l \vec{g} \\ \nabla \cdot \langle \vec{v}^l \rangle = 0 \end{array} \right. \quad (2.41)$$

Since all conservation equations were presented and simplified by the main assumption of a static solid phase, we may include them in a graphical summary in section 2.1.1

* Macro models: Rivaux ? Gu beckermann 1999 ?

* Micro macro: Tommy Carozzani2013, guo beckermann 2003, Combeau 2009, Miha Založnik 2010 (indirect), P. Thévoz, J.-L. Desbiolles, M. Rappaz, Metallurgical and Materials TransactionsA 20 (2) (1989) 311–322

* end by talking about taking air into account and the need for an interface capturing method

2.2 Eulerian and Lagrangian motion description

2.2.1 Overview

In mechanics, it is possible to describe motion using two well-known motion description: Eulerian and Lagrangian descriptions. To start with the latter, it describes the motion of a particle by attributing a reference frame that moves with the particle. In

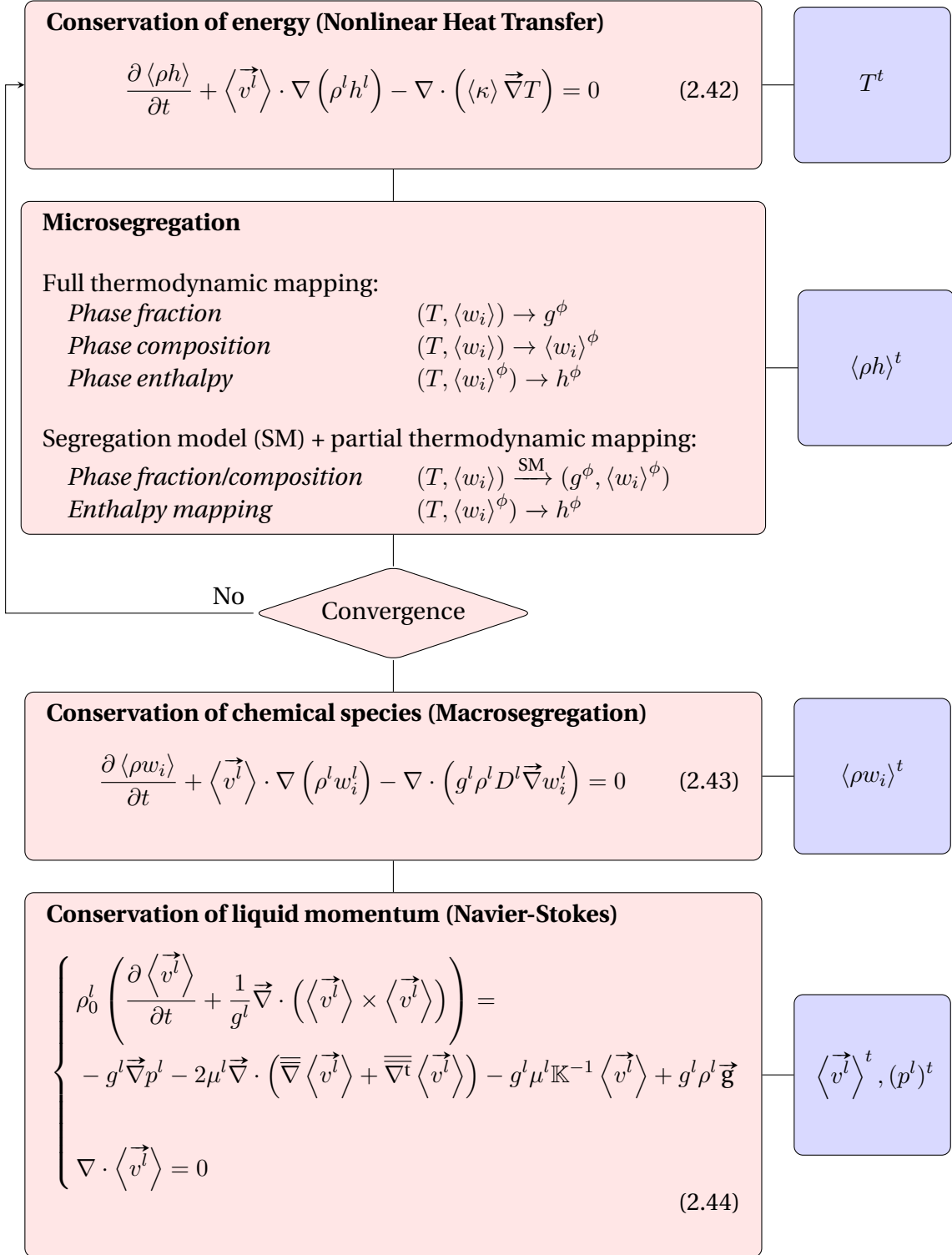


Fig. 2.1 – Graphical resolution algorithm of the conservation equations used in a monodomain macroscopic model to predict macrosegregation for a time increment t . The blue boxes represent the output of each equation.

2.2. Eulerian and Lagrangian motion description

other words, the particle itself is the center of a reference frame moving at the same speed during time. The position vector, denoted by \vec{x} , is hence updated as follows:

$$\vec{x}^{(t+1)} = \vec{x}^{(t)} + \vec{v} \Delta t \quad (2.45)$$

As such, the total variation of any physical quantity ψ related to the particle can be found by deriving with respect to time, $\frac{d\psi}{dt}$. In contrast to the Lagrangian description, the Eulerian description considers a fixed reference frame and independent of the particle's trajectory. The total variation of ψ cannot be simply described by a temporal derivative, since the particle's velocity is not known to the reference frame, and thus the velocity effect, namely the advective transport of ψ , should also be considered as follows:

$$\frac{d\psi}{dt} = \frac{\partial \psi}{\partial t} + \underbrace{\vec{v} \cdot \vec{\nabla} \psi}_{\text{Advection Transport}} \quad (2.46)$$

In this case, the LHS term is also known as *total* or *material derivative*. The importance of these motion descriptions is essential to solve mechanics, whether for fluids or solids, using a numerical method like the finite element method (FEM). One of the main steps of this method is to spatially discretise a continuum into a grid of points (nodes, vertices ...), where any physical field shall be accordingly discretised. Now, if we focus on a node where velocity has a non zero value and following the previously made analysis, two outcomes are possible: either the node would be fixed (Eulerian) or it would move by a distance proportional to the prescribed velocity (Lagrangian). In the latter case, points located on the boundaries constantly require an update of the imposed boundary conditions.

From these explanations, one can deduce that an Eulerian framework is suited for fluid mechanics problems where velocities are high and may distort the mesh points, whereas the Lagrangian framework is better suited for solid mechanics problems where deformation velocities are relatively low and should well behave when predicting strains.

Another motion description has emerged some decades ago, [Hirt \[1971\]](#) call it the Arbitrary Langrangian-Eulerian (ALE) method. ALE combines advantages from both previous descriptions as it dictates a Lagrangian behaviour at "solid" nodes where solid is deforming, and an Eulerian behaviour at "fluid" nodes.

2.2.2 Interface capturing

As no solid deformation is considered in this work, the Eulerian framework is a convenient choice. Solidification shrinkage is to be considered in our current scope, so it will deform the alloy's outer surface in contact with the air. We intend to track this interface and its motion over time via a numerical method. A wide variety of methods accomplish this task while they yield different advantages and disadvantages. Such methods fall into two main classes, either interface tracking or interface capturing, among which we cite: marker-and-cell (MAC) [Harlow et al. 1965], volume of fluid (VOF) [Hirt et al. 1981], phase field methods (PF), level set method (LSM) [Osher et al. 1988], coupled level set - VOF method and others. The interested reader may refer to quick references by Prosperetti [2002] and Maitre [2006] about these methods.

In the past years, the level set method received a considerable attention in many computational fields, specifically in solidification. For this reason, we will focus on this method henceforth, giving a brief literature review and technical details in the next sections.

2.3 Solidification models with level set

In classic solidification problems, the need to track an interface occurs usually at the solid-liquid interface, that is why the phase field method [Karma et al. 1996; Boettinger et al. 2002] and the level set method [Chen et al. 1997; Gibou et al. 2003; Tan et al. 2007] were applied at a microscale to follow mainly the dendritic growth of a single crystal in an undercooled melt. In our case however, when we mention "solidification models using LSM", we do not mean the solid-liquid interface inside the alloy, but it is the alloy(liquid)-air interface that we intend to track, assuming that microscale phenomena between the phases within the alloy, are averaged using the previously defined technique in section 2.1.1.

Very few models were found in the literature, combining solidification and level set as stated previously. Du et al. [2001] applied it to track the interface between two molten alloys in a double casting technique. Welding research, on another hand, has been more active adapting the level set methodology to corresponding applications. In CEMEF, two projects made use of the metal-air level set methodology in welding simulations and showed promising results. Desmaison et al. [2014] employed this methodology to simulate a hybrid arc and laser beam welding used in high thickness steel sheet welding. Later, Chen [2014] applied it to gas metal arc welding (GMAW) to predict the grain structure in the heat affected zone essentially. More recently,

Courtois et al. [2014] used the same methodology but this time to predict keyhole defect formation in spot laser welding. The tracked interface in this case was that between the molten alloy and the corresponding vapor phase.

2.4 The level set method

Firstly introduced by Osher et al. [1988], this method became very popular in studying multiphase flows. It is reminded that the term *multiphase* in computational domains usually refers to multiple fluids, and thus should not be mixed with definition of a phase in the current solidification context. For disambiguation, we shall use *multifluid flow* when needed. The great advantage lies in the way the interface between two fluids, F_1 and F_2 is implicitly captured, unlike other methods where the exact interface position is needed. In a discrete domain, the concept is to assign for each mesh node of position vector \vec{x} , the minimum distance $d_\Gamma(\vec{x})$ separating it from an interface Γ . The distance function, denoted α and defined in eq. (2.47), is then signed positive or negative, based on the fluid or domain to which the node belongs.

$$\alpha(\vec{x}) = \begin{cases} d_\Gamma(\vec{x}) & \text{if } \vec{x} \in F_1 \\ -d_\Gamma(\vec{x}) & \text{if } \vec{x} \in F_2 \\ 0 & \text{if } \vec{x} \in \Gamma_{F1,F2} \end{cases} \quad (2.47)$$

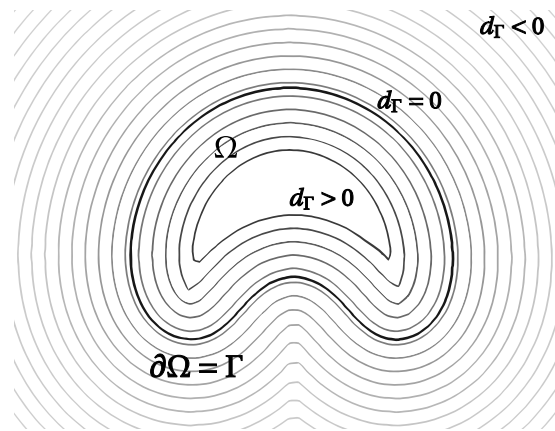


Fig. 2.2 – Schematic of the interface Γ (thick black line) of a rising air bubble (Ω) in water. The other contours represent isovalues of the distance function around and inside the interface contour. Those outside are signed negative whereas inside they are signed positive.

2.4.1 Diffuse interface

The level set has many attractive properties that allows seamless implementation in 2D and 3D models. It is a continuously differentiable C^1 -function. The Heaviside function is also continuous but non differentiable, with an abrupt transition from 0 to 1 across the sharp interface, as follows:

$$H = H(\alpha(\vec{x})) = \begin{cases} 0 & \text{if } \alpha(\vec{x}) < 0 \\ 1 & \text{if } \alpha(\vec{x}) \geq 0 \end{cases} \quad (2.48)$$

With the help of eq. (2.48), we can define the geometric "presence" of a domain with respect to the interface. As such, material properties depend upon this function, which will be discussed later in section 2.4.2. It is established that a steep transition can lead to numerical problems, so the Heaviside function should be smoothed in a volume of fixed thickness around the interface. Sinusoidal smoothing in eq. (2.49) is widely used with level set formulations.

$$H = \begin{cases} 0 & \text{if } \alpha(\vec{x}) < -\varepsilon \\ 1 & \text{if } \alpha(\vec{x}) > \varepsilon \\ \frac{1}{2} \left(1 + \frac{\alpha(\vec{x})}{\varepsilon} + \frac{1}{\pi} \sin \left(\frac{\pi \alpha(\vec{x})}{\varepsilon} \right) \right) & \text{if } -\varepsilon \leq \alpha(\vec{x}) \leq \varepsilon \end{cases} \quad (2.49)$$

where the interval $[-\varepsilon; +\varepsilon]$ is an artificial interface thickness around the zero distance. Defining a diffuse interface rather than a sharp one, is also a common approach in phase field methods [Beckermann et al. 1999; Sun et al. 2004]. It is emphasized that the latter methods give physically meaningful analysis of a diffuse interface and the optimal thickness by thoroughly studying the intricate phenomena happening at the scale of the interface. However, for level set methods, there has not been a formal work leading the same type of analysis. For this reason, many aspects of the level set method lack physical meanings but remain computationally useful. In a recent paper by Gada et al. [2009], the authors respond partially to this problem by analysing and deriving conservation equations using a level set in a more meaningful way, but do not discuss the diffuse interface aspect.

The Dirac delta function is also an important property to convert surface integrals to volume terms, which could turn useful when modelling surface tension effects for instance, using the *continuum surface force* method (CSF) [Brackbill et al. 1992]. The Dirac function, plotted in fig. 2.3 along with the Heaviside function within an interface

thickness of $[-\varepsilon; +\varepsilon]$, is derived from the Heaviside as follows:

$$\delta(\alpha) = \delta(\alpha(\vec{x})) = \frac{\partial H}{\partial \alpha(\vec{x})} = \begin{cases} \frac{1}{2\varepsilon} \left(1 + \cos \left(\frac{\pi \alpha(\vec{x})}{\varepsilon} \right) \right) & \text{if } |\alpha(\vec{x})| \leq \varepsilon \\ 0 & \text{if } |\alpha(\vec{x})| > \varepsilon \end{cases} \quad (2.50)$$

The Heaviside and delta Dirac functions can be readily processed to obtain other geometric properties from the level set, which are extremely useful. We mention the most relevant ones [Peng et al. 1999]:

$$\text{normal vector : } \vec{n} = \frac{\vec{\nabla}\alpha}{\|\vec{\nabla}\alpha\|} \quad (2.51)$$

$$\text{curvature : } \zeta = -\nabla \cdot \vec{n} \quad (2.52)$$

$$\text{surface area of the air-metal interface : } A^\Gamma = \int_{\Omega} \delta(\alpha) \|\vec{\nabla}\alpha\| d\Omega \quad (2.53)$$

$$\text{metal volume : } V^M = \int_{\Omega} H^M d\Omega \quad (2.54)$$

where, for the last two equations, we consider a three-dimensional domain Ω containing two subdomains, metal and air, separated by an interface Γ . It is reminded that for a 2D case, eq. (2.53) evaluates a length instead of the area while eq. (2.54) gives the area instead of volume. Finally, within the diffuse interface, fluids properties may vary linearly or not, depending on the mixing law, which is presented in the next section.

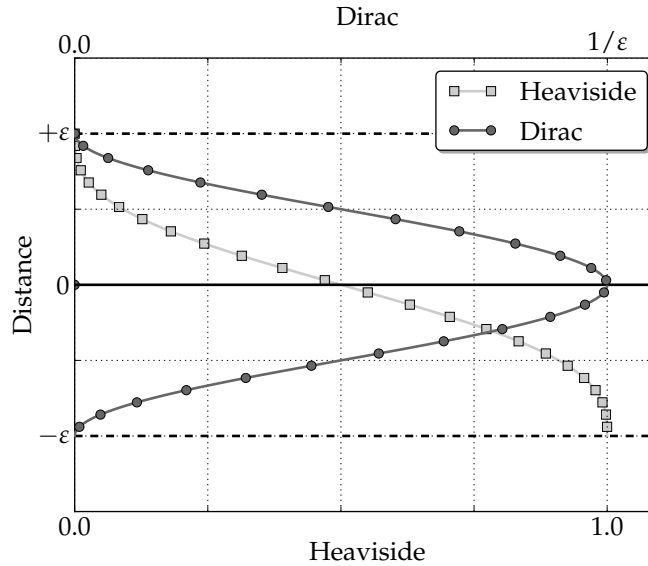


Fig. 2.3 – Schematic of two level properties inside the diffuse interface: Heaviside (lower x-axis) and Dirac delta (upper x-axis) functions. Note that the peak of the Dirac function depends on the interface thickness to ensure a unity integral of the delta function over Ω .

2.4.2 Mixing Laws

A *monolithic* resolution style, as opposed to a *partitioned* resolution, is based on solving a single set of equations for both fluids separated by an interface, as if a single fluid were considered. Level set is one among many methods that use the monolithic style to derive a single set of conservation equations for both fluids. The switch from one material to the other is implicitly taken care of by using the Heaviside function as well as mixing laws. These laws are crucial to define how properties vary across the diffuse interface in view of a more accurate resolution. The most frequently used mixing law in the literature is the arithmetic law. Other transitions are less known such as the harmonic and logarithmic mixing. The first law is maybe the most intuitive and most used for properties mixture as it emanates from VOF-based methods. If we consider any property ψ (for instance the fluid's dynamic viscosity μ) then the arithmetic law will give a mixed property $\hat{\psi}$ as follows:

$$\hat{\psi} = H^{F_1}\psi^{F_1} + H^{F_2}\psi^{F_2} \quad (2.55)$$

Basically, the result is an average property that follows the same trend as the Heaviside function. As for the harmonic law, it writes:

$$\hat{\psi} = \left(\frac{H^{F_1}}{\psi^{F_1}} + \frac{H^{F_2}}{\psi^{F_2}} \right)^{-1} \quad (2.56)$$

and last, the logarithmic law writes:

$$\hat{\psi} = n^{(H^{F_1} \log_n \psi^{F_1} + H^{F_2} \log_n \psi^{F_2})} \quad (2.57)$$

where n is any real number serving as a logarithm base, which often is either the exponential e or 10. The mixture result with this law is the same, regardless of the value of n . By looking to [fig. 2.4](#), we clearly see that the difference between all three approaches is the property weight given to each side of the level set in the mixture. The arithmetic law, being symmetric, has equal weights, ψ^{F_1} and ψ^{F_2} , in the final mixture. Nevertheless, the asymmetric harmonic mixing varies inside the diffuse interface with a dominant weight of one property over the other. As for the logarithmic mixture, it can be seen as an intermediate transition between the preceding laws. As long as the interface thickness is small enough, the choice of a mixing law should not drastically change the result, inasmuch as it depends on the discretisation resolution of the interface. This fact made the arithmetic mixing the most applied one, because it is symmetric and easy to implement (no handling of potential division problems like

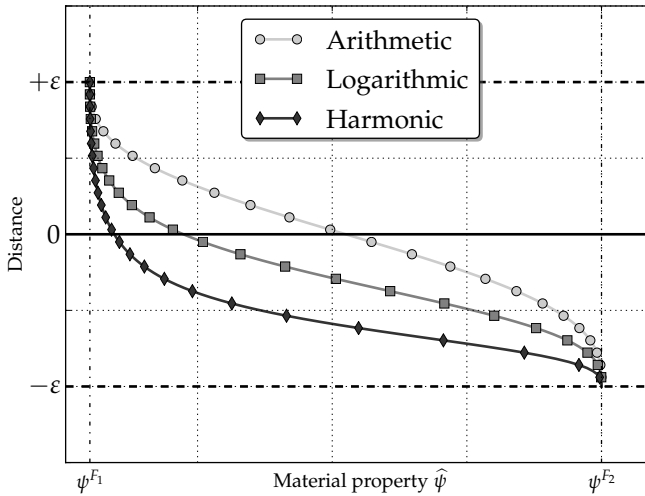


Fig. 2.4 – Three mixing laws, arithmetic, logarithmic and harmonic commonly used in monolithic formulations.

harmonic laws for instance). However, Strotos et al. [2008] claim that the harmonic law proves to conserve better diffusive fluxes at the interface. More recently, an interesting study made by Ettrich et al. [2014] focused on mixing thermal properties using a phase field method. They define a diffuse interface in which they separately mix the thermal conductivity, κ , and the heat capacity, C_p , then compute the thermal diffusivity as the ratio of these properties. Later, the authors compare the temperature field obtained by diffusion to a reference case in order to decide which combination of mixing laws gives the best result. Despite not being directly related to a level set method, this work gives an insight of the mixture possibilities and their effect on a pure thermal diffusion. Otherwise, little work has been found in the literature on the broad effects of mixture types on simulation results in a level set context.

2.5 Interface motion

When a physical interface needs to have topology changes because of fluid structure interaction or surface tension for instance, the level set model can follow these changes by a transport step. The idea is to advect the signed distance function, its zero isovalue representing the interface and all other distant isovales, with the velocity field as input. The motion of the interface is thus expressed by:

$$\frac{d\alpha}{dt} = \frac{\partial\alpha}{\partial t} + \vec{v} \cdot \vec{\nabla}\alpha = 0 \quad (2.58)$$

2.5.1 Level set transport

The finite element method gives the fully discretised weak form of [eq. \(2.58\)](#) by using a convenient set of test functions α^* belonging the Hilbertian *Sobolev* space:

$$\int_{\Omega} \alpha^* \frac{\partial \alpha}{\partial t} d\Omega + \int_{\Omega} \alpha^* \vec{v} \cdot \vec{\nabla} \alpha d\Omega = 0 \quad \forall \alpha^* \in \mathcal{H}^1(\Omega) \quad (2.59)$$

The spatial discretisation of α assigns, for each of the total N nodes of a simplex, the following values:

$$\alpha = \sum_N P_j \alpha_j \quad (2.60)$$

Furthermore, with the standard Galerkin method, we replace test functions by the interpolation functions P_j , then we apply a temporal discretisation for the main unknowns by a forward (implicit) finite difference in time. Consequently, [eq. \(2.59\)](#) can be recast as follows:

$$i, j : 1 \rightarrow \text{Nnodes}$$

$$\frac{1}{\Delta t} (\alpha_j^t - \alpha_j^{t-\Delta t}) \int_{\Omega} P_i P_j d\Omega + \alpha_j^t \int_{\Omega} \vec{v}^t \cdot \vec{\nabla} P_j d\Omega = 0 \quad (2.61a)$$

$$\left[\frac{1}{\Delta t} \int_{\Omega} P_i P_j d\Omega + \int_{\Omega} \vec{v}^t \cdot \vec{\nabla} P_j d\Omega \right] \alpha_j^t = \frac{1}{\Delta t} \int_{\Omega} \alpha^{t-\Delta t} P_i d\Omega \quad (2.61b)$$

$$[\mathcal{M}_{ij} + \mathcal{A}_{ij}] \alpha_j^t = \mathcal{F}_i \quad (2.61c)$$

where \mathcal{M}_{ij} and \mathcal{A}_{ij} are respectively the mass (or capacity) matrix and advection matrix, both written within a local finite element, whereas \mathcal{F}_i is a local vector of known quantities from the previous time step. The solution of the linear system in [eq. \(2.61c\)](#) is the transported distance function.

When the convection regime becomes more dominant diffusion (for high Reynolds number), the standard Galerkin method may lead to instabilities in the solution. In this case, stabilisation is crucial to avoid these oscillations, unless very fine remeshing is done "such that convection no longer dominates on an element level", as stated by [Brooks et al. \[1982\]](#). The authors give a brief explanation of how numerically a convection-dominated equation can lead to oscillatory solutions with the standard Galerkin approximation. They proposed a stabilisation scheme, the Streamline Upwind Petrov-Galerkin, better known as SUPG, to stabilise advection dominated Navier-Stokes equations. However, their technique applies to any convection-diffusion equation. The SUPG method consists of modifying the test functions (like a classical Petrov-

Galerkin method) by adding artificial diffusion in the flow direction. The modified test function writes:

$$\alpha_{SUPG}^* = \alpha^* + \underbrace{C_{SUPG}^E (\vec{v}_{\text{transport}} \cdot \vec{\nabla} \alpha^*)}_{\text{Upwind contribution}} \quad (2.62)$$

where the upwind contribution for each finite element E depends on a stabilisation parameter C_{SUPG}^E that is expressed as follows:

$$C_{SUPG}^E = \frac{h^E}{v_{\text{flow}}^E} \quad (2.63)$$

[Equation \(2.63\)](#) shows that the SUPG parameter represents a time constant relative to an element mesh size, h^E , and an average velocity that should represent the magnitude in the flow direction. In the present work, all convection-diffusion equations are stabilised with the SUPG method, namely the conservation of mass, energy, momentum and chemical species as well as the level set transport.

2.5.2 Level set regularisation

Upon transport the distance function field, a crucial property of the level set may be partially or totally lost over the domain, which is:

$$\begin{cases} \|\vec{\nabla} \alpha\| = 1 \\ \alpha(x, t) = 0 & \text{if } x \in \Gamma(t) \end{cases} \quad (2.64)$$

The closer this L^2 -norm to one, the more regular the level set. An irregular distance function induces cumulative numerical errors while transporting distance values far from the interface, resulting in wrong distance information, and loss of properties that make up a "distance function". To show one the benefit of level set regularisation, [Basset \[2006\]](#) states after showing several tests of distance function transport, that regularised distance functions transported with a standard Galerkin method (i.e. without any stabilisation) show better "quality" globally in the domain, compared to initially non-regularised ones. When the transport equation in [eq. \(2.58\)](#) is discretised in time then solved, a *regularisation* (also known as *reinitialisation*) is necessary to conserve as much as possible the property in [eq. \(2.64\)](#).

[Figure 2.5](#) shows the need of regularisation in two different simulations of the same phenomenon: rising air bubble inside water. The importance of this well studied case [[Sussman et al. 1994](#); [Hysing et al. 2009](#)] is that the interface between two fluids is

highly deformable as the bubble rises because of buoyancy, and therefore the task of tracking the dynamic interface while maintaining an accurate distance function is a considerable numerical task. In the first simulation, the distance contours are squeezed against the zero-distance contour marked by the thick black line. A closer look to the interface reveals undesired distortions, with a "wavy" shape at some points. This effect is evidently an artefact of a level set transport lacking subsequent reinitialisation, inasmuch as the surface tension tends to minimise the total surface area and make it as smooth as possible. Nevertheless, the second simulation unveils much better results, especially how the interface shows no sign of destabilisation. We also note the regular spacing between contours, which is a consequence of conserving the property defined in [eq. \(2.64\)](#). This improvement is attributed to the regularization done at each time step after the transport. In the forthcoming sections, we present three regularisation methods, then show their strong and weak points.



Fig. 2.5 – Schematic of the influence of level set regularisation on the distance function at the same time frame: a) without any regularisation step, the isovalue contours are distorted in the wake of the rising air bubble while being squeezed ahead of it, b) in contrast to regularising the distance function, where the contours maintain their spacing and geometric properties with respect to the tracked interface.

Classic Hamilton-Jacobi reinitialisation

In order to repair a distance function impaired by convective transport, [Sussman et al. \[1994\]](#) proposed solving a classic *Hamilton-Jacobi* equation, given in its most general form:

$$\frac{\partial \alpha}{\partial t} + \mathbb{H}(\alpha, x, t) = 0 \quad x \in \Omega, t > 0 \quad (2.65)$$

where $\alpha(x, t = 0) = \alpha_0$ is the initial value of the distance function. The term \mathbb{H} is known as the *Hamiltonian*. When the sign of the level set and its metric property ($\|\vec{\nabla}\alpha\| = 1$) are considered, eq. (2.65) reduces to:

$$\frac{\partial \alpha}{\partial t} + S(\alpha) (\|\vec{\nabla}\alpha\| - 1) = 0 \quad (2.66)$$

where $S(\alpha)$ is a step function giving the sign of the level set as follows:

$$S(\alpha) = \frac{\alpha}{|\alpha|} = \begin{cases} -1 & \text{if } \alpha < 0 \\ 0 & \text{if } \alpha = 0 \\ +1 & \text{if } \alpha > 0 \end{cases} \quad (2.67)$$

The sign function defined in eq. (2.67) is often smoothed to avoid numerical problems, as proposed for instance by [Sussman et al. \[1994\]](#):

$$S(\alpha) = S_\varepsilon(\alpha) = \frac{\alpha}{\sqrt{\alpha^2 + \varepsilon^2}} \quad (2.68)$$

where ε is a smoothing parameter that depends on the mesh size around the interface. However, one should be aware that within the smoothing thickness, the regularised function may suffer from local oscillations because of the reciprocal reinitialisation taking place at each side of the level set. [Peng et al. \[1999\]](#) states that this problem is more likely to happen if the initial level set shows very weak or very steep gradients, and therefore is not regular enough. The authors eventually propose a new sign function which would reinitialise the distance function, as close as possible to the interface without modifying the latter, as follows:

$$S(\alpha) = S_\varepsilon(\alpha) = \frac{\alpha}{\sqrt{\alpha^2 + \|\vec{\nabla}\alpha\|^2 \varepsilon^2}} \quad (2.69)$$

Convective reinitialization

A recent work by [Ville et al. \[2011\]](#) introduced another concept for reinitialisation called the *convective reinitialisation*. The idea lies in combining both level set advection and regularisation in a single equation, saving resolution time. The key components of their method starts by defining a pseudo time step, $\Delta\tau$, that is linked to the main time variable through a numerical parameter λ_τ , as follows:

$$\lambda_\tau = \frac{\partial \tau}{\partial t} \quad (2.70)$$

The order of magnitude of λ_τ , which can be seen as a relaxation parameter [see [Vigneaux 2007](#), p. 89], is close to the ratio $h/\Delta t$. Then, the classic Hamilton-Jacobi [eq. \(2.65\)](#) is combined into the convection step by writing:

$$\frac{\partial \alpha}{\partial t} + (\vec{v} + \lambda_\tau \vec{U}) \cdot \vec{\nabla} \alpha = \lambda_\tau S(\alpha) \quad (2.71)$$

where \vec{U} is a velocity vector in the normal direction to the interface, defined by $\vec{U} = S(\alpha) \vec{n}$, the normal vector \vec{n} being previously defined in [eq. \(2.51\)](#). The obvious shortcoming of convective reinitialisation is that it depends on a numerical parameter λ_τ . Another limitation of the method is the use of a sinusoidal filter to modify the distance function by truncating its values beyond a thickness threshold, which is also another parameter to calibrate the resolution. The drawback of truncating the level set is the loss of information far from the interface and the inability to fully reconstruct the distance function. If we denote this threshold by E and the modified level set by $\tilde{\alpha}$ inside the thickness, then [eq. \(2.71\)](#) is recast as:

$$\frac{\partial \alpha}{\partial t} + (\vec{v} + \lambda_\tau \vec{U}) \cdot \vec{\nabla} \alpha = \lambda_\tau S(\alpha) \sqrt{1 - \left(\frac{\pi}{2E} \tilde{\alpha}\right)^2} \quad (2.72)$$

[Equation \(2.72\)](#) describes the transport and partial reconstruction of the distance function α , knowing its value $\tilde{\alpha}$ inside the thickness E .

Geometric reinitialization

This category of methods go from the level set's basic geometric principle to construct a distance function, instead of solving a partial differential system of equations as in the classic Hamilton-Jacobi reinitialisation. A widely known instance of this category is the *fast marching method* developed by [Sethian \[1996\]](#) and influenced by the [Dijkstra \[1959\]](#)'s method to compute the shortest path in a network of nodes. The method aims to solve the eikonal equation in [eq. \(2.64\)](#) to propagate the distance function in a single direction by *upwinding*, i.e. going from low to high values of the distance function, while preserving a unitary distance gradient.

Direct reinitialisation is another interesting method in the geometric reinitialise category. However, it has not gained noticeable attention in the literature given the terrible cost in terms of computation time and efficiency if not optimised. The main idea is very simple: reconstruct the distance function over Ω or a subset of Ω , by computing the minimum distance between each mesh node and the interface. It means that, for

any point $\vec{x} \in \Omega$, the following constraint should be satisfied Osher et al. [2003]:

$$d_\Gamma(\vec{x}) = \min \|\vec{x} - \vec{x}_\Gamma\| \quad \forall \vec{x}_\Gamma \in \partial\Omega = \Gamma, \quad (2.73)$$

A efficient and optimised implementation of this method is done by Shakoor et al. [2015] making use of k - d trees to limit the search operations of elements and the subsequent distance evaluations in each of these elements. Moreover, the authors give a comparison of the previously stated methods on 2D and 3D cases, showing the great performance of direction reinitialisation when used with k-d trees algorithm, hence we use it in the present work.

2.6 Mesh adaptation

2.6.1 Metrics and anisotropy

The key to reduce spatial discretisation errors and obtain better results is a fine mesh. The optimal mesh resolution depends on the equations being discretised and solved on the FE grid, which consists of an array of structured triangles (fig. 2.6a), in the most basic situation. However, the potential of the Finite Element Method over other methods like the Finite Volume Method (FVM) is the use of unstructured grids. The easiest meshing solution one can choose is to create unstructured homogeneous and isotropic grid (fig. 2.6b), while respecting some constraints regarding the time step (temporal discretisation) stemming from physical or numerical conditions, e.g. diffusion shock constraint in diffusional transient equations or Courant–Friedrichs–Lewy (CFL) condition in transient advective equations. In such a case, errors due to interpolation are minimised, which guarantees good results but with expensive time cost.

Heterogeneous meshes (fig. 2.6c) that consist of fine isotropic elements in areas of interest along with coarser isotropic elements in other areas, may reduce the needed time to solve each conservation equation. Although this is an interesting alternative, it is less powerful than anisotropic meshing. In the latter (fig. 2.6d), elements adapt to a physical quantity, such as enthalpy or velocity, reducing the elemental length in the direction where the gradient is higher, while stretching the element in the orthogonal direction. This allows more accurate resolution with less elements than needed by isotropic meshing. Moreover, this type of meshing is well adapted to the context of this thesis as it allows getting a fine mesh in the normal direction to the interface, that is in its transport direction, while reducing the number of elements in other directions. Regions undergoing solidification are also important to remesh since microsegregation starts in the mushy zone, i.e. between the liquidus and solidus temperatures

given by a local average composition, where fluid flow may transport species, leading eventually to macrosegregation.

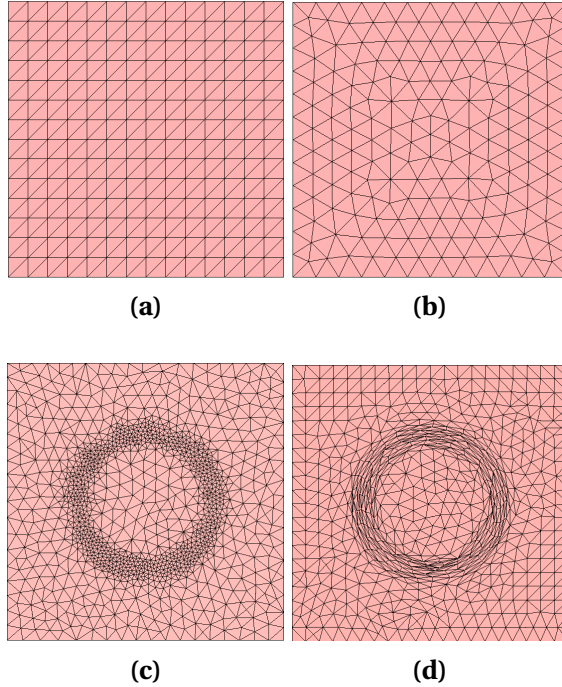


Fig. 2.6 – Alternatives for initial finite element grid generation: (a) structured homogeneous, (b) unstructured homogeneous isotropic, (c) unstructured heterogeneous isotropic and (d) unstructured heterogeneous anisotropic meshes.

Since mesh adaptation involves advanced mathematical notions, readers interested in the basics are referred to the following references: [Coupez 1991; Coupez 2000; Gruau et al. 2005; Jannoun 2014]. In this study, we show and compare different remeshing methods relevant to macrosegregation prediction, and based on previous work done at CEMEF. These techniques rely on metric tensors, and some of them belong to *a posteriori* error estimators category. A metric or a metric tensor \mathcal{M} , also known as *Riemannian* metric, is a positive symmetric definite matrix that relates to an element's size in \mathbb{R}^3 via:

$$\mathcal{M} = \begin{pmatrix} M_{11} & M_{12} & M_{13} \\ M_{12} & M_{22} & M_{23} \\ M_{13} & M_{23} & M_{33} \end{pmatrix} = \mathcal{R} \begin{pmatrix} 1/h_x^2 & 0 & 0 \\ 0 & 1/h_y^2 & 0 \\ 0 & 0 & 1/h_z^2 \end{pmatrix} \mathcal{R}^T \quad (2.74)$$

where \mathcal{R} is a rotation matrix and h_x , h_y and h_z are the respective dilatation scalars defined by the metric in the (x, y, z) space, describing a three-dimensional anisotropy. The metric information is then passed to a mesh generation tool, called *MTC*, which is based on an iterative procedure of local topology optimisations. We focus hereafter

on two adaptive remeshing techniques, then discuss the functional details and show some examples.

2.6.2 Remesh2: Interface remeshing

Remesh2 is an explicit method to compute an anisotropic metric around the zero surface of a distance function. The idea is, as mentioned previously, to reduce the elements cost in the tangential directions to level set by stretching the elements, leaving small element lengths in the normal direction, where the level set gradient is the greatest. This method is not based on error estimators, but rather on explicit input from the user who chooses the mesh size in normal and tangential directions to the interface, as well as in the positive and negative regions delimited by the level set. The following parameters are used as input data to determine the final node-wise metric:

- $h_{\vec{n}}$ mesh size in the normal direction of the level set
- $h_{\vec{\tau}}$ mesh size in the tangential directions of the level set
- h_M mesh size in the metal
- h_A mesh size in the air
- α distance function (level set)
- ε level set mixing thickness
- \vec{V} arbitrary vector

Algorithm 1: *Remesh2* metric construction

Data: \vec{n} h_M h_A $h_{\vec{n}}$ $h_{\vec{\tau}}$ α
Result: \mathcal{M}_2

 Initialise node index: $j = 0$;

while $j \leq j_{end}$ **do**
if $\alpha_j < \varepsilon$ **then**

 Compute normal direction to level set: $\vec{n} = \vec{\nabla}\alpha / \|\vec{\nabla}\alpha\|$;

 Compute the first tangential direction: $\vec{\tau}_1 = \vec{V} - (\vec{V} \cdot \vec{n}) \cdot \vec{n}$;

 Deduce the second tangential direction: $\vec{\tau}_2 = \vec{n} \wedge \vec{\tau}_1$;

 Compute rotation matrix and its transpose: \mathcal{R}_j and \mathcal{R}_j^{-1} ;

 Deduce P1 metric at node j : $(\mathcal{M}_2)_j = \mathcal{R}_j \Lambda \mathcal{R}_j^{-1}$
else

go back to the beginning of current section;

 Increment j ;

2.6.3 Remesh4: Multi-criteria remeshing

It is a metric construction method based on edge-based error distribution

What i concluded from Z-FAST-SMACS cases A and B, where remesh4 was used in two different ways (LS and velocity/100 , LS and ConcentrationPosNeg) is that for diffuse interface thickness less than 2e-4 m, mass conservation gets all sorts of problems, because of low element resolution around interface while higher resolution at the tips of the transition region

To do ?

Interface Remeshing: Importance when using a static level set and more importantly when LS is transported, influence of mixing area *thickness* and *resolution* (i.e. nb of nodes with the area), Isotropic or anisotropic ? the first is more important to composition calculation while the second is more relevant if we mean do thermohydraulics without macrosegregation

Chapter 3

Energy balance with thermodynamic tabulations

Contents

3.1 State of the art	44
3.2 Thermodynamic considerations	44
3.2.1 Volume averaging	44
3.2.2 The temperature-enthalpy relationship	45
3.2.3 Tabulation of properties	46
3.3 Numerical method	48
3.3.1 Enthalpy-based approach	51
3.3.2 Temperature-based approach	52
3.3.3 Convergence	52
3.4 Validation	54
3.4.1 Pure diffusion	54
3.4.2 Convection and diffusion	54
3.5 Application: multicomponent alloy solidification	60
3.5.1 Tabulations	62
3.5.2 Discussion	63

3.1 State of the art

When speaking about macrosegregation, one needs to know that the problem involves phase change. For that, a minimum of four conservation equations are necessary: conservation of mass, momentum, chemical species and energy. The phase change literature contains a wealth of numerical methods to solve energy conservation in solidifying alloys. A comprehensive overview of these methods is given by [Swaminathan. et al. \[1993\]](#).

The corresponding equation associates the total average enthalpy to the temperature via intrinsic alloy properties, such as the heat capacity of the phases and the latent heat associated with the phase transformations. However, in the course of solidification and while macrosegregation is taking place, these properties change because the average composition may vary significantly: the transformation paths are thus modified, as well as the phases' composition and heat capacity. Similarly, the latent heat of phase transformations is not a mere constant that could be distributed as a function of the phase fractions assuming only temperature-dependent phases' properties, as often found in the literature [\[Bellet et al. 2009\]](#). It is thus impossible to establish a priori the dependence of the enthalpy with respect to temperature when macrosegregation alters the average composition, even in the case of full thermodynamic equilibrium between phases.

In this chapter, we discuss a suitable numerical scheme based on an enthalpy method, already used in the literature to alleviate this macrosegregation-related problem [\[Swaminathan. et al. 1993; Carozzani et al. 2013\]](#). Later on, we introduce a modified formulation, using the effective heat capacity method that increases the original scheme's efficiency. The introduced method uses tabulated thermodynamic quantities (solidification paths, phases' enthalpy and composition) in a range of average compositions and temperatures as found in the literature [\[Doré et al. 2000; Thuillet et al. 2004; Du et al. 2007\]](#), with the aim of evaluating the total average enthalpy as well as the effective heat capacity. The novelty of the modified method resides in the use of thermodynamic tabulations without losing the advantages of the previous method, thus yielding faster computation times while maintaining a good accuracy.

3.2 Thermodynamic considerations

3.2.1 Volume averaging

The volume averaging technique, presented in [section 2.1.1](#), is the first thing consider when solving the energy equation in the presence of macrosegregation. The reason is

3.2. Thermodynamic considerations

that phase quantities that vary with the average composition, have a great impact on the thermal properties, hence on the overall heat transfer in the system. We recall the basic equation:

$$\langle \psi \rangle = \sum_{\phi} g^{\phi} \langle \psi \rangle^{\phi} \quad (3.1)$$

where g^{ϕ} denotes the volume fraction of phase ϕ in the RVE. It should be emphasized that the averaging technique applies to virtually all thermodynamic variables (enthalpy, density . . .). Among these variables, the temperature is also considered to be uniform in the RVE. Applying the volume averaging technique to the energy conservation principle along with interfacial balances between the phases, results in the following averaged equation [Rappaz et al. 2003]:

$$\frac{\partial \langle \rho h \rangle}{\partial t} + \nabla \cdot (\langle \rho h \vec{v} \rangle) = \nabla \cdot (\langle \kappa \rangle \vec{\nabla} T) + \langle \dot{Q}_V \rangle \quad (3.2)$$

where ρ stands for the density, h the mass enthalpy, \vec{v} the velocity field, κ the thermal conductivity, T the temperature and \dot{Q}_V a possible volume heat source. [Equation \(3.2\)](#) is the standard averaged form of the energy conservation equation used in non-stationary phase change problems.

Once the variational form has been discretised in space and time, two possible resolution schemes emerge: the first is an explicit forward Euler scheme which gives rise to a linear equation where the temperature is known at time t , T^t . This requires very small time steps in the current context, which limits the solver's usability at the scale of industrial applications. The second scheme is the backward Euler or full implicit discretisation where terms are function of $T^{t+\Delta t}$. It leads to a nonlinear equation with 2 interdependent unknowns, $\langle \rho h \rangle^{t+\Delta t}$ and $T^{t+\Delta t}$. It is clear that the nature of the temperature-enthalpy relationship plays a central role when formulating the resolution strategy of this nonlinear equation. Generally, it is admitted that, depending on the resolution strategy, it is necessary to express enthalpy as a function of temperature or vice-versa, together with associated partial derivatives, $\frac{d\langle \rho h \rangle}{dT}$ or $\frac{dT}{d\langle \rho h \rangle}$.

3.2.2 The temperature-enthalpy relationship

In solidification problems, additional variables are involved in [eq. \(3.1\)](#) and [eq. \(3.2\)](#), like the transformation path that defines the history of the phase fractions, as well as the average chemical composition $\langle w_i \rangle$, i being the index of the chemical species (only the solutes are considered). The temperature-enthalpy relation averaged over

the phases in a given RVE writes:

$$\langle \rho h \rangle = \sum_{\phi} g^{\phi}_{(T, \langle w_i \rangle \dots)} \rho^{\phi}_{(T, \langle w_i \rangle^{\phi} \dots)} h^{\phi}_{(T, \langle w_i \rangle^{\phi} \dots)} \quad (3.3)$$

Note that the volume average enthalpy is approximated by the product $\langle \rho h \rangle^{\phi} = \langle \rho \rangle^{\phi} \langle h \rangle^{\phi}$ in the current work. As stated in the introduction, it becomes clear from [eq. \(3.3\)](#) that phase properties, i.e. average phase density, ρ^{ϕ} and enthalpy, h^{ϕ} , are temperature and composition dependent. This equation is the key to convert the average volume enthalpy to temperature (through a procedure named *H2T*) or vice-versa (*T2H*). The values of the different phase fractions g^{ϕ} (solidification path) and phase enthalpies $\langle \rho h \rangle^{\phi}$ are thus needed to close the relation.

3.2.3 Tabulation of properties

The complexity of performing a thermodynamic conversion is directly linked to the simplicity of determining the alloy properties, namely the phase fractions and phase enthalpies. In the case of binary alloys and with several assumptions with respect to the system (e.g., linear mono-varient temperature composition relationships, constant heat capacity of phases and constant latent heat of transformations, equilibrium approximations between phases) analytical calculations are often used to determine the properties. Nevertheless, analytical relations are more complex or even impossible to derive in the case of multicomponent alloys ($i > 1$). To overcome this problem, one can resort to thermodynamic databases and phase equilibrium calculations to tabulate the transformation paths and the phase enthalpies for a given range of temperatures and average compositions. It is a handy solution for two main reasons: first, the conversion is merely a binary search in a table; secondly, it is a simple solution for coupling with macrosegregation. In this way, phase fractions g^{ϕ} are tabulated as functions of temperature and average composition, while for each phase ϕ the mass enthalpy, h^{ϕ} , and the density, ρ^{ϕ} , are tabulated as functions of temperature and phase intrinsic average compositions $\langle w_i \rangle^{\phi}$, as well as other possible parameters. [Table 3.1](#) summarizes the steps in order to perform a temperature-to-enthalpy (*T2H*) conversion using the predefined tabulation approach. In step 1, the transformation path is acquired for each average composition and temperature to determine the list of phases, their volume fractions g^{ϕ} and their intrinsic compositions $\langle w_i \rangle^{\phi}$. In step 2, the phase enthalpy h^{ϕ} and density ρ^{ϕ} are determined by searching for the temperature and the already known phase composition $\langle w_i \rangle^{\phi}$. In step 3, the average volume enthalpy is computed from the volume fraction, density and mass enthalpy of phases using [eq. \(3.3\)](#). The

3.2. Thermodynamic considerations

Table 3.1 – Tabulation processing for a $T2H$ procedure

Step Number	1	2	3
Inputs	$T, \langle w_i \rangle$	$T, \langle w_i \rangle^\phi$	$g^\phi, \rho^\phi h^\phi$
Outputs	$g^\phi, \langle w_i \rangle^\phi$	ρ^ϕ, h^ϕ	$\langle \rho h \rangle$ (eq. (3.3))

methodology to build the tabulations is straightforward. It is based on two main scans. On the one hand, intervals for the variation of the average composition $\langle w_i \rangle$ are chosen from the known alloy composition. These variations have to cover the extreme values adopted during the simulation, which are not known a priori. An interval is also selected for the variation of temperature. The latter is easier to determine as it usually starts from the initial melt temperature and goes down to the room temperature in a standard casting simulation. For each mapping of composition and temperature, a thermodynamic equilibrium state is computed. The outputs are the number of phases encountered, together with their fraction and intrinsic compositions. The minimum and maximum intrinsic composition for each phase could then be determined. On the other hand, for each phase, a scan of the intrinsic composition and temperature is made to compute the intrinsic properties. The same temperature interval and step as defined earlier are used. Regarding the enthalpy-to-temperature conversion ($H2T$), a backward iterative $T2H$ search is performed. For a known composition $\langle w_i \rangle$, denoting (τ) the iteration index to convert the enthalpy H_{input} , we start with an initial guess for temperature $T^{(\tau=0)}$ then convert it to an enthalpy $H^{(\tau=0)}$ with the $T2H$ conversion. Using an appropriate nonlinear algorithm (Brent is the most versatile in our case), we aim at minimizing the following scalar residual: $R_H = |H_{\text{input}} - H^{(\tau)}|$. Once the algorithm has converged, the temperature $T^{(\tau)}$ is the result of the $H2T$ conversion. It is inferred that the first conversion ($T2H$) is a direct one whereas the latter ($H2T$) is indirect and requires a series of iterative steps; each step being a single $T2H$ resolution. In other words, a $H2T$ conversion is a backward search for a temperature, hence it is slower. This conversion's speed lag is exacerbated when tabulations increase in size (e.g. large number of temperature and composition steps) and complexity (e.g., multi-component industrial alloys used in casting), since the search gets more complicated with the increasing number of input columns (one column for each alloying element).



Fig. 3.1 – Algorithm for a single temperature to enthalpy ($T2H$) conversion.

3.3 Numerical method

The finite element method is used to solve the energy conservation as expressed by [eq. \(3.2\)](#). A test function \mathcal{W} belonging to the Hilbertian Sobolev space $\mathcal{H}^1(\Omega_E)$ of continuous integrable test functions is used to formulate the integral variational form of [eq. \(3.2\)](#) [[Süli 2000](#)]. A Fourier boundary condition is considered on the domain boundary $\partial\Omega_E$. The domain Ω is discretised using first-order linear simplexes, Ω_E , defined by their number of local nodes (denoted “NbLoc”): triangles in 2D with NbLoc=3 and tetrahedra in 3D with NbLoc=4. The outcome is a residual that we aim to minimize so that the conservation principle is satisfied. Therefore, the weak form writes:

$$\begin{aligned} \forall \mathcal{W} \in M = \{u \in \mathcal{H}^1(\Omega_E)\} \\ \int_{\Omega_E} \mathcal{W} \frac{\partial \langle \rho h \rangle}{\partial t} dV + \int_{\Omega_E} \mathcal{W} \left\langle \vec{v}^l \right\rangle \cdot \vec{\nabla} (\rho^l h^l) dV - \int_{\Omega_E} \mathcal{W} \nabla \cdot (\langle \kappa \rangle \vec{\nabla} T) dV - \int_{\Omega_E} \mathcal{W} \left\langle \dot{Q}_V \right\rangle dV = 0 \end{aligned} \quad (3.4)$$

where we assumed a static solid phase and an incompressible liquid phase, which allowed recasting the second term of [eq. \(3.2\)](#) into $\left\langle \vec{v}^l \right\rangle \cdot \vec{\nabla} (\rho^l h^l)$. The steps for discretizing in time and space the previous equation are well detailed in some book references like [Rappaz et al. \[2003\]](#) and [Dantzig et al. \[2009\]](#). As for enthalpy and temperature, they are spatially discretised in each simplex using interpolations functions \mathcal{P} , thus



Fig. 3.2 – Algorithm for a single enthalpy to temperature (H2T) conversion.

Chapter 3. Energy balance with thermodynamic tabulations

defining the nodal values H_j and T_j , respectively:

$$\langle \rho h \rangle = \sum_{j=1}^{\text{NbLoc}} \mathcal{P}_j H_j \quad (3.5)$$

$$T = \sum_{j=1}^{\text{NbLoc}} \mathcal{P}_j T_j \quad (3.6)$$

Note that H_j is a volumetric enthalpy. The Galerkin formulation gives the following expression for the residual contribution at a mesh node i (PS: here i is not the usual solute index) for time step t in a local element Ω_E :

$$(R_i^E)^t = \mathcal{M}_{ij}^E (H_j^t - H_j^{t-\Delta t}) + \mathcal{A}_{ij}^E T_j^t + (\mathcal{K}1_{ij}^E + \mathcal{K}2_{ij}^E) - \mathcal{F}_i^E - \mathcal{Q}_i^E = 0 \quad (3.7)$$

$i, j : 1 \rightarrow \text{NbLoc}$

where the volumetric contributions are detailed as follows:

$$\text{transient term: } \mathcal{M}_{ij}^E = \int_{\Omega_E} \frac{1}{\Delta t} \mathcal{P}_i \mathcal{P}_j dV \quad (3.8)$$

$$\text{advection term: } \mathcal{A}_{ij}^E = \int_{\Omega_E} \rho^l C_p^l \mathcal{P}_i \left\langle \vec{v}^l \right\rangle \cdot \vec{\nabla} \mathcal{P}_j dV \quad (3.9)$$

$$\text{diffusion term: } \mathcal{K}1_{ij}^E = \int_{\Omega_E} \langle \kappa \rangle \vec{\nabla} \mathcal{P}_i \vec{\nabla} \mathcal{P}_j dV \quad (3.10)$$

$$\text{source term: } \mathcal{Q}_i^E = \int_{\Omega_E} \mathcal{P}_i \left\langle \dot{Q}_V \right\rangle dV \quad (3.11)$$

while the surface boundary contributions are given by:

$$\text{boundary condition term 1: } \mathcal{K}2_{ij}^E = \int_{\partial\Omega_E} h_{\text{ext}} \mathcal{P}_i \mathcal{P}_j dS \quad (3.12)$$

$$\text{boundary condition term 2: } \mathcal{F}_i^E = \int_{\partial\Omega_E} h_{\text{ext}} T_{\text{ext}} \mathcal{P}_i dS \quad (3.13)$$

$$(3.14)$$

The surface integrals $\mathcal{K}2_{ij}^E$ and \mathcal{F}_i^E are related to a Fourier-type boundary condition, with h_{ext} as a coefficient of heat exchange and T_{ext} as the external temperature far from the boundary. The energy conservation principle is satisfied when the sum of the residual contributions coming from all the mesh elements is zero. In other words, the following global residual defined by the assembly of these contributions, should

be minimized:

$$(R_i)^t = \mathcal{M}_{ij} \left(H_j^t - H_j^{t-\Delta t} \right) + \mathcal{A}_{ij} T_j^t + (\mathcal{K}1_{ij} + \mathcal{K}2_{ij}) T_j^t - \mathcal{F}_i - \mathcal{Q}_i = 0 \quad (3.15)$$

$i, j : 1 \rightarrow \text{NbGlob}$

where the global tensors \mathcal{M}_{ij} , \mathcal{A}_{ij} , $\mathcal{K}1_{ij}$, $\mathcal{K}2_{ij}$, \mathcal{F}_i and \mathcal{Q}_i contain respectively, after an assembly step, the contributions of the local matrices \mathcal{M}_{ij}^E , \mathcal{A}_{ij}^E , $\mathcal{K}1_{ij}^E$, $\mathcal{K}2_{ij}^E$, \mathcal{F}_i^E and \mathcal{Q}_i^E from each discretised element in the domain Ω . Accordingly, the indices i and j refer to global node numbers, where the total number of nodes is denoted by "NbGlob". It is clear that the global residual inherits the dependence between enthalpy and temperature. This is shown in eq. (3.15) where the average volume enthalpy is a function of the temperature. It infers that this residual is a non-linear function; therefore minimizing it requires an iterative non-linear algorithm. Our choice settles on the Newton-Raphson method, known for its quadratic convergence speed. A solidification problem can induce severe non-linearities from the release of the latent heat (which itself is temperature-composition dependent) and the variations of the thermophysical properties of the alloy with respect to temperature and average composition. This algorithm could thus treat such variations. Considering the link between enthalpy and temperature, eq. (3.15) may be solved either for enthalpy or for temperature as a nodal unknown; hence both formulations are presented hereafter.

3.3.1 Enthalpy-based approach

The residual is re-written using a Taylor series expansion to the first order for a non-linear iteration (ν) :

$$(R_i)^{(\nu+1)} = (R_i)^{(\nu)} + \left(\frac{dR}{dH} \right)_{ij}^{(\nu)} \Delta H_j^{(\nu)} + \mathcal{O}(H_j^2) \quad (3.16)$$

Neglecting the second order terms, the suggested correction at each iteration in view of cancelling the residual and giving the new value $H_j^{(\nu)}$, is given by the linear system in eq. (3.17) relative to what we call a *Hsolver*:

$$\left(\frac{dR}{dH} \right)_{ij}^{(\nu)} \left(H_j^{(\nu+1)} - H_j^{(\nu)} \right) = -R_i^{(\nu)} \quad (3.17)$$

where $\frac{dR}{dH}$ is a global tangent matrix yielding the variations of the residual with respect to the enthalpy in the last iteration, $H_j^{(\nu)}$. If eq. (3.7) is considered, then the contribu-

tion of an element Ω_E writes:

$$\left(\frac{dR}{dH} \right)_{ij}^{(\nu)E} = \underbrace{\mathcal{M}_{ij}^E + \mathcal{A}_{ij}^E \left(\frac{dT}{dH} \right)_j^{(\nu)}}_{\text{no sum on } j} + \underbrace{(\mathcal{K}1_{ij}^E + \mathcal{K}2_{ij}^E) \left(\frac{dT}{dH} \right)_j^{(\nu)}}_{\text{no sum on } j} \quad (3.18)$$

[Equation \(3.18\)](#) is the core of the enthalpy-based solver. The resolution of [eq. \(3.17\)](#) then yields a new estimate of the vector of nodal enthalpies $H^{(\nu+1)}$, which are the only unknowns to be solved for. Once determined at iteration (ν) , convergence tests are performed (refer to section

3.3.2 Temperature-based approach

Similarly to the Hsolver, the local residual is recast for a nonlinear iteration (ν) , leading this time to an iterative temperature correction:

$$\left(\frac{dR}{dT} \right)_{ij}^{(\nu)} \left(T_j^{(\nu+1)} - T_j^{(\nu)} \right) = -R_i^{(\nu)} \quad (3.19)$$

where $\frac{dR}{dT}$ is a global tangent matrix yielding the variations of the residual with respect to temperature $T_j^{(\nu)}$ at the previous iteration. This solver will be referred to as *Tsolver*. The contribution of an element Ω_E to this tangent matrix is evaluated as:

$$\left[\left(\frac{dR}{dT} \right)_{ij}^{(\nu)} \right]^E = \underbrace{\mathcal{M}_{ij}^E \left(\frac{dH}{dT} \right)_j^{(\nu)}}_{\text{no sum on } j} + \mathcal{A}_{ij}^E + (\mathcal{K}1_{ij}^E + \mathcal{K}2_{ij}^E) \quad (3.20)$$

In contrast to the previous solver, [eq. \(3.20\)](#) is the core of the temperature-based solver. The resolution of [eq. \(3.19\)](#) then yields a new estimate of the vector of nodal temperatures $T^{(\nu+1)}$, which are the only unknowns to be solved for. Once updated for iteration (ν) , convergence tests are performed (refer to section

3.3.3 Convergence

The previous two sections described the iterative resolution of the same discretised energy conservation by both Tsolver and Hsolver. However, in [eqs. \(3.18\)](#) and [\(3.20\)](#), an important term emerges from the tangent matrix evaluation describing the variations between temperature and enthalpy: $\frac{dH}{dT}$ (or $\frac{dT}{dH}$). This term invokes the previously mentioned temperature-enthalpy tabulations which depend on the alloy composition. Consequently, $\frac{dH}{dT}$ (or $\frac{dT}{dH}$) has a great influence on the convergence of the Tsolver

(respectively the Hsolver). When eq. (3.17) or eq. (3.19) is solved at iteration (ν) , this term is written using a finite difference:

$$\text{Tsolver} \quad \left(\frac{dH}{dT} \right)_j^{(\nu+1)} = \frac{\langle \rho h \rangle_j^{(\nu+1)} - \langle \rho h \rangle_j^{(\nu)}}{T_j^{(\nu+1)} - T_j^{(\nu)}} \quad (3.21)$$

$$\text{Hsolver} \quad \left(\frac{dT}{dH} \right)_j^{(\nu+1)} = \frac{T_j^{(\nu+1)} - T_j^{(\nu)}}{\langle \rho h \rangle_j^{(\nu+1)} - \langle \rho h \rangle_j^{(\nu)}} \quad (3.22)$$

For the Tsolver, the enthalpy $\langle \rho h \rangle_j^{(\nu)}$ is needed to evaluate eq. (3.21). In contrast, the Hsolver requires the value of $T_j^{(\nu)}$ to evaluate the corresponding eq. (3.22). In both cases, the unknown is determined by the temperature-enthalpy relation. The indices next to the mentioned unknowns indicate that this relation is used for each iteration (ν) at each mesh node j , hence affecting the global resolution time between the two solvers. The Hsolver needs a $H2T$ to evaluate $\frac{dT}{dH}$, whereas the Tsolver needs a $T2H$ to evaluate $\frac{dH}{dT}$. It can be seen that Tsolver uses solely $T2H$ procedure (flowchart in fig. 3.1) and the thermodynamic tabulations to determine the enthalpy, hence the term $\frac{dH}{dT}$. On the other hand, Hsolver repeats the same procedure a finite number of times in order to determine a temperature output through $H2T$ (flowchart in fig. 3.2) and use it to compute $\frac{dT}{dH}$. This algorithmic difference leverages the Tsolver in terms of computation time providing the same numerical accuracy while conserving the total system energy.

Convergence tests are necessary at the end of each iteration of the energy solver to determine the convergence status of the algorithm. In the context of the Tsolver for instance, the residual is re-evaluated with the newly determined temperature $T_j^{(\nu+1)}$ and enthalpy $H_j^{(\nu+1)}$ so eq. (3.15) rewrites:

$$(R_i)^{(\nu+1)} = \mathcal{M}_{ij} \left(H_j^{(\nu+1)} - H_j^{t-\Delta t} \right) + \mathcal{A}_{ij} T_j^{(\nu+1)} + (\mathcal{K}1_{ij} + \mathcal{K}2_{ij}) T_j^{(\nu+1)} - \mathcal{F}_i - \mathcal{Q}_i \\ i, j : 1 \rightarrow \text{NbGlob} \quad (3.23)$$

The norm of the current residual, $\|R^{(\nu+1)}\|$, is compared to a fixed small value $\varepsilon_R \approx [10^{-5}; 10^{-4}]$. The resulting temperature variation, $|T_j^{(\nu)} - T_j^{(\nu-1)}|$, should also respond to similar criterion between two consecutive iterations. For that purpose, we compare it to another fixed value $\varepsilon_T \approx [10^{-3}; 10^{-2}]$. Convergence is ultimately achieved when

the following criteria are simultaneously met:

$$\begin{cases} \|R^{(\nu+1)}\| < \varepsilon_R \\ \text{Max}_{j:1 \rightarrow \text{NbGlob}} |T_j^{(\nu+1)} - T_j^{(\nu)}| < \varepsilon_T \end{cases} \quad (3.24)$$

A comparison of both solver formulations is done in the hereafter test cases section.

3.4 Validation

3.4.1 Pure diffusion

The two solvers are first tested in a purely diffusive case for a one-dimensional solidification configuration. Predictions with a 1D front tracking model [Gandin 2000] is used as a benchmark. It provides solutions for the temperature and solid fraction during directional solidification of a 10 cm long Al-7 wt.% Si ingot. The melt, with initial uniform temperature, is cooled with a heat exchange coefficient (assuming a Fourier boundary condition) from one side, the other side being adiabatic. All values for alloy properties, initial and boundary conditions and numerical parameters are listed in [table 3.2](#). For this simple test case, we use linear temperature dependence of the intrinsic phase enthalpies, that is $\langle \rho h \rangle^s = \langle \rho C_p \rangle T$ and $\langle \rho h \rangle^l = \langle \rho C_p \rangle T + \rho L$, where $\langle \rho C_p \rangle$ is the heat capacity per unit volume and ρL is the latent heat per unit volume. Values for $\langle \rho C_p \rangle$ and ρL , as well as for the thermal conductivities, $\kappa = \langle \kappa \rangle^l = \langle \kappa \rangle^s$, are taken constant. Moreover, a Gulliver Scheil approximation is used to compute a single temperature – fraction of solid relationship in the absence of macrosegregation. This is done assuming a linear binary phase diagram and thus requires using the properties listed in [table 3.2](#), i.e. the segregation coefficient, k , the liquidus slope, m_L , the liquidus temperature, T_L , and the eutectic temperature, T_E . [Figure 3.5](#) show the comparison with the Hsolver and Tsolver. The cooling curves and liquid fraction results are found superimposed to the front tracking solution, thus giving validation of the implementation as well as the iterative schemes presented above to solve the energy conservation

3.4.2 Convection and diffusion

To validate the Tsolver with fluid flow, we consider the following set of equations already defined in the flowchart of [section 2.1.1](#). Moreover, an assumption of a static and non deformable solid phase is made. Consequently, the mechanical model is reduced to the conservation of momentum in the liquid phase. This assumption also

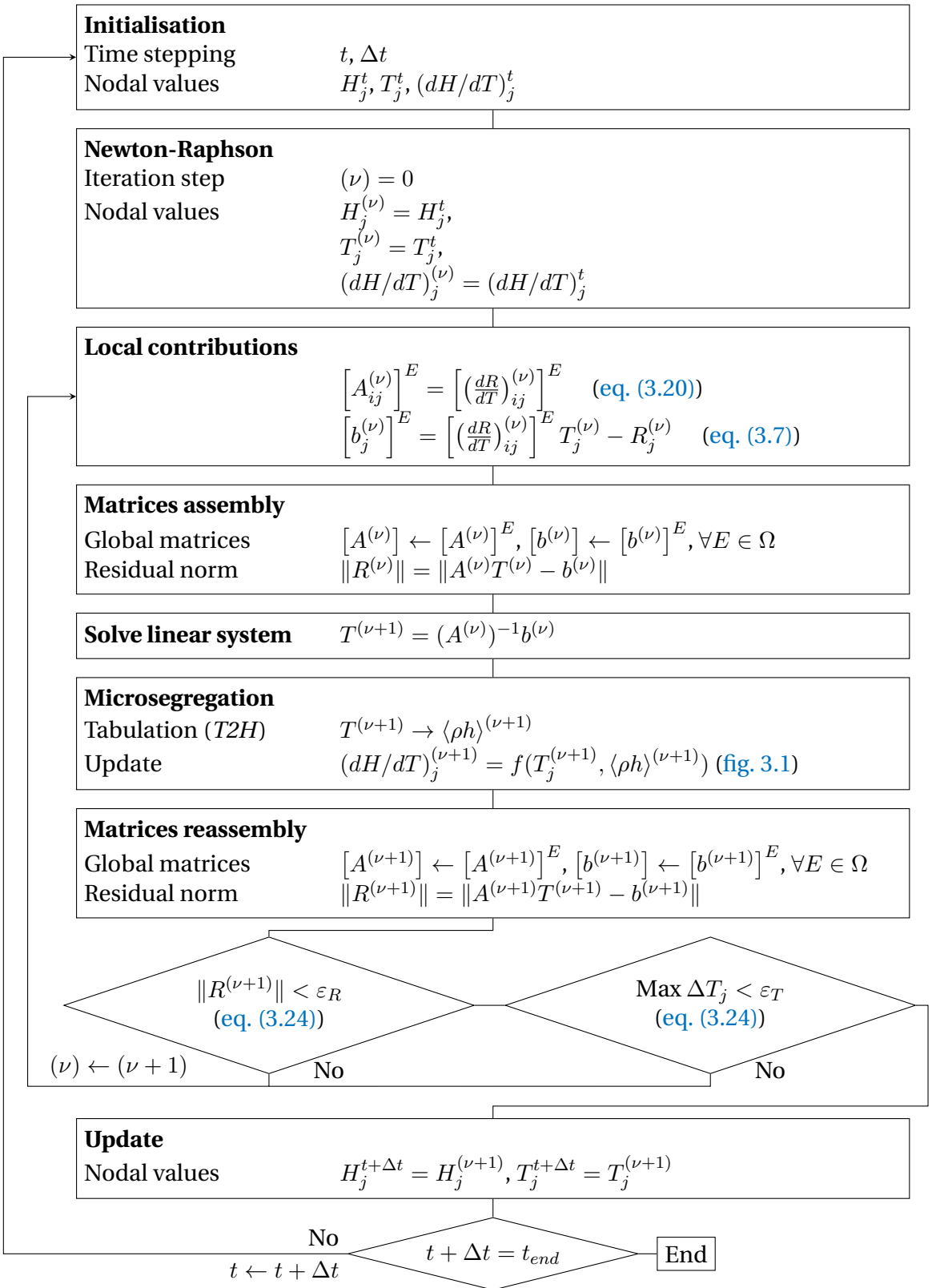


Fig. 3.3 – Resolution algorithm of the temperature-based solver.

Chapter 3. Energy balance with thermodynamic tabulations



Fig. 3.4 – Resolution algorithm of the enthalpy-based solver.



Fig. 3.5 – Computed unidirectional heat diffusion during solidification of an Al-7 wt.% Si alloy using (orange) the enthalpy method and (black) the temperature method, comparison being made for (a) cooling curves and (b) the liquid fraction history. Each curve corresponds to a position along the sample, from 0 cm (cooling side) to 10 cm (insulated side), with 2 cm spacing between the positions.

Chapter 3. Energy balance with thermodynamic tabulations

Table 3.2 – Parameters for the pure diffusion test case with an Al-7 wt.% Si alloy presented in fig. 3.5

Parameter	Symbol	Value	Unit
Nominal composition	$\langle w \rangle_0$	7	wt.%
Liquidus temperature	T_l	618	°C
Eutectic temperature	T_E	577	°C
Segregation coefficient	k	0.13	—
Liquidus slope	m_l	-6.5	K wt.% ⁻¹
Heat capacity (liquid and solid)	ρC_p	2.6×10^6	J m ⁻³ K ⁻¹
Enthalpy of fusion	ρL	9.5×10^8	J m ⁻³
Thermal conductivity (liquid and solid)	κ	70	W m ⁻¹ K ⁻¹
Heat transfer coefficient	h_{ext}	500	W m ⁻² K ⁻¹
External temperature	T_{ext}	100	°C
Initial temperature	T_0	800	°C
Ingot length		0.1	m
FE mesh size		10^{-3}	m
Time step	Δt	0.1	s
Convergence criterion (residual)	ε_R	10^{-6}	—
Convergence criterion (temperature)	ε_T	10^{-2}	K

yields some other consequences on the mass balance and the liquid momentum conservation. In the latter, a Darcy term is added to take into account the dissipative interfacial stress in the porous-like mushy zone. Its main parameter is the permeability of the mushy zone, K . It is considered isotropic, hence reducing to a scalar which is given by the Carman-Kozeny relation, based on the secondary dendrite arm spacing λ_2 : $K = \frac{g^l l^3 \lambda_2^2}{180(1-g^l)^2}$. The liquid density being taken constant, its spatial variations as a function of temperature and average composition are still needed to compute thermosolutal convection forces. For that purpose, the Boussinesq approximation (eq. (4.7)) is used, considering the thermal β_T and solutal $\beta_{\langle w \rangle^l}$ expansion coefficients and a reference density, ρ_{ref} , defined at a reference temperature T_0 and reference composition w_0^l . Values for the references are taken at the liquidus temperature and the nominal composition of the alloy, $\langle w \rangle_0$ [Carozzani et al. 2013]. More details about the FE formulation can be found in the PhD work of Rivaux [2011] and Carozzani [2012]. The Tsolver's ability to be coupled with various physical phenomena like macrosegregation and fluid flow in porous medium is displayed in this test case. Details about fluid flow resolution will not be given in this section, but rather in the next chapter. It



Fig. 3.6 – Experimental cooling curves overlap with the results of the 3D FE convection-diffusion simulation. The left (LHE) and right (RHE) heat exchangers impose the boundary temperature in the experiment.

consists of a solidification benchmark where a 10 cm width \times 6 cm height \times 1 cm thick cavity containing a Sn-3 wt.% Pb melt is cooled down from its two narrowest vertical sides using heat exchangers (LHE: left heat exchanger, RHE: right heat exchanger). The experiment, inspired by [Hebditch et al. \[1974\]](#) similar set up, has been revisited by [Hachani et al. \[2012\]](#) who performed the solidification with better controlled conditions and using an increased number of samples for composition analysis. Recently, a successful attempt to simulate the experiment was carried out by [Carozzani et al. \[2013\]](#) relying on an enthalpy resolution. All details regarding geometry, finite element discretization, material properties and boundary conditions can be found in the latter reference. For this computation, solidification paths, phase compositions and phase enthalpies were determined by a thermodynamic module dedicated to equilibrium calculations for binary alloys. The 3D simulation results in [fig. 3.6](#) show a satisfactory agreement with the experimental temperature measurements recorded at mid heights of the cavity and uniformly distributed along its width [[Carozzani et al. 2013](#)]. In fact, simulation results with the Tsolver and the Hsolver were found to be almost superimposed, as shows [fig. 3.6](#). Further comparison is made between both solvers, as shows [fig. 3.7](#), where the average composition, liquid fraction and temperature fields are extracted from a cut plane halfway through the ingot. On the same figure, if we compare the composition, we notice that the solidified part (right side) has basically the same segregation pattern, while in the convected liquid has a slightly different solute distribution. As for the extent of the mushy zone, we observe that liquid fraction contours are very close, indicating that temperature distributions and interdendritic segregation are also close between both solvers predictions. Regarding the computation, the Tsolver resolution proves to be faster than the Hsolver used by [Carozzani et al. \[2013\]](#): a process time of 7000s required a computation time of 90 hours 13 minutes compared to 114 hours 21 minutes spent by the enthalpy resolution with 32 cores on the same cluster. The gain factor is about 20%.

3.5 Application: multicomponent alloy solidification

We have shown that the efficiency of the temperature-based resolution resides in its performance when combined with thermodynamic tabulations. A multicomponent alloy consists of at least two solute elements, and therefore the tabulation size increases, hence the number of search operations also increases. To demonstrate the speed-up ability of the temperature-based approach while predicting all phase transformations during macrosegregation caused solely by mass diffusion, we consider the solidification of a ternary alloy, Fe-2 wt.% C-30 wt.% Cr. In order to neglect fluid flow

3.5. Application: multicomponent alloy solidification



Fig. 3.7 – Comparison of 3D simulation results: average composition, liquid fraction and temperature at $t = 3000$ s for Tsolver and Hsolver.

resolution, we assume that solidification in this case is so slow that no forces are generated inside the melt, while additionally all buoyancy forces are also neglected, so no momentum conservation is solved in this section. As illustrated in [fig. 3.9a](#), the alloy domain has a cylinder shape close to 3-inch height \times 1-inch diameter. Exact values are reported in [table 3.3](#) with all material properties, initial and boundary conditions, as well as numerical parameters for the simulations. The melt steel is initially at 1395 °C. The temperature of the bottom surface is imposed with a constant decreasing rate of 0.1 K s⁻¹ starting with 1380 °C, i.e. 40 °C higher than the nominal liquidus temperature, as shown in [fig. 3.9b](#). The other surfaces are kept adiabatic. The cylinder is held in a vertical position. [fig. 3.8](#) also provides the transformation path of the alloy at nominal composition, i.e. assuming no macrosegregation and full thermodynamic equilibrium as computed with ThermoCalc and the TCFE6 database [[TCFE6 2010; Andersson et al. 2002](#)]. A total of 5 phases need to be handled, the characteristic temperature for their formation being reported in [fig. 3.9b](#).

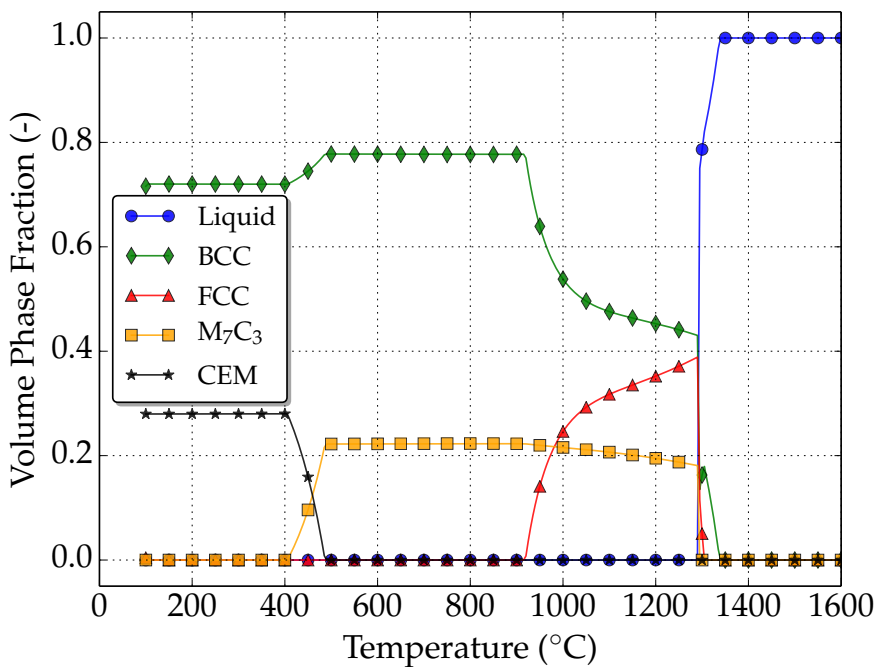


Fig. 3.8 – Thermodynamic mapping [[TCFE6 2010; Andersson et al. 2002](#)] of the transformation path for the Fe-2 wt.% C-30 wt.% Cr at nominal composition.

3.5.1 Tabulations

Full thermodynamic equilibrium is considered in the present case. Due to macrosegregation, the average composition is expected to continuously vary in time and space

during casting. Transformation paths are thus determined a priori for a set of average compositions around the nominal value. Hence, carbon content varies in the interval [1.8 wt.%, 2.2 wt.%] while chromium content variation is in the interval [27 wt.%, 33 wt.%]. The offset of $\pm 10\%$ with respect to the nominal composition value allows tabulating relatively small composition steps to ensure a fairly accurate mapping when compared to the corresponding ternary phase diagram. The average composition step is 0.04 wt.% for carbon and 0.6 wt.% for chromium, thus representing 2% intervals with respect to the nominal composition. The temperature varies in the interval [100 °C, 1600 °C] by 5 °C steps. For each triplet (carbon content in wt.% C, $\langle w_C \rangle_0$, chromium content in wt.% Cr, $\langle w_{Cr} \rangle_0$, temperature in K) corresponds a phase fraction g^ϕ and a pair of intrinsic phase composition ($\langle w_{Cr} \rangle^\phi, \langle w_C \rangle^\phi$). For the 5 phases listed in [fig. 3.8](#) (LIQ=liquid, BCC=ferrite, FCC=austenite, M₇C₃=carbide, CEM=cementite), the enthalpy h^ϕ and density ρ^ϕ , are tabulated as functions of temperature and phase intrinsic composition. If this latter input lies between two tabulated values, a linear interpolation is performed to determine the output, i.e. phase enthalpy and density. With the advancement of solidification, the liquid is enriched with solute by macrosegregation, which enables new solidification paths. It means that the primary solidifying phase is not necessarily the same as when considering the nominal composition. For this reason, the tabulation approach is interesting inasmuch as it provides phase transformation paths and values of phase properties that are compatible with the system's actual composition. [Figure 3.10](#) summarizes the tabulated thermodynamic data for two sets of average composition for the considered ternary system. Note that in the present test case, phase densities are taken constant ($\rho^s = \rho^l = 6725 \text{ kg m}^{-3}$). Therefore they are not tabulated. With this assumption, no shrinkage occurs upon phase change.

3.5.2 Discussion

A first case is considered without macrosegregation, that is, all mechanical driving forces are bypassed, leading to a static melt. This is achieved by nullifying the thermal and solutal expansion coefficients, which is equivalent to a constant density in space and time, i.e. no Boussinesq force is considered. This way, the average composition may only vary due to diffusion in the liquid phase according to [eq. \(2.43\)](#) where the convection term is neglected. Diffusion is significantly small in the present case and can be neglected too. In such a case, the composition distribution maintains a homogeneous aspect throughout the sample during the entire cooling sequence. The phase transformations then are necessarily expected to follow the unique path shown in [fig. 3.8](#). After 407 s of cooling, the liquidus isotherm enters the bottom surface of



Fig. 3.9 – Configurations for directional casting of (a) a 1 inch diameter \times 3 inches height cylindrical domain for which (b) temperature-time conditions are imposed at its bottom surface.

the geometry and starts its upward propagation, marking the solidification onset. [Figure 3.11](#) presents the simulation results at 3 successive times for the distribution of the solute species and the temperature, as well as for the fraction of phases listed in [fig. 3.8](#). At 600 s, a fully liquid region is still largely present while the mushy zone is made of liquid plus the primary solid phase (ferrite). At 10 560 s, the sample is full solid, with fractions of ferrite and cementite that corresponds to the values read in [fig. 3.8](#) at low temperature. At the selected intermediate time, the presence of 4 phases is found. The solid region at the bottom of the cylinder is made of ferrite, austenite plus carbide, the temperature being still too high to permit the cementite to form. The mushy zone above the solid region is characterized by the presence of 3 phases due to a peritectic reaction taking place that progressively transform ferrite into austenite in the presence of liquid. It can be noticed that the phase fraction isovalues in [fig. 3.11](#) (at 600 s) are horizontal, owing this to two factors: the first is the temperature field, which varies unidirectionally from bottom to top, controlled by thermal diffusion, while the second is the uniform average composition throughout the sample due to the absence of convection. In fact both factors are consequences of the flow absence, which would transport heat and solute by advection, thus inevitably changing the phase distribution. The succeeding phase change is a solid-state transformation where α -ferrite and the carbide M_7C_3 react to form cementite at 490 °C at nominal composition, as shown in [fig. 3.9b](#). The reaction is relatively slow, ending with 28% of cementite and 72% of α -ferrite.

3.5. Application: multicomponent alloy solidification

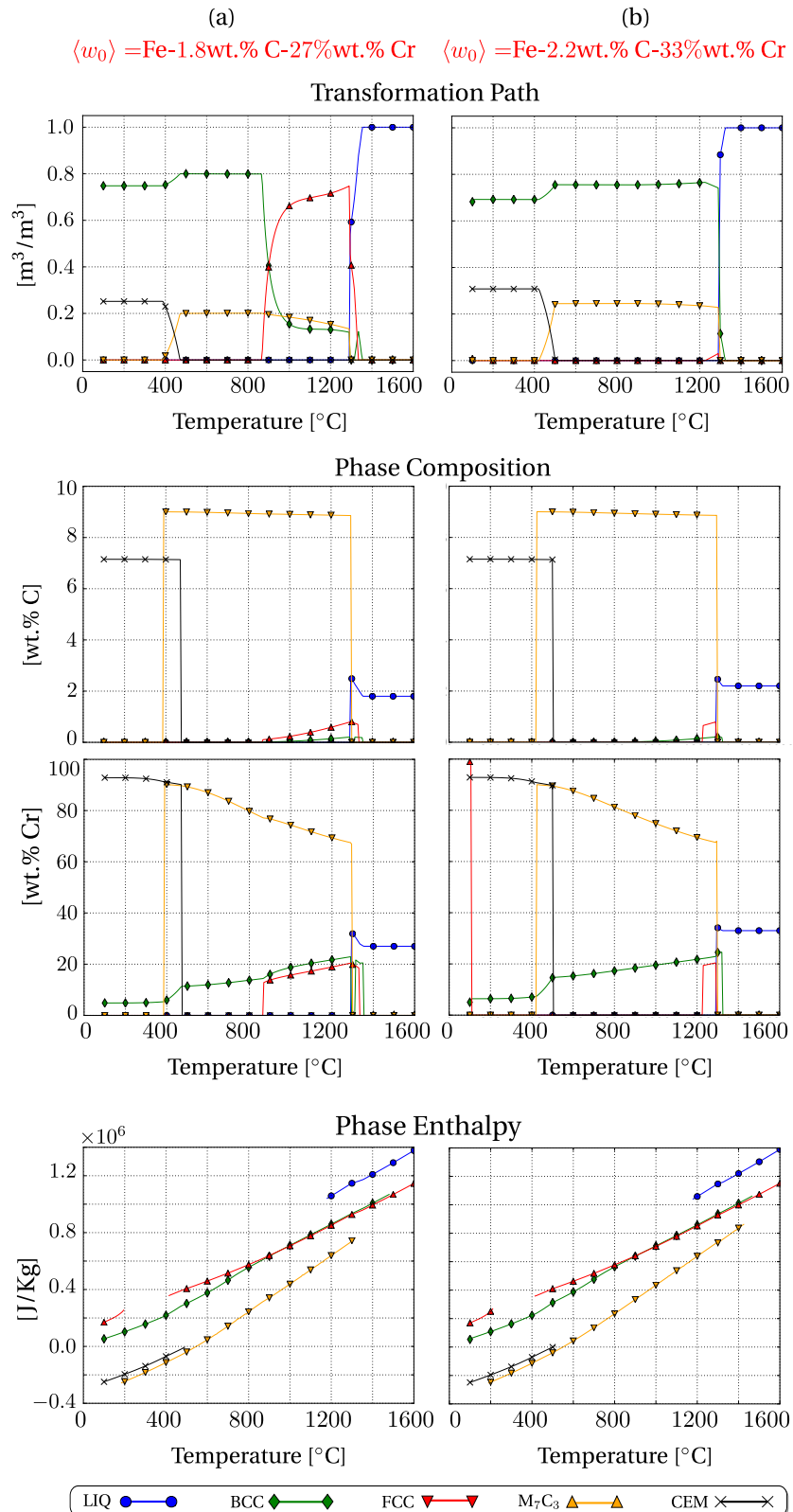


Fig. 3.10 – Tabulated thermodynamic data for the ternary system Fe-C-Cr alloy with software Thermo-Calc [Andersson et al. 2002] with database TCFE6 [TCFE6 2010]. The two columns represent two values of nominal average composition, for a) low carbon and chromium content and b) high carbon and chromium content. The effect of their variation on transformation paths, phase compositions and phase enthalpies is shown in the corresponding graphs.

Chapter 3. Energy balance with thermodynamic tabulations

Table 3.3 – Solidification parameters for the Fe-2 wt.% C-30 wt.% Cr alloy.

Parameter	Symbol	Value	Unit
Nominal composition	$\langle w_C \rangle_0$	2	wt.%
	$\langle w_{Cr} \rangle_0$	30	wt.%
Characteristic temperatures	T_{bottom}	fig. 3.9b	°C
Phase fraction	g^ϕ	Tabulations fig. 3.10	–
Phase enthalpy	$\langle h \rangle^\phi$	Tabulations fig. 3.10	–
Phase composition	$\langle w_C \rangle^\phi$	Tabulations fig. 3.10	wt.%
Phase composition	$\langle w_{Cr} \rangle^\phi$	Tabulations fig. 3.10	wt.%
Diffusion coefficients	$\langle D_C \rangle^l$	15×10^{-10}	$\text{m}^2 \text{s}^{-1}$
	$\langle D_{Cr} \rangle^l$	15×10^{-10}	$\text{m}^2 \text{s}^{-1}$
Dynamic viscosity	μ^l	2×10^{-3}	Pa s
Thermal expansion coefficient	β_T	8.96×10^{-5}	K^{-1}
Solutal expansion coefficient	$\beta_{\langle w_C \rangle^l}$	1.54×10^{-3}	wt.\%^{-1}
	$\beta_{\langle w_{Cr} \rangle^l}$	1.72×10^{-2}	wt.\%^{-1}
Thermal conductivity in the solid	$\langle \kappa \rangle^s$	40	$\text{W m}^{-1} \text{K}^{-1}$
Thermal conductivity in the liquid	$\langle \kappa \rangle^l$	28	$\text{W m}^{-1} \text{K}^{-1}$
Dendrite arm spacing	λ	60×10^{-6}	m
Density	ρ_0^l	6725	kg m^{-3}
Reference composition (carbon)	$\langle w_C \rangle_{\text{ref}}^l$	2	wt.%
Reference composition (chromium)	$\langle w_{Cr} \rangle_{\text{ref}}^l$	30	wt.%
Reference temperature	$\langle w_C \rangle_{\text{ref}}^l$	1377	°C
Initial temperature	T_0	1395	°C
Ingot diameter		25×10^{-3}	m
Ingot length		75×10^{-3}	m
FE mesh size		10^{-3}	m
Time step	Δt	0.1	s
Convergence criterion (residual)	ε_R	10^{-6}	–
Convergence criterion (temperature)	ε_T	10^{-2}	K

3.5. Application: multicomponent alloy solidification



Fig. 3.11 – : Upward solidification of a cylinder rod with a static liquid at 3 stages in a Fe-2 wt.% C-30 wt.% Cr. The left columns show the average composition and temperature distribution, while the right columns show the phase fractions.

Chapter 4

Macrosegregation with liquid metal motion

Contents

4.1	Introduction	70
4.2	Formulation stability	70
4.2.1	Stable mixed finite elements	70
4.2.2	Variational multiscale (VMS)	71
4.3	Navier-Stokes solver	72
4.3.1	Strong and weak formulations	72
4.3.2	Stabilisation parameters	76
4.3.3	Implementation	77
4.4	Application to multicomponent alloys	77
4.4.1	Results	80
4.5	Macroscopic prediction of channel segregates	83
4.5.1	Introduction	83
4.5.2	Experimental work	84
4.5.3	Macroscopic scale simulations	84
4.6	Meso-Macro prediction of channel segregates	91
4.6.1	Numerical method	91
4.6.2	Configuration	93
4.6.3	Effect of vertical temperature gradient	97
4.6.4	Effect of cooling rate	99
4.6.5	Effect of lateral temperature gradient	101
4.6.6	Mono-grain freckles	102

4.1 Introduction

Fluid flow is an important part, if not the most important, in understanding the evolution of a system undergoing phase change and chemical segregation. It is attributed to the convective transport in fluids where the variations time scale is much smaller than the remaining physics that are characterised by smoother variations. To understand how fluid motion contributes to the heat and mass transfer, we have swiftly presented the momentum conservation equation in a solidifying liquid, [eq. \(2.41\)](#). In this chapter, we will first give quick overview of the numerical treatment of this system of Navier-Stokes equations, then comment on some computational aspects such as the choice of a suitable time step and the conditions that impose minimum and maximum bounds on both time step and mesh size.

4.2 Formulation stability

A wide array of numerical methods can be used to solve systems like [eq. \(2.41\)](#). When speaking about Navier-Stokes equations, the choice can be narrowed to two famous approaches with some similarities: stable mixed finite element method and Variational MultiScale (VMS) method. When two finite element spaces are introduced (e.g. one for velocity and another for pressure), the essential *inf-sup* condition (also known as stability condition) determined by [Babuška \[1971\]](#) and [Brezzi \[1974\]](#) should be fulfilled. It states that the formulation is not well-posed if the both spaces have the same interpolation order. For instance, a P1/P1 element (i.e. P1 for velocity / P1 for pressure) cannot guarantee the stability of the Navier-Stokes solution since velocity and pressure are both linearly interpolated at the simplex vertices. However, the major difference between the previously mentioned formulations is the way in which the inf-sup condition is accounted for. Stable mixed finite elements are stable because they directly respond to the stability condition by enriching the velocity space, hence they fall under the category of Satisfying Babuška-Brezzi (SBB) methods. In contrast, methods like VMS belong to the Circumventing Babuška-Brezzi (CBB) category [[Barbosa et al. 1991](#)]. CBB methods rely on equal-order interpolations with additional stabilisation that circumvents the need to satisfy the stability condition. Further details about both formulation types are given in the next subsections.

4.2.1 Stable mixed finite elements

First introduced by [Arnold et al. \[1984\]](#), the MINI element is the key ingredient of this approach. This type of element introduces an additional degree of freedom for the

velocity field while keeping a linear interpolation for the pressure field, thus satisfying the Babuška-Brezzi condition with a richer velocity space. The additional degree, known as the *bubble* function, vanishes on the element's boundary. We may therefore speak of a P1+/P1 finite element in a velocity-pressure formulation. This stable formulation has been the de facto standard for solving fluid and solid mechanics for many years at CEMEE.

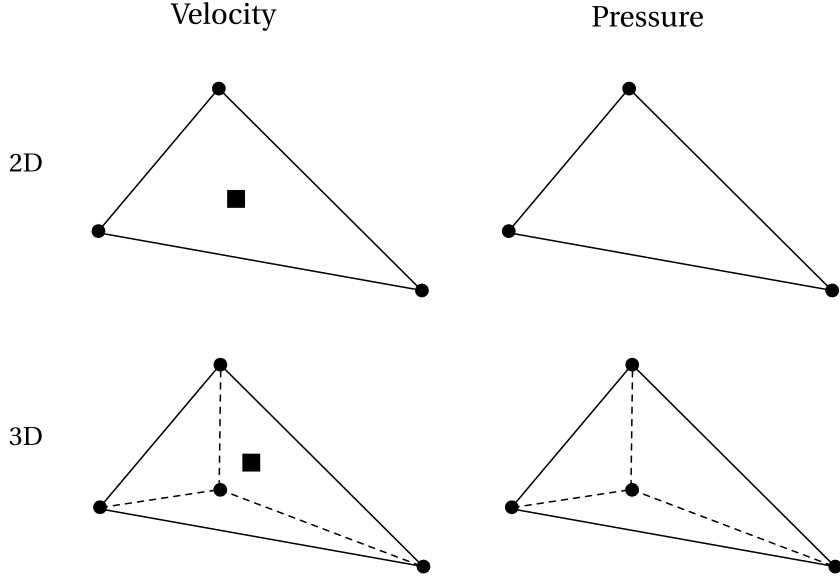


Fig. 4.1 – Schematic of 2D and 3D stable P1+/P1 finite elements, respectively triangle and tetrahedron, with velocity and pressure fields interpolation order. The dots represent the nodes while the squares represent the bubbles.

4.2.2 Variational multiscale (VMS)

As the name indicates, this approach considers two scales of phenomena: the coarse and fine scales. Applied to a velocity-pressure formulation, these fields are decomposed according to these scales as follows:

$$\langle \vec{v}^l \rangle = \langle \vec{v}^l \rangle_h + \tilde{\vec{v}}^l \quad (4.1)$$

$$p = p_h + \tilde{p} \quad (4.2)$$

where $\langle \vec{v}^l \rangle_h$ and p_h are the coarse scale velocity and pressure discretised on the finite element mesh (hence the subscript h), while the remaining terms represent the fine scale velocity and pressure that cannot be captured at the scale of the FE grid. Instead of defining a finer grid to model the effect of these terms, one can solve the fine scale equations obtained once [eqs. \(4.1\) and \(4.2\)](#) are injected in [eq. \(2.41\)](#) then use the

output in the coarse scale equations. Further technical details about the method and the equations are found in the PhD work of [Hachem \[2009\]](#).

The added value of the VMS method is the time gain that we get by incorporating the effect of the fine scale into the coarse scale physics without discretising on a finer grid, while maintaining the ability to predict localised fluid motion such as small vortices.

4.3 Navier-Stokes solver

In the present thesis, we chose to solve the fluid momentum conservation using a stabilised P1/P1 formulation with additional element-level integrals to add stability for convection-dominated terms, transient-dominated terms and pressure terms. The stabilisation techniques include the streamline upwind/Petrov-Galerkin (SUPG), pressure stabilising/Petrov-Galerkin (PSPG) and the least-squares on incompressibility constraint (LSIC) as a stabilisation framework introduced by [Tezduyar et al. \[1992\]](#). The global approach, more commonly known as SUPG-PSPG-LSIC, prevents the classical formulation instability coming from the linear equal-order interpolation functions.

It is important to note that the P1/P1 SUPG-PSPG-LSIC approach is slightly different than a VMS approach as the derivation of stabilising terms in the latter comes from a physical interpretation of two different length scales, a resolved coarse scale and an unresolved fine scale. The incorporation of the fine-scale equation within the coarse-scale one results in additional stabilising terms, while in the current approach these terms come from a mathematical analysis based on limiting cases of diffusion or advection. The final stabilising scheme is however very similar. The Navier-Stokes solver developed by [Hachem et al. \[2010\]](#) and [Rivaux \[2011\]](#) is a convenience choice to solve a stabilised Navier-Stokes system with Darcy terms.

4.3.1 Strong and weak formulations

The strong form of the fluid mechanics problem has been previously established in chapter 2 ([section 2.1.1](#)), where we obtained the following system of mass and liquid

momentum conservation equations:

$$\begin{cases} \rho_0^l \left(\frac{\partial \langle \vec{v}^l \rangle}{\partial t} + \frac{1}{g^l} \vec{\nabla} \cdot (\langle \vec{v}^l \rangle \times \langle \vec{v}^l \rangle) \right) = \\ - g^l \vec{\nabla} p^l - \vec{\nabla} \cdot (2\mu^l \langle \vec{\varepsilon}^l \rangle) - g^l \mu^l \mathbb{K}^{-1} \langle \vec{v}^l \rangle + g^l \rho^l \vec{g} \\ \nabla \cdot \langle \vec{v}^l \rangle = 0 \end{cases} \quad (4.3)$$

The strong solution consists of finding the pair $(\langle \vec{v}^l \rangle, p^l)$ of the previous system, when the following essential (Dirichlet type) and natural (Neumann type) boundary conditions are applied :

$$\langle \vec{v}^l \rangle = \vec{v}_0 \text{ on } \partial\Omega_{\text{Dirichlet}} \quad (4.4)$$

$$\langle \vec{\sigma}^l \rangle \cdot \vec{n} = \vec{N} \text{ on } \partial\Omega_{\text{Neumann}} \quad (4.5)$$

$$\text{with } \partial\Omega_{\text{Dirichlet}} \cup \partial\Omega_{\text{Neumann}} = \partial\Omega \quad (4.6)$$

We can comment on the strong form with the following recap points:

1. the liquid metal is Newtonian with a dynamic viscosity denoted μ^l
2. the metal is incompressible, therefore the liquid and solid densities are constant and equal (hence ρ_0^l in the inertial term) and the mass balance reduces to $\nabla \cdot \langle \vec{v}^l \rangle = 0$
3. the Boussinesq approximation is used to compute the thermosolutal buoyancy force in the melt via the term $g^l \rho^l \vec{g} = g^l \rho^l (T, \langle w_i \rangle^l) \vec{g}$, where $\rho^l (T, \langle w_i \rangle^l)$ can be either tabulated as a function of temperature and liquid composition for each solute i , or directly approximated by:

$$\rho^l = \rho_0^l \left(1 - \beta_T (T - T_0) - \sum_{i=1}^{\text{nb species}} \beta_{w_i^l} (\langle w_i \rangle^l - \langle w_i \rangle_0^l) \right) \quad (4.7)$$

where β_T and $\beta_{w_i^l}$ are respectively the thermal and solutal expansion coefficients, while T_0 and $\langle w_i \rangle_0^l$ represent a reference temperature and a reference liquid composition for each chemical species, respectively.

The weak form treated by the VMS solver derives from the strong form by multiplying

Chapter 4. Macrosegregation with liquid metal motion

by test functions for velocity and pressure belonging to these functional spaces:

$$\begin{aligned} v &= \left\{ \vec{u}, \quad \vec{u} \in (\mathcal{H}^1(\Omega))^d \mid \vec{u} = \vec{v}_0 \text{ on } \partial\Omega \right\} \\ v^0 &= \left\{ \vec{u}, \quad \vec{u} \in (\mathcal{H}^1(\Omega))^d \mid \vec{u} = \vec{0} \text{ on } \partial\Omega \right\} \\ \varrho &= \{q, \quad q \in L^2(\Omega)\} \end{aligned}$$

where d stands for the space dimension. Then, based on these definitions, we write the advective upwinding stabilised test function for the velocity, \vec{U} :

$$\vec{U} = \vec{u} + \tau_{\text{SUPG}} \vec{\nabla} \vec{u} \cdot \left\langle \vec{v}^l \right\rangle_{\Omega_E} \quad (4.8)$$

τ_{SUPG} is an elemental stabilising parameter for advection-dominated terms and $\left\langle \vec{v}^l \right\rangle_{\Omega_E}$ is the superficial velocity in the element Ω_E , calculated by regular P1 interpolation:

$$\left\langle \vec{v}^l \right\rangle_{\Omega_E} = \frac{\sum_{i=1}^D \left\langle \vec{v}^l \right\rangle_i}{D} \quad (4.9)$$

Moreover, we need the following operators in order to simplify the notation of element-based variational integrals:

$$[a, b] = \int_{\Omega_E} ab \, d\Omega \quad (4.10)$$

$$[c, d]^* = \int_{\partial\Omega_E} cd \, d\Gamma \quad (4.11)$$

Finally, the SUPG-PSPG-LSIC stabilised weak formulation writes:

$$\left\{ \begin{array}{l} \forall \vec{u} \in v^0 \\ \left[\left(\frac{\rho_0^l}{g^l} \frac{\partial \langle \vec{v}^l \rangle}{\partial t} \right), \vec{U} \right] + \left[\left(\frac{\rho_0^l}{g^{l2}} (\bar{\nabla} \langle \vec{v}^l \rangle) \langle \vec{v}^l \rangle \right), \vec{U} \right] + \left[\left(\frac{2\mu^l}{g^l} \right), \bar{\bar{\varepsilon}}(\langle \vec{v}^l \rangle) : \bar{\bar{\varepsilon}}(\vec{U}) \right] \\ + \left[\left(\mu^l \mathbb{K}^{-1} \langle \vec{v}^l \rangle \right), \vec{U} \right] - \left[\left(\rho^l \vec{g} \right), \vec{U} \right] - [p, \nabla \cdot \vec{U}] - \left[\frac{\vec{N}}{g^l}, \vec{U} \right]^* \\ + \left[\tau_{\text{LSIC}}, \left(\rho_0^l \nabla \cdot \langle \vec{v}^l \rangle \nabla \cdot \vec{u} \right) \right] = 0 \\ \\ \forall q \in \varrho \\ \left[\nabla \cdot \langle \vec{v}^l \rangle, q \right] + \\ \left[\tau_{\text{PSPG}} \frac{\vec{\nabla} q}{\rho_0^l}, \left(\frac{\rho_0^l}{g^l} \frac{\partial \langle \vec{v}^l \rangle}{\partial t} + \frac{\rho_0^l}{g^{l2}} (\bar{\nabla} \langle \vec{v}^l \rangle) \langle \vec{v}^l \rangle + \mu^l \mathbb{K}^{-1} \langle \vec{v}^l \rangle - \rho^l \vec{g} \right) \right] = 0 \end{array} \right. \quad (4.12)$$

Replacing eq. (4.8) in eq. (4.12), we get the final weak form:

$$\left\{ \begin{array}{l} \forall \vec{u} \in v^0 \\ \left[\left(\frac{\rho_0^l}{g^l} \frac{\partial \langle \vec{v}^l \rangle}{\partial t} \right), \vec{u} \right] + \left[\left(\frac{\rho_0^l}{g^{l2}} (\bar{\nabla} \langle \vec{v}^l \rangle) \langle \vec{v}^l \rangle \right), \vec{u} \right] + \left[\left(\frac{2\mu^l}{g^l} \right), \bar{\bar{\varepsilon}}(\langle \vec{v}^l \rangle) : \bar{\bar{\varepsilon}}(\vec{u}) \right] \\ + \left[\left(\mu^l \mathbb{K}^{-1} \langle \vec{v}^l \rangle \right), \vec{u} \right] - \left[\left(\rho^l \vec{g} \right), \vec{u} \right] - [p, \nabla \cdot \vec{u}] - \left[\frac{\vec{N}}{g^l}, \vec{u} \right]^* \\ + \left[\tau_{\text{SUPG}} \bar{\nabla} \vec{u} \cdot \langle \vec{v}^l \rangle_{\Omega_E}, \left(\frac{\rho_0^l}{g^l} \frac{\partial \langle \vec{v}^l \rangle}{\partial t} + \frac{\rho_0^l}{g^{l2}} (\bar{\nabla} \langle \vec{v}^l \rangle) \langle \vec{v}^l \rangle + \mu^l \mathbb{K}^{-1} \langle \vec{v}^l \rangle + \vec{\nabla} p^l - \rho^l \vec{g} \right) \right] \\ + \left[\tau_{\text{LSIC}}, \left(\rho_0^l \nabla \cdot \langle \vec{v}^l \rangle \nabla \cdot \vec{u} \right) \right] = 0 \\ \\ \forall q \in \varrho \\ \left[\nabla \cdot \langle \vec{v}^l \rangle, q \right] + \\ \left[\tau_{\text{PSPG}} \frac{\vec{\nabla} q}{\rho_0^l}, \left(\frac{\rho_0^l}{g^l} \frac{\partial \langle \vec{v}^l \rangle}{\partial t} + \frac{\rho_0^l}{g^{l2}} (\bar{\nabla} \langle \vec{v}^l \rangle) \langle \vec{v}^l \rangle + \mu^l \mathbb{K}^{-1} \langle \vec{v}^l \rangle + \vec{\nabla} p^l - \rho^l \vec{g} \right) \right] = 0 \end{array} \right. \quad (4.13)$$

4.3.2 Stabilisation parameters

Several expressions for τ_{SUPG} were derived by Tezduyar et al. [1992] and Tezduyar et al. [2000], from which we retain the following:

$$\tau_{\text{SUPG}} = \left(\frac{1}{\tau_{\text{advec}}^2} + \frac{1}{\tau_{\text{diff}}^2} + \frac{1}{\tau_{\text{trans}}^2} \right)^{-1/2} \quad (4.14)$$

where we use three parameters τ_{advec} , τ_{diff} and τ_{trans} having time as unit (*s*) that stabilise respectively advection-dominated, diffusion-dominated and transient-dominated regimes, given by:

$$\tau_{\text{advec}} = \frac{h_{\text{stream}}}{2\|\langle \vec{v}^l \rangle_{\Omega_E}\|} \quad (4.15)$$

$$\tau_{\text{diff}} = \frac{h_{\text{stream}}^2}{4\nu^l} \quad (4.16)$$

$$\tau_{\text{trans}} = \frac{\Delta t}{2} \quad (4.17)$$

where $h_{\text{stream}} = 2\|\langle \vec{v}^l \rangle_{\Omega_E}\| \left(\langle \vec{v}^l \rangle_{\Omega_E} \cdot \vec{\nabla} \mathcal{P} \right)$ is the element length in the stream direction, computed using the local superficial velocity and the interpolation functions \mathcal{P}_j relative to each local node j , ν^l is the liquid's kinematic viscosity ($\text{m}^2 \text{s}^{-1}$) and Δt is the time step. The transient term stabilisation was initially derived for Navier-Stokes equations without Darcy term. As the latter has a significant role in the weak form eq. (4.13), it needs to be stabilised. The current thesis is based on several past projects that either considered eq. (4.17) like Liu [2005] or modified it like Gouttebroze [2005] and Rivaux [2011] to take account the Darcy term, giving the term:

$$\tau_{\text{trans-darcy}} = \frac{\Delta t}{2 \left(1 + \Delta t \frac{\mu^l}{\rho_0^l \mathbb{K}} \right)} \quad (4.18)$$

In the literature, no substantial references were found to backup the formulation of eq. (4.18), it will be used in the current work though. It is worth mentioning that Zabaras et al. [2004] has invoked the necessity to stabilise Darcy terms in a generalised Navier-Stokes/Darcy P1/P1 formulation, and introduced what they call Darcy-Stabilising/Petrov-Galerkin (DSPG), using local non-dimensional numbers of Darcy (Da) and Prandtl (Pr) numbers expressing respectively the ratio of local permeability to a characteristic length L and the ratio of momentum diffusivity, ν^l , to heat diffusivity

4.4. Application to multicomponent alloys

in the liquid, α^l :

$$\tau_{\text{darcy}} = \frac{Da}{Pr} \left(\frac{g^l}{1 - g^l} \right)^2 = \frac{\alpha^l \mathbb{K}}{\nu^l L^2} \left(\frac{g^l}{1 - g^l} \right)^2 \quad (4.19)$$

Last, the definitions of the remaining stabilisation parameters are given as follows:

$$\tau_{\text{PSPG}} = \tau_{\text{SUPG}} = \left(\left(\frac{2 \|\langle \vec{v}^l \rangle_{\Omega_E} \|}{h_{\text{stream}}} \right)^2 + \left(\frac{4\nu^l}{h_{\text{stream}}^2} \right)^2 + \left(\frac{2 \left(1 + \Delta t \frac{\mu^l}{\rho_0^l \mathbb{K}} \right)}{\Delta t} \right)^2 \right) \quad (4.20)$$

$$\tau_{\text{LSIC}} = \frac{h_{\text{stream}}}{2} \|\langle \vec{v}^l \rangle_{\Omega_E} \| Z(Re_{\Omega_E}) \quad (4.21)$$

with $Z(Re_{\Omega_E})$ being a local Reynolds-dependant function that evaluates to:

$$Z(Re_{\Omega_E}) = \begin{cases} Re_{\Omega_E}/3 & \text{if } Re_{\Omega_E} \leq 3 \\ 1 & \text{if } Re_{\Omega_E} > 3 \end{cases} \quad (4.22)$$

and

$$Re_{\Omega_E} = \frac{\|\langle \vec{v}^l \rangle_{\Omega_E} \| h_{\text{stream}}}{2\nu^l} \quad (4.23)$$

4.3.3 Implementation

The final matrix definition of the weak form of eq. (4.3) is given by:

$$\begin{pmatrix} A_{vv} & A_{vp} \\ A_{pv} & A_{pp} \end{pmatrix} \begin{pmatrix} \langle \vec{v}^l \rangle \\ p^l \end{pmatrix} = \begin{pmatrix} B_v \\ B_p \end{pmatrix} \quad (4.24)$$

CFL condition

Integration order

Using P1 linear elements implies a P2 integration ? what are the advantages (time) and limitations ?

4.4 Application to multicomponent alloys

In the previous chapter, we have considered a static melt upon solidification of multi-component alloy. The artificial consideration of a still flow is dropped in this chapter,

hence taking into account macrosegregation caused by fluid motion, using realistic values of the expansion coefficients given in [table 3.3](#). In the real conditions, the melt is in constant motion and knowing that the carbon and chromium solutes have lightening effects on the liquid at nominal composition, the density inversion resulting from the composition gradient in the interdendritic liquid, may cause flow instability (segregation plumes) at the solidification front. While the selected alloy is a steel, this application is also representative of directional cooling in a single crystal casting, e.g. for nickel-base superalloys [[Beckermann et al. 2000](#)]. Solidification of this class of alloys is carefully controlled so as to prevent any freckle-type defect to exist in the as-cast state. In this section, we consider the same simulation parameters defined in [table 3.3](#) as well the geometry and thermal boundary conditions previously defined in [fig. 3.9](#). Moreover, we solve the liquid momentum conservation equation, with non-slip boundary conditions on all external sides of the cylinder.

4.4. Application to multicomponent alloys

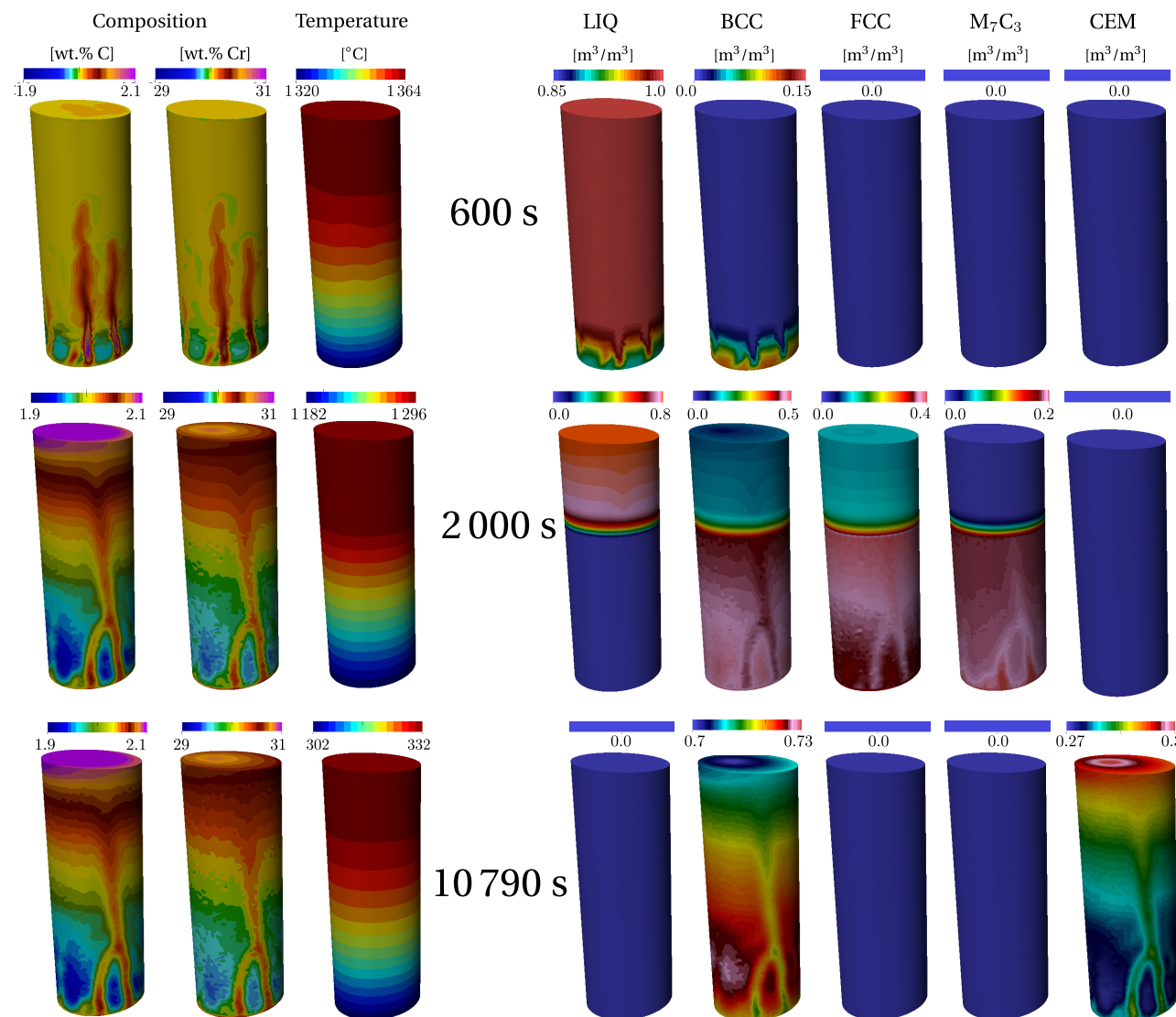


Fig. 4.2 – : Upward solidification of a cylinder rod at 3 stages showing the metallurgical consequences of macrosegregation Fe-2 wt.% C-30 wt.% Cr. The left columns show the average composition and temperature distribution, while the right columns show the phase fractions.

4.4.1 Results

Solidification starts at 407 s when the cylinder's bottom base temperature reaches the liquidus temperature of the alloy. In fact, the solidification onset is the same as in the pure diffusion case in [fig. 3.11](#), since the average composition remains unchanged for an entirely liquid domain (assuming an initially infinite solute mixing in the melt). As shown in [fig. 4.2](#) at 600 s, the first solid phase to form remains ferrite. We can also see solute-rich channels forming in the mushy zone and solute plumes rising in the melt above the mushy zone due to a subsequent upward flow. It is actually caused by the thermosolutal buoyancy force created by the carbon and chromium solutes. Such phenomenon could delay solidification inside liquid-rich channels and results in a freckling defect [Felicelli et al. 1991] on the surface of the cylinder as well as inside, as shown later in this section. As solidification proceeds, the liquid becomes more enriched with solute and the peritectic reaction forming the austenite phase is reached. However, for very large enriched melt, it can also be observed that primary solidification proceeds with the austenite phase rather than the ferrite phase. The carbide phase can also form with the austenite phase at some locations. These observations correspond to a simulation time of 2000 s in [fig. 4.2](#). Solidification ends at around 2475 s, the last liquid solidifying at the cylinder's top surface, where the average composition reaches a maximum of Fe-2.151 wt.% C-30.633 wt.% Cr, i.e. a relative positive macrosegregation, $(\langle w_i \rangle - \langle w_i \rangle_0) / \langle w_i \rangle_0$, of 7.5% for carbon and 2.1% for chromium. The fact that the maximum average composition is observed at the top, is verified in [fig. 4.3a](#) which shows the composition map in a 2D vertical slice through the longitudinal axis of the cylinder. We can also see it in [fig. 4.3b](#) where the relative composition profile are plotted at the end of the cooling process along the longitudinal cylinder axis Z-Z' and along the axis of the segregated channel, F-F'. The negative segregation up to 1 cm from the chill corresponds to the solute depletion caused by the first solid formation. The subsequent solidification enriches further the liquid; hence the solid composition also increases. The composition evolution trend for both solutes is similar: an overall rise until positive segregation is achieved above 5 cm from the chill. The positive macrosegregation intensifies when the profile is chosen at the center of the segregated channel, negative segregation then becoming less pronounced. Beyond 2475 seconds, no variations of the average composition maps are observed since solute diffusion in the solid phases is neglected. Nonetheless, as temperature decreases, solid-state transformations are still possible as for the case with no macrosegregation. The formation of a cementite phase begins at the cylinder base at 8843 s with a temperature of 496.9 °C. At about 9293 s, the isotherm 488.5 °C reaches the top surface. This temperature value is the local cementite solvus temperature. The difference in



Fig. 4.3 – (a) average composition map on a vertical section inside the sample, with (b) relative macrosegregation profiles on the vertical revolution axis.

the solvus temperature between the bottom and top surfaces is due macrosegregation. Macrosegregation also explains the variation in the cementite content. The solid state transformation ends shortly before 10 500 s. The influence of the solidification process is clear on the final macrosegregation pattern, hence the final phase distribution. This is better illustrated by drawing the time evolution of phase fractions at the center of the bottom and top surfaces of the cylinder in fig. 4.4. With no macrosegregation, in fig. 4.4a, the final distribution of the phases is the same at time 12 000 s, while with macrosegregation, in fig. 4.4b, variations of the cementite and ferrite are revealed. The segregated channels inside the cylinder and on the boundary, are often termed "freckles" when they consist of visible equiaxed grains [Copley et al. 1970]. This defect is marked by a noticeable gradient of composition and phase fractions, possibly changing the mechanical properties in the channels, hence the overall mechanical behaviour of the alloy. The coupling of the Tsolver with thermodynamic tabulations is thus demonstrated. It shows the ability to predict complex solidification paths, even if only at equilibrium. As for the computation time, the Tsolver resolution performed better: 500 seconds of solidification required 6 hours 14 minutes compared to 8 hours 6 minutes spent by the enthalpy resolution with 12 cores on the same machine. The gain factor is about 22%.



(a)



(b)

Fig. 4.4 – History of phase fraction (a) without macrosegregation and (b) with macrosegregation at the center of the (plain) bottom and (dashed) top surfaces of the cylinder surfaces, extracted from simulations displayed in (a) [fig. 3.11](#) and (b) [fig. 4.2](#).

4.5 Macroscopic prediction of channel segregates

4.5.1 Introduction

We have seen in the previous multicomponent solidification test case, a formation of segregated channels in the cylinder. This defect manifests itself as a composition inhomogeneity that is highly non-isotropic. A typical description of its morphology would consider a channel with a diameter proportional to few primary dendrite arm spacing and a length that could vary from millimeters to centimeters. These “worm”-like shapes could form during directional solidification of cast parts designed for engine applications, particularly in Nickel-base superalloys [Giamei et al. 1970; Beckermann et al. 2000; Genereux et al. 2000; Schneider et al. 1997]. In the latter situation, the channels are filled with a chain of small equiaxed crystals, thus referring to the term “freckle”. In large steel ingots, these channel defects are also related to A- and V-segregates [Pickering 2013].

Considering a binary alloy with a partition coefficient less than unity and having a negative liquidus slope, freckles may form by the following mechanisms: i) solute partitioning occurs at the scale of dendrite arms and solute is rejected in the melt, ii) local composition gradients are intensified resulting in an increase of the solutal buoyancy force in the mushy zone, iii) solute-rich pools are formed, causing segregation chimneys and convective plumes in the melt, iv) which lead to partial remelting and transport of dendrites, continuous solute feeding and locally delayed solidification, and finally v) accumulation of fragments and/or equiaxed crystals in the chimneys before the end of solidification.

Because it is of prime importance to control the occurrence of channel segregation, several attempts have been made from the late 1960’s [Flemings et al. 1967; Flemings et al. 1968a; Flemings et al. 1968b] to the early 2000’s [Ramirez et al. 2003] to understand it and characterise it by deriving freckling criteria. These studies are summarized in [Auburtin 1998]. One of the reasons for only considering freckling criteria is that direct realistic simulations of the formation of freckles in a casting geometry are still difficult. Indeed, experimental observations show that it requires a satisfying description of the microstructure together with the 3D convective flow controlled by the cooling conditions of the complete cast part [Shevchenko et al. 2013]. Such information is not accessible yet. Only simulations in representative simple cuboid or cylindrical domains are usually achieved [Felicelli et al. 1991; Felicelli et al. 1998; Kohler 2008; Guo et al. 2003], except when considering small volume casting [Desbiolles et al. 2003]. They are usually limited to unstable thermosolutal convection without or with little regard to the microstructural features. Considering the spatial resolution of the de-

fect, being for example of the order of the primary dendrite arm spacing, a fluid flow computation in the 3D casting part is also very demanding and not common in the literature. Among other criteria, the dimensionless Rayleigh number has been identified as a good indicator for the occurrence of segregation channels or a subsequent freckle defect. The dependence of freckling tendency on the Rayleigh number has been studied numerically and compared to experimental observations, as done by [Ramirez et al. 2003].

4.5.2 Experimental work

An interesting experimental work on directional solidification of In-75 wt.% Ga featuring in-situ X-ray monitoring has been recently carried out by Shevchenko et al. [2013]. The comparison with numerical modelling is paramount for two main reasons: firstly, the in-situ technique allows to follow solidification in real-time and offers visual description of the system behaviour: grain morphology, composition evolution, effect on fluid flow in the mushy zone and chimney initiation, as well as other modelling input data such as dendritic and eutectic nucleation undercooling; secondly, an indium-gallium system is more representative of metallic alloy solidification than the widely used organic systems, e.g. the succinonitrile-acetone mixture that exhibits alloy-like dendritic formation in its growth stage. Further information with respect to the experimental hardware, procedure and data analysis can be found in [Boden et al. 2008; Shevchenko et al. 2013].

4.5.3 Macroscopic scale simulations

Configuration

The focus of this section is on qualitative comparison between numerical simulation and the previously mentioned experiment. The experimental cell geometry shown in fig. 1.7c is hexagonal. With adiabatic lateral sides, it results in a bending of the isotherm surfaces as shown in the experiment. The metallic cooling plates shown in fig. 4.5a partly compensate for this effect. However, a residual horizontal component of the temperature gradient remains. To qualitatively replicate this effect while simplifying the cell geometry, a 22 mm × 22 mm × 1 mm cuboid cell is considered with small cooling fluxes on its lateral vertical side surfaces computed using a constant heat transfer coefficient, h_{ext} , and a constant environment temperature, T_{ext} . Temperatures at the bottom and top surfaces, respectively T_{Top} and T_{Bottom} , are imposed in a way to maintain a constant vertical gradient, G , thus linearly decreasing over time with the same cooling rate R . Both square faces of the geometry, having an area of

4.5. Macroscopic prediction of channel segregates

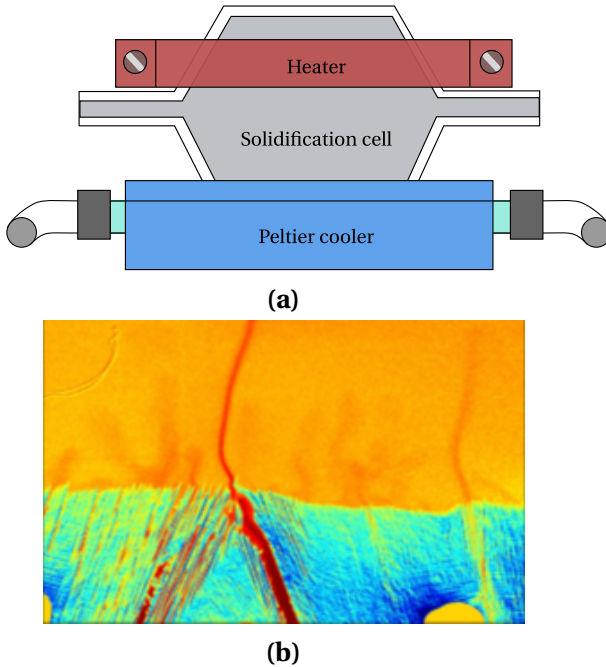


Fig. 4.5 – Illustration of the benchmark experiments for in-situ observation of segregated channels formation using X-Ray radiography with (a) a schematic of the cell and (b) a typical image of the microstructure formed during directional solidification of an In-75 wt.% Ga alloy. Reproduced from [Shevchenko et al. 2013].

22 mm × 22 mm, are adiabatic. In spite of taking cell dimensions similar to benchmark experiments presented above, the cell thickness is increased from 150 µm to 1 mm. This facilitates the computation and will later be subject to discussion.

Table 4.1 – Summary of the simulations and the corresponding parameters for the FE cases, where a purely macroscopic model is used. Parameters are varied from (G1) low to (G2) high gradient and (L0) no, to (L1) low lateral cooling.

Case	Vertical gradient G [K mm ⁻¹]	Cooling rate R [K s ⁻¹]	Lateral cooling L (h _{ext} , T _{ext}) [W m ⁻² K ⁻¹ , °C]	Initial temperature (T _{top} , T _{bottom}) [°C]
FE-G1R1L0	G1:0.2	R1:-0.01	L0:(0,0)	(29.75, 25.25)
FE-G1R1L1	G1:0.2	R1:-0.01	L1:(20,0)	(29.75, 25.25)
FE-G2R1L1	G2:1.5	R1:-0.01	L1:(20,0)	(58.25, 25.25)

Materials properties are provided in [table 4.2](#) while initial and boundary conditions are given in [table 4.1](#). A series of computations is performed to understand the influence of process parameters on the final macrosegregation pattern. In directional growth, the main parameters are the vertical temperature gradient, G, and the cooling rate, R, since they control the isotherms speed. However, the effect of a higher lateral cooling is also considered below by increasing the heat transfer coefficient, h_{ext}.

Finally, the grain structure is another crucial parameter that drastically changes the analysis inasmuch as growth undercooling is fundamental to determine the onset of solidification. The computation cases used in this study are presented in [table 4.1](#). The label of each case allows direct access to the simulation parameters as explained in the caption. Values for these parameters are inspired from the above experiments ([section 4.5.2](#)). Initial conditions consider a quiescent liquid at uniform composition given by the nominal alloy composition $\langle w_0 \rangle$. The temperature field is also initially uniform at a temperature averaged between the top and bottom initial values provided in [table 4.1](#). It has been checked that a uniform temperature gradient is swiftly reached, and that the unsteady regime to settle a vertical temperature gradient does not affect the phenomena studied. For simulations with grain structures, boundary conditions for nucleation at the bottom horizontal $22\text{ mm} \times 1\text{ mm}$ surface are kept constant as given in [table 4.1](#).

The macroscale approach employs the finite element method to compute the temperature and composition fields at FE nodes. The liquid fraction is then determined directly from the former fields, assuming a linear phase diagram, i.e. linear liquidus with full thermodynamic equilibrium between phases or lever rule approximation. This linear approximation is made available by the dotted line provided in [fig. 4.6](#). Note that this line defines a phase diagram that seems very different from the correct one. However, this linear fit is only used in a composition region located around the nominal composition of the alloy. It is also worth noticing that the eutectic microstructure is expected to appear at $15.3\text{ }^\circ\text{C}$. However, experimental observations revealed that large eutectic nucleation undercooling was reached, so the eutectic solidification was not reported in the experiments studied by [Shevchenko et al. \[2013\]](#). Consequently, the solidification path is computed without accounting for the eutectic microstructure in the present simulations, thus extending the liquidus and solidus lines below the eutectic temperature as sketched with the linear approximations in [fig. 4.6](#).

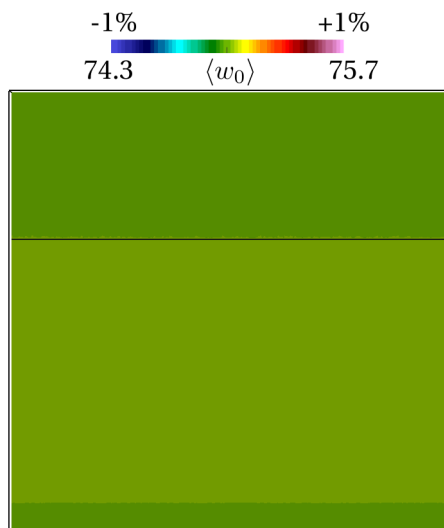
Results

The first case labeled FE-G1R1L0 is a reference case that features a low gradient (G1), low cooling rate (R1), and without any lateral cooling (L0), ensuring that isotherms retain a planar shape. These simulation parameters defined in [table 4.2](#), result in a negligible fluid flow reaching a maximum velocity of $4 \times 10^{-8}\text{ mm s}^{-1}$ in the bulk. Accordingly, the solidification front remains stable and follows the planar isotherms; no chimneys are observed. The average composition field is thus only little modified in the mushy zone as shown in [fig. 4.7](#) (mind the values of the scale limits). It is con-



Fig. 4.6 – Binary phase diagram of the In-Ga system [Andersson et al. 2002; TCBIN 2006] and its approximation for solidification studies with an In-75 wt.% Ga alloy. The dashed and dotted lines are linear liquidus and solidus approximations near the nominal composition.

cluded that velocity in the bulk is not high enough to initiate instabilities. In the next case, FE-G1R1L1, a cooling flux with a constant and very low value of the heat transfer coefficient is imposed on both vertical lateral surfaces to initiate a downward fluid flow by thermal buoyancy. Once solidification starts, solute-rich regions start to appear on the sides of the domain. Despite the visible concentration difference between these lateral regions and the central mush seen in [fig. 4.7](#), their diffuse and uniform aspect indicates no resemblance to segregated channels. We keep the same configuration but increase the vertical gradient from 0.2 K mm^{-1} (G1) to 1.5 K mm^{-1} (G2) in the case FE-G2R1L1. The isotherms become closer to each other hence reducing the depth of the mushy zone for the same time increment compared to the preceding case. The rejected gallium solute locally accumulates at several different positions in the mushy zone, stemming from the base of the cell, with a maximum of 0.7 wt.%Ga above nominal composition. This is the consequence of segregation of gallium rich liquid being lighter than the above liquid bulk and creating an upward buoyancy force. The positive segregation and subsequent Ga-rich chimneys then rise up with an upward velocity component slightly greater than 1 mm s^{-1} . [Figure 4.8](#) gives a series of snapshots for case FE-G2R1L1 at three different times. Among the two clear distinct plumes that are visible at 250 s in [fig. 4.7](#), only one has led to a channel formation, that remains in [fig. 4.8](#) at 500 s. In fact, an animation between 250 s and 500 s (not shown here) reveals that one plume vanishes, thus permitting the first one to further develop. A second freckle is also seen on the left hand side of the cell. These two freckles are stable for a long time since they remain at time 1000 s. However, the left side freckle develops



(a) FE-G1R1L0



(b) FE-G1R1L1



(c) FE-G2R1L1

Fig. 4.7 – Average Ga composition field at 250 s for the 3 FE cases showing the influence of process parameters on the freckling tendency. The black line represents the liquidus isotherm given in [table 4.2](#).

4.5. Macroscopic prediction of channel segregates

Table 4.2 – Material parameters for In-75 wt.% Ga and numerical parameters.

Parameter	Symbol	Value	Unit
Nominal composition	$\langle w_0 \rangle$	75	wt.%
Liquidus temperature	T_l	25.25	°C
Segregation coefficient	k	0.0165	wt.% wt.% ⁻¹
Liquidus slope	m_l	-2.73	K wt.% ⁻¹
Gibbs-Thomson coefficient	Γ_{GT}	2×10^{-7}	K m ⁻¹
Heat capacity (liquid and solid)	C_p	380.74	J kg ⁻¹ K ⁻¹
Enthalpy of fusion	L	8.02×10^{-4}	J kg ⁻¹
Diffusion coefficient of Ga in liquid In	D^l	1.525×10^{-9}	m ² s ⁻¹
Dynamic viscosity	μ^l	2×10^{-3}	Pas
Thermal expansion coefficient	β_T	0.0978×10^{-3}	K ⁻¹
Solutal expansion coefficient	$\beta_{\langle w \rangle^l}$	1.44×10^{-3}	wt.% ⁻¹
Thermal conductivity in the solid	$\langle \kappa \rangle^s$	40	W m ⁻¹ K ⁻¹
Thermal conductivity in the liquid	$\langle \kappa \rangle^l$	28	W m ⁻¹ K ⁻¹
Dendrite arm spacing	λ	60×10^{-6}	m
Density	ρ_0^l	6725	kg m ⁻³
Reference composition	w_0^l	75	wt.%
Reference temperature	T_0	25.25	°C
CA cell size		30×10^{-6}	m
FE mesh size		140×10^{-6}	m
Time step	Δt	0.1	s

further to become the main one at 1500 s, while the mid-width freckle decreases in intensity, changes orientation and subsequently disappears (not shown here). Thus, the birth and death of very few freckles is observed in this simulation, mainly due to solutal instability, as the temperature field shown in fig. 4.8 clearly remains stable despite the low lateral heat flux. As shown in fig. 4.7, instability is yet required to create these chemical plumes and channels. Here, it is created by a very small lateral heat flow but other sources of instability could be involved, as shown with the grain structure in the next section.



Fig. 4.8 – Simulation results for case FE-G2R1L1 showing maps of the average composition in gallium, the solid fraction, the superficial velocity field (vertical component) and the temperature, on a cut plane at the center of the cell at 500 s, 1000 s and 1500 s.

Discussion

In section 4.5.1, we have introduced some successful attempts of freckle predictions. The authors tackled the problem from an qualitative perspective. To our knowledge, the closest work to quantitative freckling analysis in solidification literature was done by Ramirez et al. [2003]. They attempted to draw a correlation (freckling criterion) between the process parameters and the occurrence of freckles, (without any size or shape constraints, i.e. any flow instability that may appear and form the smallest freckle is considered). To accomplish this, they took a number of experiments done independently by Pollock et al. [1996] and Auburtin et al. [2000] where the casting parameters vary one at a time: casting speed (R), thermal gradient (G), angle (θ) with respect to vertical orientation and nominal composition ($\langle w_0 \rangle$), giving a database for 6 different superalloys. The experimental results were compared to a modified Rayleigh number that accounts for the various parameters. It allowed them to define a threshold for freckle formation in Nickel-base superalloys, as well as Pb-Sn alloys. Other contributions by Yuan et al. [2012] (Pb-Sn alloy) and Karagadde et al. [2014] (In-Ga alloy) relied on a Cellular Automata Finite Difference (CAFD) model developed by Lee et al. [2002], which solves the dendrite tip growth kinetics at the solid-liquid interface together with macroscopic conservation equations. The authors compared the simulated formation of freckles with the results obtained by Shevchenko et al. [2013]. However, these simulations follow solidification in a small volume that contains a few dendrites with interdendritic liquid, therefore limited as far as to predict the liquid behaviour outside the mushy zone. On another hand, experimental observations reveal a great deal of information regarding solute redistribution, first in the chimneys that wash the dendrites in their way and then convective plumes that expel chemical species outside the mush, resulting in a global complex phenomenon. In order to capture simultaneously the interaction between the mushy zone and the free liquid, we use the Cellular Automata Finite Element (CAFE) method to combine the macroscopic and mesoscopic length scales and predict more realistic channel segregation.

4.6 Meso-Macro prediction of channel segregates

4.6.1 Numerical method

Microscopic scale

The CAFE model introduces a grid of regular and structured cubic cells, with a constant size in all space directions, referred to as the cellular automaton (CA) grid. It is different

from the unstructured finite element mesh previously mentioned for the solution of the average conservation equations. A typical CA step dimension is smaller than the smallest FE mesh size. The CA grid serves to represent solidification phenomena including nucleation, growth and remelting of the envelope of the primary dendritic grains. Details about the CAFE model can be found in [Carozzani et al. 2012; Carozzani et al. 2013; Carozzani et al. 2014]. Cell information, such as the temperature, the average composition or the velocity of the liquid phase, is interpolated from the nodes of the FE mesh. State indices are also defined for each CA cell, providing the presence of liquid or solid phases.

Nucleation

Initially, cells are in a fully liquid state. In the present situation, random nucleation sites are chosen based on a nucleation density, n_{\max} (expressed in surface density inverse m⁻²), at the bottom surface of the geometry in contact with the cooler. Nucleation occurs in a cell only if the latter contains a nucleation site, and when the local undercooling of the cell reaches the critical nucleation undercooling given as input by a Gaussian distribution of mean undercooling ΔT_N with a standard deviation ΔT_σ . The crystallographic orientation of each grain newly nucleated is also randomly chosen using values of the Euler angles to fully define the three rotations that transform the reference frame to the $\langle 100 \rangle$ directions that define the main growth axes of the dendrite trunks and arms. Grain selection is therefore solely controlled by growth competition.

Growth

Dendrite growth is driven by the chemical supersaturation $\Omega_{\text{saturation}}$, which is a dimensionless number proportional to the difference between the liquid composition at the dendrite tip and the melt composition far away from the tip. The higher the supersaturation, the faster the dendrite tip velocity. However, in the presence of a convective fluid, the chemical supersaturation is highly influenced by the intensity and the direction of the flow with respect to the growth direction of the dendrites. In the current model, convection is central in studying freckle formation. Therefore, the purely diffusive Ivantsov relation used to determine the Peclet number Pe as function of the supersaturation, is replaced by a modified relation using a boundary layer correlation model that accounts for both the intensity and the misorientation of the liquid velocity with respect to the growth direction of the dendrites [Gandin et al. 2003]. The main parameters for this growth kinetics models are the Gibbs Thomson coefficient,

4.6. Meso-Macro prediction of channel segregates

Table 4.3 – Summary of the simulations and the corresponding parameters for the CAFE cases, coupling macroscopic model with the grain structure model. Parameters are varied from (G1) low to (G2) high gradient, (R1) low to (R2) high cooling rate and (L0) no, (L1) low and (L2) high lateral cooling.

Case	Vertical gradient G [K mm ⁻¹]	Cooling rate R [K s ⁻¹]	Lateral cooling L (h _{ext} , T _{ext}) [W m ⁻² K ⁻¹ , °C]	Initial temperature (T _{top} , T _{bottom}) [°C]	Nucleation (n _{max} , ΔT _N , ΔT _σ) [m ⁻² , °C, °C]
CAFE-G2R1L1	G2:1.5	R1:-0.01	L1:(20,0)	(58.25, 25.25)	(10 ⁶ , 1, 0.2)
CAFE-G1R1L1	G1:0.2	R1:-0.01	L1:(20,0)	(29.75, 25.25)	(10 ⁶ , 1, 0.2)
CAFE-G1R1L2	G1:0.2	R1:-0.01	L2:(500,0)	(29.75, 25.25)	(10 ⁶ , 1, 0.2)
CAFE-G2R2L1	G1:0.2	R2:-0.05	L1:(20,0)	(29.75, 25.25)	(10 ⁶ , 1, 0.2)

Γ_{GT} , and the diffusion coefficient for Ga in In, D^l .

Solidification path

The CA model gives the presence of the grains in the liquid as well as its growth undercooling. For coupling with macroscopic scale modelling, the fraction of phases needs to be fed back to the FE model. This is now done by accounting for the information provided by the CA model. Thus, the fraction of solid is no longer the consequence of a simple conversion of the temperature and composition assuming thermodynamic equilibrium. It also includes the solidification delay due to the kinetics of the development of the grains as detailed elsewhere in the work of [Carozzani et al. \[2013\]](#).

Numerical method

Both the finite element mesh and the cellular automaton grid play a role in predicting freckles inasmuch as this type of defect originate from interplays between hydrodynamic instabilities on the scale of the dendrites and macroscopic flows defined by the geometry of the experimental cell [[Shevchenko et al. 2013](#)]. One has to respect a small maximum FE mesh size, comparable to the dendrite arm spacing. With such an element size, composition gradients giving rise to solutal buoyancy forces can be captured. This limits consequently the CA cell size, as a minimum number of cells is required in each finite element. In the array of simulations that will be presented in the next section, the value of λ_2 was considered. We have chosen a fixed mesh element size of $2\lambda_2$ and a CA cell size of $\lambda_2/2$. An average of 4 CA cells per unit length of a finite element is enough to accurately compute the development of the grain envelopes together with the solutal, thermal and mechanical interactions.

4.6.2 Configuration

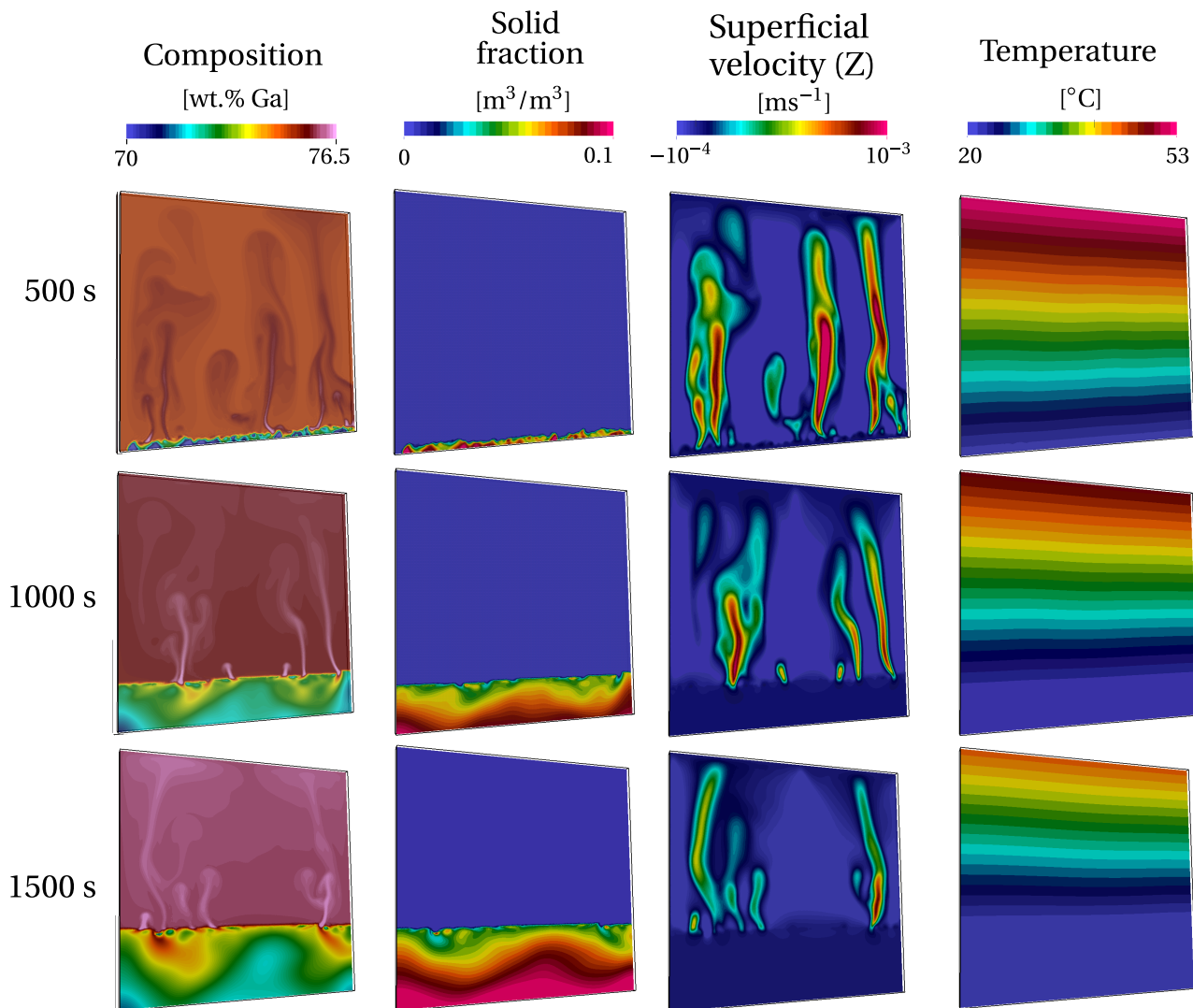


Fig. 4.9 – Simulation results for case CAFE-G2R1L1 showing maps of the average composition in gallium, the solid fraction, the superficial velocity field (vertical component) and the temperature, on a cut plane at the center of the cell at 500 s, 1000 s and 1500 s.



Fig. 4.10 – Simulation results the predicted of mushy grain structure with the corresponding composition maps.

Knowing that the configuration in FE-G2R1L1 produces segregated channels, the same set of parameters is first used for case CAFE-G2R1L1 by adding the effect of the grain structure using the CAFE model. Results are accessible in [fig. 4.9](#) for comparison with [fig. 4.8](#). A striking difference is seen: the composition maps become more perturbed as shown by the formation of numerous plumes when coupling with grain structure is active. The growing front displayed on the grain structure at the right most column of [fig. 4.9](#) dictates the leading position of the mushy zone shown in the third column. Note that each color corresponds to one grain, with 17 grains having nucleated at the cell's bottom surface. However, comparison of the solid fraction maps between [fig. 4.8](#) and [fig. 4.9](#) at the same times reveals a delay in the growing front position.

Values of the nucleation parameters in [table 4.3](#) are such that few grains rapidly form

below the nominal liquidus isotherm. The delay is therefore not due to the nucleation undercooling but to the growth undercooling of the dendrite tips. It should be noticed that, the growth front driven by undercooling in [fig. 4.9](#) also forms with a higher initial solid fraction and hence larger solute segregation occurs at the front. This effect, together with instabilities of the composition field, is caused by a more perturbed fluid flow and more plumes as observed in CAFE-G2R1L1 compared to FE-G2R1L1. Such observations fit to the complicated fluid and solute flow patterns typically occurring in the experiments as shown in [fig. 4.11](#).

It becomes obvious that the consideration of grain structure and growth undercooling are vital to accurately simulate segregated channels formation in these experiments. The reasons for the instabilities are discussed hereinafter.

In the present 3D CAFE simulation, each grain shown in [fig. 4.10](#) is associated with a crystallographic orientation. The growth kinetics is only given for the $\langle 100 \rangle$ crystallographic directions at the grain boundaries with the liquid. The CA growth model is based on the hypothesis that, in a quiescent liquid of uniform temperature distribution and composition, the grain envelop should reproduce an octahedral grain shape with main directions given by the six $\langle 100 \rangle$ directions. In the present situation where complicated fields are present for temperature, composition and liquid velocity, each grain envelope with different crystallographic orientation adapts differently to its local environment. Thus, the local undercooling of the front varies everywhere. Such variations are within few degrees here, but this is sufficient to create irregularities on the growth front, as seen on the grain structure in [fig. 4.10](#). Apart from that, these variations are linked to the position of the instabilities for the chemical and liquid velocity fields, thus demonstrating the full coupling between the CA and FE models.

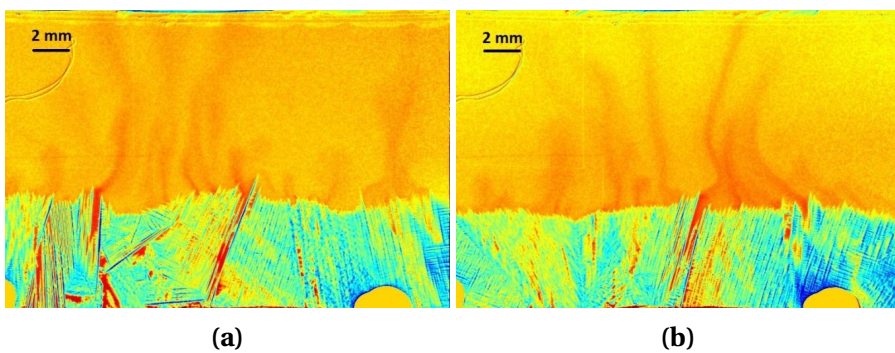


Fig. 4.11 – Snapshots of dendritic structure and composition field obtained from two solidification experiments at a cooling rate $R=-0.01 \text{ K s}^{-1}$ and temperature gradients of (a) $G=1.1 \text{ K mm}^{-1}$ and (b) $G=1.3 \text{ K mm}^{-1}$

4.6.3 Effect of vertical temperature gradient

The influence of diverse process parameters can now be considered in context of the grain structure. The effect of the vertical temperature gradient is shown by comparing the previous case CAFE-G2R1L1 with case CAFE-G1R1L1. The temperature gradient is decreased about 7 times here, from $G_2=1.5 \text{ K mm}^{-1}$ to $G_1=0.2 \text{ K mm}^{-1}$. In fact, both cases share almost all traits with respect to flow patterns and velocity magnitude in the bulk. Main differences are yet seen regarding the dynamics of the plumes shown in [fig. 4.12](#).

In the case of a low temperature gradient (G_1), the solidification front cannot maintain a shape as smooth as for the case of a large temperature gradient (G_2): the solute gradient in the liquid of the mushy zone (basically following the lever rule approximation for a given temperature) decreases, leading to a lower gradient of the solutal buoyancy force. In turn, more solute accumulates close to the front and locally reduces the growth velocity, thus creating larger “valleys” or steps with higher solute content. The irregular geometry of the front is also influenced by the dendrite tip growth kinetics model. The velocity of the isotherms is the ratio of the cooling rate, R , to the temperature gradient, G . Consequently, the isotherm velocity in case G_1 is larger than in G_2 , since cooling rate, R_1 , is the same in both cases. Moreover, because the dendrite tip velocity is a monotonously increasing function with the undercooling [[Gandin et al. 2003](#)], the latter for CAFE-G1R1L1 is larger than for CAFE-G2R1L1. Height differences of the growth front are proportional to the variations of the undercooling by the temperature gradient. Therefore, this forms larger steps on the growth front for case G_1 compared to G_2 .

The chimney extends deeper in the mushy zone when the temperature gradient increases. This is confirmed by both the simulation results shown in [fig. 4.12](#) as well as the experimental observations. Another remarkable phenomenon is also observed in the low gradient case: a “pulsing” mechanism in CAFE-G1R1L1 where a series of solute rich liquid pockets are observed one above the other. This corresponds to a repeated and localized strong spatial variation of the liquid velocity field outside the mushy zone, regularly thrusting away small plumes. These pulses are roughly similar to each other in size and exit speed, creating thus a very regular pattern during some time. In the case of a high temperature gradient (case CAFE-G2R1L1) this phenomenon is barely seen. In fact, the pattern shown in [fig. 4.12](#) is more typical, with continuous plume rising from the mushy zone and reaching the top of the domain. However, such regular plume is the initial and final pattern seen for low gradient before the pulsing regime. Similar observations have been made in the experiments too. [Figure 4.14a](#) displays the phenomenon of the “pulsing” plumes, which could be explained by the

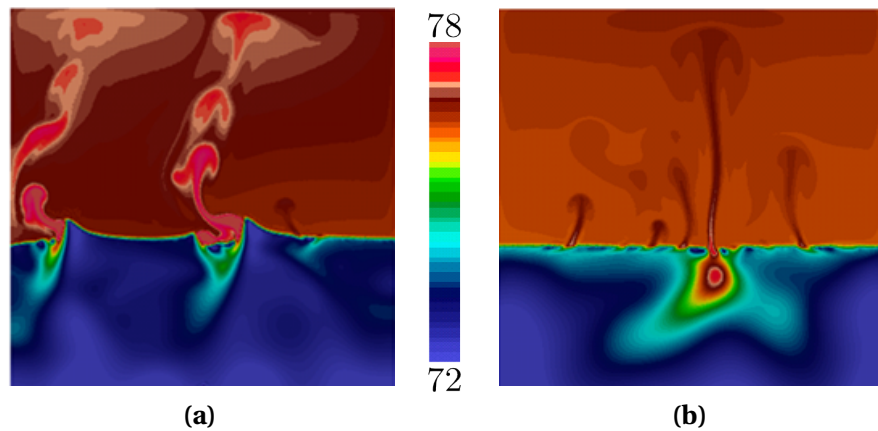


Fig. 4.12 – Average composition maps for CAFE-G1R1L1 at time 1060 s and CAFE-G2R1L1 at time 1845 s.



Fig. 4.13 – Snapshot of the pulsing mechanism coming from a groove shape in the mushy (check animation in the PDF file).

following mechanisms. The permeability of the mushy zone and the narrow gap of the solidification cell obstruct the feeding of the plumes by solute. A critical solute concentration has to be accumulated at a specific location in order to trigger the formation of a rising plume. An interim drop of the solute concentration below such a threshold would interrupt the plume. Flow instabilities can be another reason for the peculiar shape of the plumes. [Figure 4.14b](#) shows a pronounced continuous plume. The same plume can be seen a few seconds later in [fig. 4.14c](#). The plume structure becomes unstable; one can observe an indentation of streamlines followed by a mixing of rising solute-rich liquid with descending In-rich fluid. This mechanism also causes a non-continuous structure of the plumes.

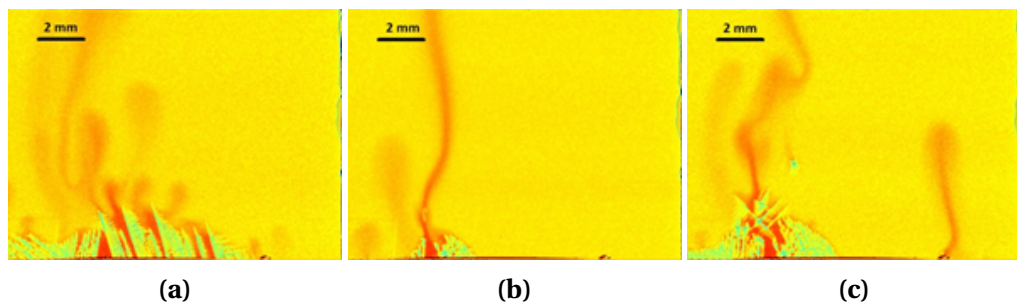


Fig. 4.14 – Snapshots of dendrite structure and composition field from two solidification experiments conducted at a cooling rate $R=-0.01 \text{ K s}^{-1}$ and a temperature gradient $=1 \text{ K mm}^{-1}$: (a) “pulsing” plumes, (b) continuous plume, (c) upcoming plume instability.

4.6.4 Effect of cooling rate

The next parameter studied is the cooling rate, corresponding to case CAFE-G1R2L1. A snapshot of the composition map and the corresponding vertical component of the velocity field are given in [fig. 4.15](#). We see a similarity with case CAFE-G1R1L1 in [fig. 4.12a](#) with respect to the buckled interface between the liquid and the mushy zone as well a plume pulsing effect when a low temperature gradient is applied. On the other hand, segregation inside the mush is more irregular with more pronounced patterns reaching a larger depth. One could distinguish alternating V and A shapes patterns in the mushy zone. As for case CAFE-G1R1L1, these patterns are created by a network of pulsing plumes formed by the steps created on the delocalized growth front due to the low temperature gradient. However, these considerations are not sufficient to explain the shape of the growth front. The reason for the protuberances created at the tips of the V shape is the presence of a descending bulk liquid with a low composition seen by the growth front. It infers that favorable growth conditions are created for a higher working temperature since the dendrite tip undercooling de-

creases for facing liquid flow and a lower composition; the growth rate is given by the isotherm velocity. The growth front thus adjusts its position to catch up with the corresponding isotherm, the latter being located at the tips of the V shape, i.e. the outmost advanced position of the growth front. It also means that the V shape angle depends on the size and intensity of the convection loops above the front. When the steps are formed on the growth front, the plumes exiting the mushy zone follow a direction normal to the front. They are inclined towards each other above the V shape. As a result, they may join and form a larger plume as seen in CAFE-G1R1L1 ([fig. 4.12a](#)), thus forming larger and more stable segregated channels. The other observation in [fig. 4.15](#) is the existence of stable regions of the growth front. For instance, this is seen in between the two V shape forming or on the right hand side of the cell. The reason

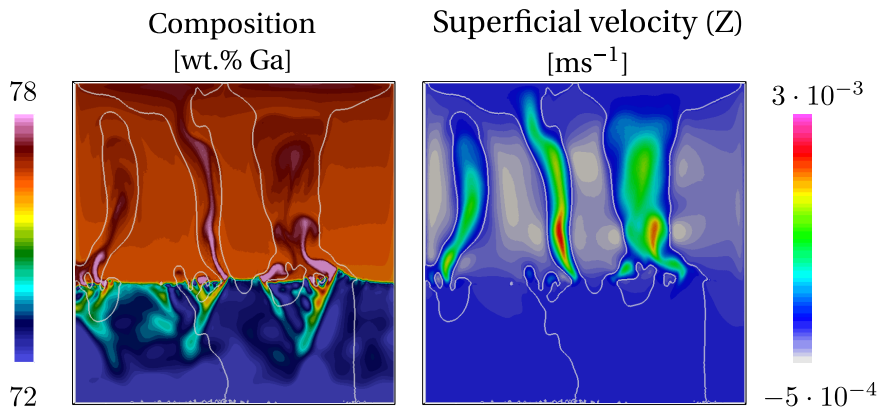


Fig. 4.15 – Average fields inside the cell for case CAFE-G1R2L1 at 350 s. The white contour identifies the zero velocity limit for the vertical component of the velocity field

for this stability is the inversion of the composition gradient located ahead. Animation shows that solute coming from the top of the cell is responsible for this accumulation, creating a layering that provides a stabilization effect above the mushy zone. This is verified by the vertical component of the average velocity also made available in [fig. 4.15](#). It is negative outside the path of the plumes. A resulting concurrent effect is the formation of the A shape segregates in between the V shape patterns seen in [fig. 4.15](#). Finally, it can be observed that these patterns are sustained longer compared to [fig. 4.12](#) CAFE-G1R1L1 because, at high cooling rate, the flow in the mushy zone is decreased due to a faster solidification. This is the same effect as described for the large gradient configuration in CAFE-G2R1L1 ([fig. 4.12b](#)). It is not clear how these observations could be compared with the A and V shapes segregates reported for steel ingots [[Pickering 2013](#)]. Despite the fact that macrosegregation is the main phenomenon leading to these patterns, there has not been a clear explanation yet in the literature for their formation. However, for steel casting, the A and V patterns

are believed to form concomitantly. Further investigations would thus be required to quantify the consequences of thermosolutal instabilities simulated here for an In-75 wt.% Ga alloy and check their possible correlation with experimental observations in steel casting.

4.6.5 Effect of lateral temperature gradient

The previous simulations show the effect of cooling rate and temperature gradient on the survival of segregation patterns deep in the mushy zone. Another simulation is performed by increasing the cooling rate using higher heat flux extracted from the vertical side boundaries. This is achieved in case CAFE-G1R1L2 where the heat transfer coefficient reaches $500 \text{ W m}^{-2} \text{ K}^{-1}$. As a consequence of the large cooling from the sides, the temperature gradient is no longer vertical. A distinct flow due to thermal buoyancy is created, driving a cold liquid downwards near the sides of the cell. Under the influence of these 2 main convection loops, all segregation plumes tend to regroup in the middle of the domain, forming a larger central plume, as seen in the composition map at 450 s in [fig. 4.16](#). However, this regime occurs at times earlier than 500 s, where the effect of thermally induced buoyancy forces is prevailing, feeding the convection loops. Approximately 500 s later, the mushy zone has extended, favouring the segregation mechanical forces i.e. $\rho_{\text{ref}} (1 - \beta_{\langle w \rangle^l} \Delta \langle w \rangle^l) \vec{g}$, rather than the thermal mechanical forces, $\rho_{\text{ref}} (1 - \beta_T \Delta T) \vec{g}$. [Figure 4.16](#) shows the correspond-

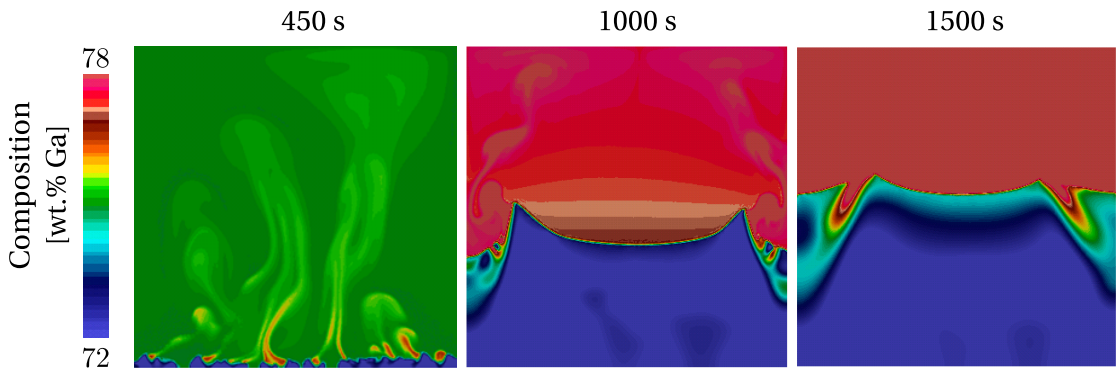


Fig. 4.16 – 2D cut plane of the average composition inside the cell for case CAFE-G1R1L2 at the following time increments: 450 s, 1000 s and 1500 s.

ing composition maps with stable chimneys at about 1000 s that also remain at 1500 s. The solidification front then tends to form a concave shape at the center of the cell, thus partially revealing the form of the isotherms toward the cell center. The stable pattern in the center is similar to the plateau seen at the center, between the A-shapes in [fig. 4.12](#) and [fig. 4.15](#). As stated before, it is an inactive region with respect

to plume initiation due to the inversion of the solute composition gradient. In other words, the high gallium concentration at the top of cell causes indium, which is the heavier species, to accumulate and be partially trapped between the mushy walls, thus creating a stable flow configuration. Outside of the plateau, 2 plumes are observed from the prominent instabilities of the growth front, adopting diverging directions. This is also observed at the center of the cell in [fig. 4.15](#) on each side of the A-shape segregate. These plumes in [fig. 4.16](#) lead to the formation of two stable channels. The corresponding situation in the experiment is shown in [fig. 4.17](#). The chimneys on both sides and the plateau in between can be clearly recognised. The additional cooling at the side walls produces two flow vortices between the side wall and the strong convective plumes above the chimneys. The central part of the sample remains almost unaffected by the additionally driven thermal convection. This area is characterised by the occurrence of a number of smaller convective plumes.

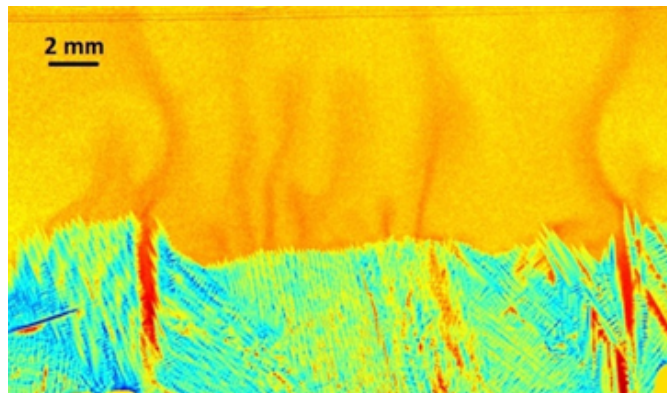


Fig. 4.17 – Snapshot of dendritic structure and composition field from a solidification experiment recorded at 1000 s for a cooling rate $R=-0.01 \text{ Ks}^{-1}$ and a temperature gradient $G=-1 \text{ Kmm}^{-1}$.

4.6.6 Mono-grain freckles

All CAFE simulations were performed considering a normal classic heterogeneous nucleation at the surface of the mould where the metal is cooled down. However, as the number of grains is not negligible, the subsequent fluid-structure interaction between dendrites, simply represented by an isotropic permeability and the interdendritic flow cannot be easily interpreted. Therefore, one may consider simpler solidification cases like a mono-grain growth. This ideal situation is not always experimentally viable: either the mould surface is not perfectly smooth, and therefore nucleation can be triggered by a wetting mechanism, or the metal contains a certain level of impurity which can trigger nucleation heterogeneously in the liquid bulk. Regardless of this

4.6. Meso-Macro prediction of channel segregates

experimental limitation, this type of simulations allows simpler understanding as the grain growth is not disturbed by another neighbouring grain, it grows while exclusively interacting with the liquid phase.



Fig. 4.18 – Snapshots of mono-grain solidification showing the average composition in gallium predicted by the CAFE approach. Two orientation scenarios are considered where a) the grain is upright with a Euler angle of $(90^\circ, 0^\circ, 0^\circ)$ or b) the grain is tilted with a Euler angle of $(90^\circ, 30^\circ, 0^\circ)$ (check animation in the PDF file).

Chapter 5

Macrosegregation with solidification shrinkage

Contents

5.1	Solidification shrinkage	107
5.2	Choice of interface tracking	107
5.3	Multidomain formalism	109
5.3.1	Assumptions	110
5.4	FE partitioned model	111
5.4.1	In the metal	112
5.4.2	In the air	115
5.5	FE monolithic model	118
5.5.1	Monolithic equations	118
5.5.2	Darcy term in the air	121
5.5.3	Interface motion and stability	121
5.6	1D application: solidification with inverse segregation	125
5.6.1	Geometry and boundary conditions	125
5.6.2	Shrinkage without macrosegregation	126
5.6.3	Shrinkage with macrosegregation	135
5.7	2D application: controlled solidification benchmark	143
5.7.1	Absence of convection	144
5.8	3D application: reduced-gravity solidification	144
5.8.1	Previous work	144
5.8.2	Computational configuration	147
5.8.3	Texus binary alloy	152

Chapter 5. Macrosegregation with solidification shrinkage

5.8.4	Texus ternary alloy	152
5.8.5	Texus quaternary alloy	152
5.8.6	TODO	152

5.1 Solidification shrinkage

Solidification shrinkage is, by definition, the effect of relative density change between the liquid and solid phases. In general, it results in a progressive volume change during solidification, until the phase change has finished. The four stages in [figs. 5.1a](#) to [5.1d](#) depict the volume change with respect to solidification time. First, at the level of the first solid crust, near the local solidus temperature, the solid forms with a density greater than the liquid's. The subsequent volume decrease creates voids with a negative pressure, forcing the fluid to be sucked in the direction of the volume change (cf. [fig. 5.1b](#)). As a direct result of the inward feeding flow, the ingot surface tends to gradually deform in the feeding direction, forming the so-called *shrinkage pipe*, shown in [fig. 5.2](#). Since the mass of the alloy and its chemical species is conserved, a density difference between the phases ($\rho^l < \rho^s \implies \frac{\rho^l}{\rho^s} < 1$) eventually leads to a different overall volume ($V^s < V^l$) once solidification is complete, as confirm the following equations:

$$\rho^l V^l = \rho^s V^s \quad (5.1a)$$

$$V^s = \frac{\rho^l}{\rho^s} V^l \quad (5.1b)$$

Solidification shrinkage is not the only factor responsible for volume decrease. Thermal shrinkage in both solid and liquid phases, as well as solutal shrinkage in the liquid phase are also common causes in a casting process. However, thermal shrinkage is very important to apprehend, as temperature decreases in steel casting, usually exceeding a 1000 °C, thus causing substantial density variations.

5.2 Choice of interface tracking

In chapter 2, several methods of interface tracking/capturing methods were presented along with their similarities and differences. In the case of solidification shrinkage, the metal-air interface can be tracked with any method from the previously mentioned. However, several reasons motivate us to settle on the level set method. First, the easiest solution is testing a method which already exists in *CimLib* library. The level set method was implemented by HERE as a framework for monolithic resolution. Since this work, the method has been extensively used and improved in several projects mainly for multiphase flows, which is the main competence of the Computing and FLuids (C.FL) group at CEMEF. Another motivation is the compatibility between *CimLib* and *TherCast*®, where the latter is the final destination of the code developed

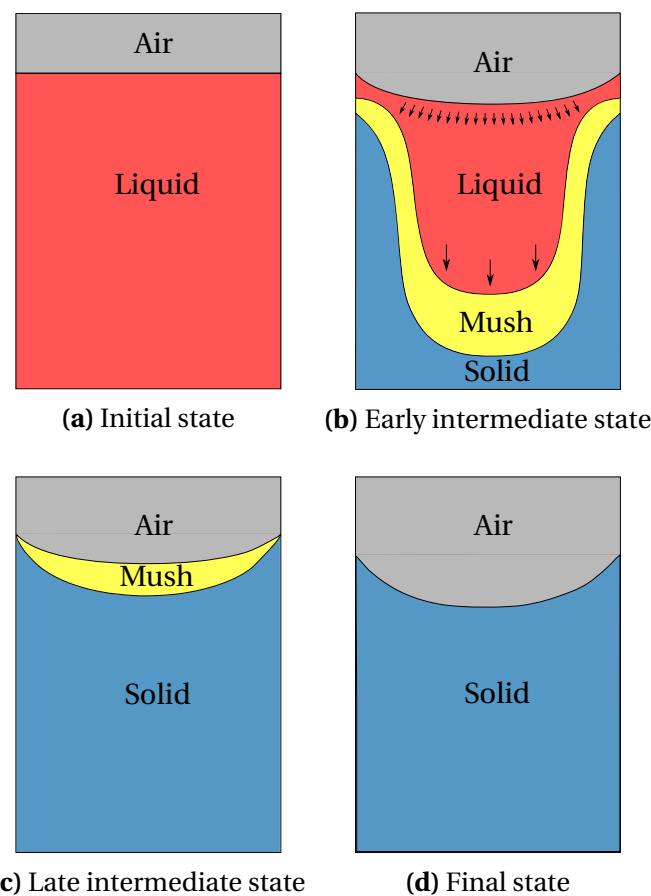


Fig. 5.1 – Schematic of the main cooling stages of an ingot against side and bottom mould walls (not shown)

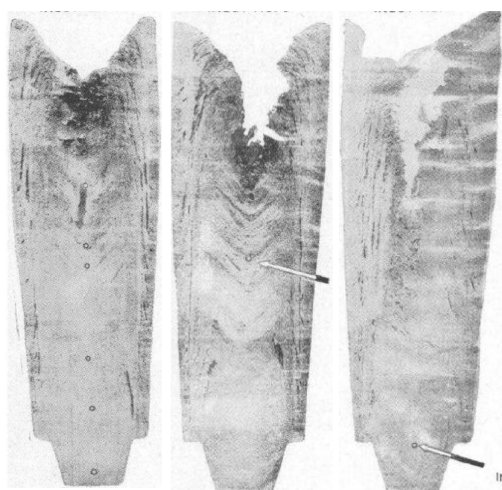


Fig. 5.2 – Sulphur prints of three ingots showing pipe formation at the top as a result of solidification shrinkage with various ingot inclination during casting [Onodera et al. 1959]. Positive macrosegregation is clearly seen in this area, while A-shape and V-shape positive mesosegregates are detected at the ingot's tips and center respectively.

during for the Ph.D. thesis. In its recent versions, *Thercast*[®] handles laminar and turbulent ingot filling where the level set method is used to capture the free surface of the molten metal. Aside from the practical motivations, some technical aspects of the level set method make it very attractive to apply it macroscopic surface tracking (in contrast to microscopic interface tracking, for instance the solid-liquid interface), such as topological properties that are readily available (e.g. curvature) and accurate position compared to volume-based methods like VOF.

5.3 Multidomain formalism

In the previous chapters, we considered in our simulations the metal as a saturated mixture of solid and liquid during solidification. It means that no gas phase may appear during the process, and this this chapter. The reason is we chose to describe our model in Eulerian description, for which we have considered a fixed grid to discretise the averaged conservation equations governing the phase change between the liquid and solid phases. Furthermore, with the introduction of shrinkage, an increase in global density means that a gas phase should enter the domain to replace the shrunk volume. At this point, several interfaces may be distinguished: liquid-solid ($l-s$), liquid-air ($l-a$) and solid-air ($s-a$), where we defined 2 phases (l and s) belonging to the "Metal" domain denoted M , while the "Air" domain, denoted A , is made up of a unique phase, (a), with the same name. As a standard for this formalism, we consider that uppercase letters are used for domains, while lowercase letters are used for phases.

The main idea behind the multidomain formalism, is to go from the classic conservations equations introduced by volume averaging in chapter 2, in the context of a solidifying two-phase system to generalise it by taking into account a third gas phase, such as:

$$V^l + V^s + V^a = V_E \quad (5.2)$$

$$g^l + g^s + g^a = 1 \quad (5.3)$$

while keeping a physical integrity with the former monodomain model. Then, one is free to choose a suitable numerical method to track the interfaces between the several phases. In our applications, we are particularly interested in keeping an indirect representation of the $l-s$ interface (dotted line in [fig. 5.3](#)) using the volume averaging theory, while employing a different method to track the $l-a$ and $s-a$ interfaces (dashed lines in [fig. 5.3](#)) with the level set method. This allows switching to the latter method

in a physically representative manner.

In this context, each domain can be seen as a material having a physical interface with the other domains. As a consequence of our interpretation, the gas phase should not exist in the metal, which may naturally occur if the thermodynamic conditions are in favour of nucleating and growing a new phase, or in the case of a gas that was trapped inside mould grooves.

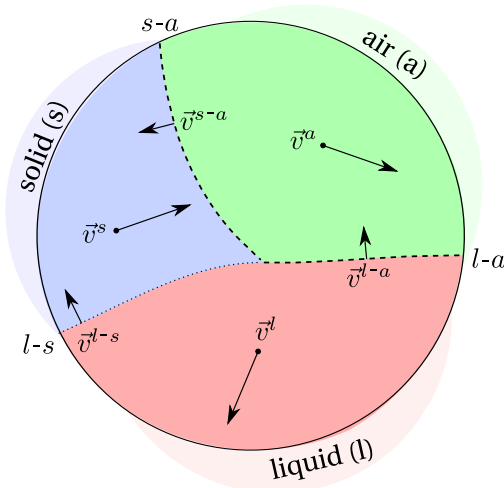


Fig. 5.3 – Schematic of a representative volume element containing 3 phases with distinct velocities, separated by 3 interfaces. The dotted line is the indirectly tracked solid-liquid interface while the other dashed lines, air-liquid and air-solid interfaces, are directly tracked.

5.3.1 Assumptions

Each phase in the system has its own velocity, \vec{v}^l , \vec{v}^s and \vec{v}^a , while the respective interfaces $l-s$, $l-a$ and $s-a$ have different and independent velocities, represented by \vec{v}^{l-s} , \vec{v}^{l-a} and \vec{v}^{s-a} . Note that the solid-liquid interface velocity was denoted \vec{v}^* in the previous chapters as no more than two phases were considered. The first major assumption is that the solid phase, once formed from the liquid, is fixed and rigid. It means that no subsequent deformation may occur and therefore \vec{v}^{s-a} reduces to vector zero. Moreover, we use the already introduced volume averaging principles to write locally for any quantity ψ :

$$\langle \psi \rangle = \left\langle \psi^l \right\rangle + \langle \psi^s \rangle + \langle \psi^a \rangle \quad (5.4a)$$

$$= g^l \psi^l + g^s \psi^s + g^a \psi^a \quad (5.4b)$$

where volume fractions, g^ϕ , for each phase ϕ were used. Rappaz et al. [2003] define the volume fraction by writing a general expression inside the representative volume V_E :

$$g^\phi = \frac{1}{V_E} \int_{V_E} \chi^\phi(x, t) d\Omega = \langle \chi^\phi \rangle \quad (5.5)$$

where the integrated quantity is an indicator (or presence) function relative to phase ϕ , which defines the volume of this phase in the system, Ω^ϕ , as follows:

$$\chi^\phi(x, t) = \begin{cases} 1 & \text{if } x \in \Omega^\phi \\ 0 & \text{otherwise} \end{cases} \quad (5.6)$$

Any phenomenon that may displace an interface, whether by phase change or a phase motion, is mathematically translated by variations of the presence function, such that its total derivative for each phase satisfies the following:

$$\frac{d\chi^\phi}{dt} = \frac{\partial \chi^\phi}{\partial t} + \vec{v}^* \cdot \vec{\nabla} \chi^\phi = 0 \quad (5.7)$$

If we consider the liquid phase, the variations of any quantity, named ψ , are given by:

$$\left\langle \frac{\partial \psi^l}{\partial t} \right\rangle = \frac{\partial \langle \psi^l \rangle}{\partial t} - \frac{1}{V_E} \int_{l-a} \psi^l \vec{v}^{l-a} \cdot \vec{n}^{l-a} d\Gamma - \frac{1}{V_E} \int_{l-s} \psi^l \vec{v}^{l-s} \cdot \vec{n}^{l-s} d\Gamma \quad (5.8)$$

$$\left\langle \vec{\nabla} \psi^l \right\rangle = \vec{\nabla} \langle \psi^l \rangle + \frac{1}{V_E} \int_{l-a} \psi^l \vec{n}^{l-a} d\Gamma + \frac{1}{V_E} \int_{l-s} \psi^l \vec{n}^{l-s} d\Gamma \quad (5.9)$$

$$\left\langle \vec{\nabla} \cdot \vec{\psi}^l \right\rangle = \vec{\nabla} \cdot \langle \vec{\psi}^l \rangle + \frac{1}{V_E} \int_{l-a} \vec{\psi}^l \cdot \vec{n}^{l-a} d\Gamma + \frac{1}{V_E} \int_{l-s} \vec{\psi}^l \cdot \vec{n}^{l-s} d\Gamma \quad (5.10)$$

[Equation \(5.7\)](#) can be recast with the level set method by using the smoothed Heaviside function in the metal. For the metal, this function is equal to one and decreases to zero in the air in a smooth way across both interfaces, solid-air and liquid-air. Since the solid phase is assumed fixed without possible deformation, and knowing that air is assumed incompressible, the solid-air interface does not move, leading to the following equation:

$$\frac{dH^M}{dt} = \frac{\partial H^M}{\partial t} + \vec{v}^{l-a} \cdot \vec{\nabla} H^M = 0 \quad (5.11)$$

5.4 FE partitioned model

In this section, we start from a the monodomain finite element model presented in [section 2.1.1](#) that was relevant to the metal only, referred to by the superscript M , then

present the essential assumptions and formulations that allow predicting solidification shrinkage in a Eulerian context that introduces another domain, the air, referred to by the superscript A .

5.4.1 In the metal

Mass and momentum conservation

By assuming a fixed solid phase ($\vec{v}^s = \vec{0}$), the average velocity in the metal reduces only to liquid's average velocity. Therefore, we can write:

$$\langle \vec{v} \rangle^M = \left\langle \vec{v}^l \right\rangle = g^l \vec{v}^l \quad (5.12)$$

With [eq. \(5.12\)](#), the mass balance in the metal writes:

$$\frac{\partial \langle \rho \rangle^M}{\partial t} + \nabla \cdot \langle \rho \vec{v} \rangle^M = 0 \quad (5.13a)$$

$$\frac{\partial \langle \rho \rangle^M}{\partial t} + \nabla \cdot (g^l \rho^l \vec{v}^l) = 0 \quad (5.13b)$$

$$\frac{\partial \langle \rho \rangle^M}{\partial t} + \rho^l \nabla \cdot (g^l \vec{v}^l) + g^l \vec{v}^l \cdot \vec{\nabla} \rho^l = 0 \quad (5.13c)$$

$$\nabla \cdot \langle \vec{v}^l \rangle = -\frac{1}{\rho^l} \left(\frac{\partial \langle \rho \rangle^M}{\partial t} + \langle \vec{v}^l \rangle \cdot \vec{\nabla} \rho^l \right) \quad (5.13d)$$

[Equation \(5.13d\)](#) explains the flow due to shrinkage. A negative divergence term means that a liquid feeding is necessary to compensate for the density difference, hence acting as a flow driving force in the melt. Additional terms should appear in the other conservation equations, balancing the volume change in the heat and species transport.

When the metal's density was considered constant during solidification, the assumption of an incompressible system made it possible to use the Boussinesq approximation. However, in the case of solidification shrinkage, the average density $\langle \rho \rangle^M$ varies, as it depends on the solidification path as well as on ρ^s and ρ^l which are not equal nor constant. Therefore, the incompressibility condition may not be applicable. In such case, the earlier given system [eq. \(2.41\)](#) is reformulated without any reference value

for density:

$$\left\{ \begin{array}{l} \rho^l \left(\frac{\partial \langle \vec{v}^l \rangle}{\partial t} + \frac{1}{g^l} \vec{\nabla} \cdot (\langle \vec{v}^l \rangle \times \langle \vec{v}^l \rangle) \right) = \\ - g^l \vec{\nabla} p^l - 2\mu^l \vec{\nabla} \cdot (\bar{\nabla} \langle \vec{v}^l \rangle + \bar{\nabla}^t \langle \vec{v}^l \rangle) - g^l \mu^l \mathbb{K}^{-1} \langle \vec{v}^l \rangle + g^l \rho^l \vec{g} \\ \nabla \cdot \langle \vec{v}^l \rangle = - \frac{1}{\rho^l} \left(\frac{\partial \langle \rho \rangle^M}{\partial t} + \langle \vec{v}^l \rangle \cdot \vec{\nabla} \rho^l \right) \end{array} \right. \quad (5.14)$$

Energy conservation

In the energy equation, a volumetric source term accounts for the heat dissipation caused by the shrinking metal volume. Before writing the new equation, we make the following assumptions:

- consequence of the static solid phase: $\langle \rho h \vec{v} \rangle = g^l \rho^l h^l \vec{v}^l + g^s \rho^s h^s \vec{v}^s = g^l \rho^l h^l \vec{v}^l$
- the heat generated by mechanical deformation, $\mathbb{S} : \dot{\epsilon}$, is neglected

The unknowns in the energy conservation are the average volumetric enthalpy $\langle \rho h \rangle^M$ and temperature T . The energy conservation equation writes:

$$\frac{\partial \langle \rho h \rangle^M}{\partial t} + \nabla \cdot \langle \rho h \vec{v} \rangle^M = \nabla \cdot (\langle \kappa \rangle^M \vec{\nabla} T) \quad (5.15a)$$

$$\frac{\partial \langle \rho h \rangle^M}{\partial t} + \nabla \cdot (g^l \rho^l h^l \vec{v}^l) = \nabla \cdot (\langle \kappa \rangle^M \vec{\nabla} T) \quad (5.15b)$$

$$\frac{\partial \langle \rho h \rangle^M}{\partial t} + \langle \vec{v}^l \rangle \cdot \vec{\nabla} (\rho^l h^l) = \nabla \cdot (\langle \kappa \rangle^M \vec{\nabla} T) - \rho^l h^l \nabla \cdot \langle \vec{v}^l \rangle \quad (5.15c)$$

$$\frac{\partial \langle \rho h \rangle^M}{\partial t} + \langle \vec{v}^l \rangle \cdot \vec{\nabla} (\rho^l h^l) = \nabla \cdot (\langle \kappa \rangle^M \vec{\nabla} T) + h^l \left(\frac{\partial \langle \rho \rangle^M}{\partial t} + \langle \vec{v}^l \rangle \cdot \vec{\nabla} \rho^l \right) \quad (5.15d)$$

The second term in the RHS of eq. (5.15d) is a heat power (of unit $W m^{-3}$) that adds to the system in the mushy zone. This term is proportional to the solidification rate and expresses the heat generated in regions where the average density is changing and/or a gradient of liquid density is being advected.

Species conservation

The last conservation principle is applied to the chemical species or solutes. This principle allows predicting macrosegregation when applied to a solidification system, along with the mass, momentum and energy balances. However, the conservation

Chapter 5. Macrosegregation with solidification shrinkage

equation should be reformulated in the case of a melt flow driven by shrinkage. Assumptions

- the solidification path is tabulated using thermodynamic data at equilibrium
- the macroscopic solute diffusion coefficient D^s in the solid phase is neglected in the mass diffusive flux term.
- consequence of the static solid phase: $\langle \rho w \vec{v} \rangle^M = g^l \rho^l \langle w \rangle^l \vec{v}^l + \cancel{g^s \rho^s \langle w \rangle^s \vec{v}^s} = g^l \rho^l \langle w \rangle^l \vec{v}^l$

The species conservation is pretty similar the energy conservation formulated in the previous section. The main difference is the breakup of the volumetric variable $\langle \rho w \rangle^M$ into a product of density $\langle \rho \rangle^M$ and the mass concentration $\langle w \rangle^M$. For a binary alloy, we write:

$$\frac{\partial \langle \rho w \rangle^M}{\partial t} + \nabla \cdot \langle \rho w \vec{v} \rangle^M - \nabla \cdot \left(\langle D^l \rangle \vec{\nabla} (\rho^l \langle w \rangle^l) \right) = 0 \quad (5.16a)$$

$$\langle \rho \rangle^M \frac{\partial \langle w \rangle^M}{\partial t} + \langle w \rangle^M \frac{\partial \langle \rho \rangle^M}{\partial t} + \nabla \cdot \left(g^l \rho^l \langle w \rangle^l \vec{v}^l \right) - \nabla \cdot \left(g^l D^l \vec{\nabla} (\rho^l \langle w \rangle^l) \right) = 0 \quad (5.16b)$$

$$\begin{aligned} & \langle \rho \rangle^M \frac{\partial \langle w \rangle^M}{\partial t} + \langle w \rangle^M \frac{\partial \langle \rho \rangle^M}{\partial t} + (\rho^l \langle w \rangle^l) \nabla \cdot \langle \vec{v}^l \rangle + \langle \vec{v}^l \rangle \cdot \vec{\nabla} (\rho^l \langle w \rangle^l) \\ & - \nabla \cdot (g^l D^l \vec{\nabla} (\rho^l \langle w \rangle^l)) = 0 \end{aligned} \quad (5.16c)$$

The mass balance gives the following relation when the liquid density is constant:

$$\nabla \cdot \langle \vec{v}^l \rangle = -\frac{1}{\rho^l} \left(\frac{\partial \langle \rho \rangle^M}{\partial t} \right) \quad (5.17)$$

If we use the result of eq. (5.17) in eq. (5.16c), then we get the following equation:

$$\langle \rho \rangle^M \frac{\partial \langle w \rangle^M}{\partial t} + \langle w \rangle^M \frac{\partial \langle \rho \rangle^M}{\partial t} = \langle w \rangle^l \frac{\partial \langle \rho \rangle^M}{\partial t} - \langle \vec{v}^l \rangle \cdot \vec{\nabla} (\rho^l \langle w \rangle^l) + \nabla \cdot (g^l D^l \vec{\nabla} (\rho^l \langle w \rangle^l)) \quad (5.18)$$

Applying Voller-Prakash [Voller et al. 1989] variable splitting, the system ends up with only one variable, $\langle w \rangle^M$. The splitting is done as follows:

$$\langle w \rangle^l = (\langle w \rangle^l)^t + \langle w \rangle^M - (\langle w \rangle^M)^t \quad (5.19)$$

where the superscript t refers to the previous time step. The chemical species conservation writes:

$$\begin{aligned} \langle \rho \rangle^M \frac{\partial \langle w \rangle^M}{\partial t} + \cancel{\langle w \rangle^M \frac{\partial \langle \rho \rangle^M}{\partial t}} = \\ \cancel{\langle w \rangle^M \frac{\partial \langle \rho \rangle^M}{\partial t}} - \rho^l \langle \vec{v}^l \rangle \cdot \vec{\nabla} \langle w \rangle^M + \nabla \cdot (g^l \rho^l D^l \vec{\nabla} \langle w \rangle^M) \\ + \frac{\partial \langle \rho \rangle^M}{\partial t} \left[(\langle w \rangle^l)^t - (\langle w \rangle^M)^t \right] - \rho^l \langle \vec{v}^l \rangle \cdot \vec{\nabla} \left((\langle w \rangle^M)^t - (\langle w \rangle^l)^t \right) \end{aligned} \quad (5.20a)$$

$$\begin{aligned} \langle \rho \rangle^M \frac{\partial \langle w \rangle^M}{\partial t} + \rho^l \langle \vec{v}^l \rangle \cdot \vec{\nabla} \langle w \rangle^M - \nabla \cdot (g^l \rho^l D^l \vec{\nabla} \langle w \rangle^M) = \\ - \frac{\partial \langle \rho \rangle^M}{\partial t} \left[(\langle w \rangle^M)^t - (\langle w \rangle^l)^t \right] + \rho^l \langle \vec{v}^l \rangle \cdot \vec{\nabla} \left((\langle w \rangle^M)^t - (\langle w \rangle^l)^t \right) \end{aligned} \quad (5.20b)$$

$$\begin{aligned} \langle \rho \rangle^M \frac{\partial \langle w \rangle^M}{\partial t} + \rho^l \langle \vec{v}^l \rangle \cdot \vec{\nabla} \langle w \rangle^M - \nabla \cdot (g^l \rho^l D^l \vec{\nabla} \langle w \rangle^M) = \\ - \frac{\partial \langle \rho \rangle^M}{\partial t} \left[(\langle w \rangle^M)^t - (\langle w \rangle^l)^t \right] \\ + \rho^l \langle \vec{v}^l \rangle \cdot \vec{\nabla} \left((\langle w \rangle^M)^t - (\langle w \rangle^l)^t \right) - \nabla \cdot \left[g^l \rho^l D^l \vec{\nabla} \left((\langle w \rangle^M)^t - (\langle w \rangle^l)^t \right) \right] \end{aligned} \quad (5.21)$$

It is noted that eq. (5.21) is valid only if both densities ρ^l and ρ^s are constant but have different values. Since density changes are incorporated in this equation, inverse segregation following solidification shrinkage is predicted. For the case where macrosegregation is solely due to fluid flow generated by natural or forced convection, i.e. no shrinkage occurs whether due to thermal-solutal contraction or phase change, the overall volume remains constant, hence density is constant. In this situation, $\rho^s = \rho^l = \langle \rho \rangle$ and the term $\partial \langle \rho \rangle / \partial t$ therefore vanishes. After dividing both sides by $\langle \rho \rangle = \rho^l$, eq. (5.21) reduces to:

$$\begin{aligned} \frac{\partial \langle w \rangle^M}{\partial t} + \langle \vec{v}^l \rangle \cdot \vec{\nabla} \langle w \rangle^M - \nabla \cdot (g^l D^l \vec{\nabla} \langle w \rangle^M) \\ = \langle \vec{v}^l \rangle \cdot \vec{\nabla} \left((\langle w \rangle^M)^t - (\langle w \rangle^l)^t \right) - \nabla \cdot \left[g^l D^l \vec{\nabla} \left((\langle w \rangle^M)^t - (\langle w \rangle^l)^t \right) \right] \end{aligned} \quad (5.22)$$

5.4.2 In the air

The presence of an air domain in our approach is important to follow the free surface of the solidifying metal. For this particular reason, some assumptions are introduced

Chapter 5. Macrosegregation with solidification shrinkage

and explained in this section in order to limit unnecessary treatment within the air, since it does not undergo phase change. It should be reminded that we consider air as a single-phase system, hence superscripts A and a are interchangeably used.

Mass and momentum conservation

To simplify fluid flow resolution in the air, we consider it as incompressible. This assumption is acceptable in the context of casting processes where air velocity has an insignificant order of magnitude. Therefore, the free metal surface is not disturbed by air flow in its vicinity. With the incompressibility of air, we are saying that any deformation of the free surface is solely due to an air mass increase, coming from the system boundaries. The mass balance hence writes:

$$\nabla \cdot \langle \vec{v} \rangle^A = \nabla \cdot \vec{v}^a = 0 \quad (5.23)$$

The air flow is governed by time-dependent incompressible Navier-Stokes equations, as previously done for the metal:

$$\left\{ \begin{array}{l} \rho^a \left(\frac{\partial \vec{v}^a}{\partial t} + \vec{\nabla} \cdot (\vec{v}^a \times \vec{v}^a) \right) = \\ - \vec{\nabla} p^a - 2\mu^a \vec{\nabla} \cdot (\vec{\nabla} \vec{v}^a + \vec{\nabla}^t \vec{v}^a) + \rho^a \vec{g} \\ \nabla \cdot \vec{v}^a = 0 \end{array} \right. \quad (5.24)$$

The air density ρ^a is considered constant along the casting process, therefore thermal gradients in the air that arise due to the low thermal conductivity, do not generate any flow, i.e. no Boussinesq approximation is made on the term $\rho^a \vec{g}$ in eq. (5.24).

Energy conservation

It was mentioned in the introduction of the current section that air is a single-phase system that cannot undergo any phase change. Therefore, heat transfer in this domain simplifies to pure thermal conduction with a low thermal conductivity coefficient, $\langle \kappa \rangle^a$. The energy balance governs the air enthalpy $\langle \rho h \rangle^A$ (which is equal to $\rho^a h^a$ in the

current context) as follows:

$$\frac{\partial \langle \rho h \rangle^A}{\partial t} + \nabla \cdot (\langle \rho h \vec{v} \rangle^A) = \nabla \cdot (\langle \kappa \rangle^A \vec{\nabla} T) \quad (5.25a)$$

$$\frac{\partial \langle \rho h \rangle^A}{\partial t} + \nabla \cdot (\rho^a h^a \vec{v}^a) = \nabla \cdot (\langle \kappa \rangle^a \vec{\nabla} T) \quad (5.25b)$$

$$\frac{\partial \langle \rho h \rangle^A}{\partial t} + \vec{v}^a \cdot \vec{\nabla} (\rho^a h^a) = \nabla \cdot (\langle \kappa \rangle^a \vec{\nabla} T) \quad (5.25c)$$

Species conservation

The composition of alloying elements is crucial quantity to predict in this work. Nevertheless, such prediction is only relevant in the metallic alloy, even if the air is also made up of other chemical species (nitrogen, oxygen ...). For this obvious reason, the species conservation equation should not be solved in the air, but that of course is contradictory to the principle of a monolithic approach. Consequently, we should compute the conservation of chemical species in both the metal and the air, considering the latter as a *fictitious metal*, thus having initially the same solute mass composition, $\langle w_0 \rangle^M = \langle w_0 \rangle^A$. Then, we limit as much as possible solute transport between these domains by limiting solute advection and diffusion. The computed air velocity, \vec{v}^a , will not be used but rather a zero-velocity vector instead, thus suppressing the solute advection term influence. As for solute diffusion, a very low macroscopic solute diffusion coefficient is used, ensuring that its order of magnitude is at most a thousand times less than that in the melt, $D^a \ll D^l$. The low artificial diffusion in the air may slightly violate the wanted no-exchange condition at the air-liquid interface, but it is acceptable since suppressing the diffusion term in the air would result in a numerically stiff partial differential equation.

$$\langle \rho \rangle^A \frac{\partial \langle w \rangle^A}{\partial t} - \nabla \cdot (D^a \vec{\nabla} (\rho^a \langle w \rangle^a)) = 0 \quad (5.26)$$

In contrast to [eq. \(5.21\)](#) for the metal, solute balance in the air, given by [eq. \(5.26\)](#), provides a linear equation as we consider a special case where the domain is monophase, therefore: $\langle w \rangle^A = \langle w \rangle^a$ at all times. Otherwise, we would have applied the variable decomposition done earlier in [eq. \(5.19\)](#) to linearise the equation.

5.5 FE monolithic model

5.5.1 Monolithic equations

The monolithic model combines all conservation equations derived for metal and air in a unique set of equations, to be solved on a fixed mesh. This can be accomplished by using the Heaviside function (defined in [section 2.4.1](#)) relative to each domain, creating a mixture of properties that vary across the interface according to a specified mixing law. However, one of the main technical difficulties of the monolithic resolution is that the obtained equation should be consistent with each domain's original equation regarding its shape and terms, making its resolution easier. While for energy and solute balances the procedure is straightforward, the presence of the Darcy dissipative term in the metal's Navier-Stokes system makes it more difficult to formulate a single monolithic equation, which is discussed after writing the equations of the monolithic model.

Mass and momentum conservation

For the system's velocity, $\langle \vec{v}^F \rangle$, is given by an arithmetic mixing between each domain's relative average fluid velocity, i.e. we need the relative fluid velocity with respect to other fixed/rigid phases in each domain. In the present context, the metal domain consists of a single fluid phase (liquid) and solid phases that form in fixed and rigid structures (assuming that solidification results in an undeformable columnar dendritic and eutectic structures, without any free equiaxed dendritic structure), while the latter domain entirely consists of a fluid phase (air). With this notation, we express the monolithic mass balance as:

$$\nabla \cdot \langle \vec{v}^F \rangle = \nabla \cdot (H^M \langle \vec{v} \rangle^M + H^A \langle \vec{v} \rangle^A) \quad (5.27)$$

$$\nabla \cdot \langle \vec{v}^F \rangle = H^M \nabla \cdot \langle \vec{v} \rangle^M + H^A \nabla \cdot \langle \vec{v} \rangle^A + \vec{\nabla} H^M \cdot (\langle \vec{v} \rangle^M - \langle \vec{v} \rangle^A) \quad (5.28)$$

$$\nabla \cdot \langle \vec{v}^F \rangle = H^M \nabla \cdot \langle \vec{v}^l \rangle \quad (5.29)$$

where we used the relation [eq. \(5.12\)](#) in the case of a fixed rigid solid to obtain [eq. \(5.29\)](#). As for the second term in [eq. \(5.28\)](#), we have made the assumption that air is incompressible. Therefore any volume variation of the metal domain, will trigger an air inflow or suction effect through the surface boundaries of the air domain. The third and last term in the same equation expresses a velocity jump at the interface. In our case, we neglect this contribution by assuming that both velocities tend to be equal when the interface thickness tends to zero. Finally, the monolithic mass balance

writes:

$$\nabla \cdot \langle \vec{v}^F \rangle = H^M \left(-\frac{1}{\rho^l} \left(\frac{\partial \langle \rho \rangle^M}{\partial t} + \langle \vec{v}^l \rangle \cdot \vec{\nabla} \rho^l \right) \right) \quad (5.30)$$

The momentum balance looks like the one derived for the metal, but using level set mixed properties, we get the following:

$$\begin{cases} \hat{\rho} \left(\frac{\partial \langle \vec{v}^F \rangle}{\partial t} + \frac{1}{g^F} \vec{\nabla} \cdot (\langle \vec{v}^F \rangle \times \langle \vec{v}^F \rangle) \right) = \\ - g^F \vec{\nabla} p - 2\hat{\mu} \vec{\nabla} \cdot (\vec{\nabla} \langle \vec{v}^F \rangle + \vec{\nabla}^t \langle \vec{v}^F \rangle) - g^F \hat{\mu} \tilde{\mathbb{K}}^{-1} \langle \vec{v}^F \rangle + \hat{\rho} g \vec{g} \\ \nabla \cdot \langle \vec{v}^F \rangle = H^M \left(-\frac{1}{\rho^l} \left(\frac{\partial \langle \rho \rangle^M}{\partial t} + \langle \vec{v}^l \rangle \cdot \vec{\nabla} \rho^l \right) \right) \end{cases} \quad (5.31)$$

Note that the Darcy term has a special treatment explained in the next section. The mechanical properties are mixed as follows:

$$\text{Fluid fraction : } g^F = H^M g^l + H^A g^a = H^M g^l + H^A \quad (5.32)$$

$$\text{Density : } \hat{\rho} = H^M \rho^l + H^A \rho^a \quad (5.33)$$

$$\text{Dynamic viscosity : } \hat{\mu} = H^M \mu^l + H^A \mu^a \quad (5.34)$$

$$\text{Weight force : } \hat{\rho} g \vec{g} = H^M g^l \rho^l \vec{g} + H^A g^a \rho^a \vec{g} = H^M g^l \rho^l \vec{g} + H^A \rho^a \vec{g} \quad (5.35)$$

We defined a fluid fraction, g^F , as an arithmetic mixing between liquid and air fractions across the interface. This quantity will be essential for the monolithic Darcy term. As for the weight force in both domains, it is taken into account via eq. (5.35). The phase densities may vary as functions of other parameters such as temperature or phase composition (ρ^l depends on both), creating buoyancy forces of convection inside the fluid. In our approach, since we are only interested in liquid's flow, we keep the air phase density ρ^a constant, so as to prevent a mixture of forces around the level set, which helps stabilise the fluid flow resolution.

Chapter 5. Macrosegregation with solidification shrinkage

Energy conservation

Deriving the monolithic energy conservation equation is straightforward. The monolithic system writes:

$$\frac{\partial \widehat{\langle \rho h \rangle}}{\partial t} + \left\langle \vec{v}^F \right\rangle \cdot \vec{\nabla} \widehat{\langle \rho h \rangle^F} = \nabla \cdot \left(\widehat{\langle \kappa \rangle} \vec{\nabla} T \right) + \widehat{\Phi} \quad (5.36)$$

The solution of [eq. \(5.36\)](#) is $\widehat{\langle \rho h \rangle}$, a mixed field between both domains average volumetric enthalpies. The other parameters are $\widehat{\langle \rho h \rangle^F}$ and $\widehat{\langle \kappa \rangle}$ which denote respectively the fluids' mixture volume enthalpy and the mixture of average thermal conductivities. The last term, $\widehat{\Phi}$, is an average heat source accounting for energy change caused by the alloy's shrinking volume. As no volume change was considered for the air, $\widehat{\Phi}$ is present only in the metal's energy balance. These quantities are defined in the following equations:

$$\text{Total enthalpy : } \widehat{\langle \rho h \rangle} = H^M \langle \rho h \rangle^M + H^A \langle \rho h \rangle^A \quad (5.37)$$

$$\text{Fluid phases enthalpy : } \widehat{\langle \rho h \rangle^F} = H^M \rho^l h^l + H^A \rho^a h^a \quad (5.38)$$

$$\text{Average thermal conductivity : } \widehat{\langle \kappa \rangle} = H^M \langle \kappa \rangle^M + H^A \langle \kappa \rangle^A \quad (5.39)$$

$$\text{Average heat change : } \widehat{\Phi} = H^M \rho^l h^l \nabla \cdot \left\langle \vec{v}^l \right\rangle \quad (5.40)$$

Species conservation

As previously explained in [section 5.4.2](#), we consider that species conservation is solved over both domains, as follows:

$$\begin{aligned} & \langle \rho \rangle^M \frac{\partial \widehat{\langle w \rangle}}{\partial t} + \rho^l \left\langle \vec{v}^l \right\rangle \cdot \vec{\nabla} \widehat{\langle w \rangle} - \nabla \cdot \left(g^l \rho^l D^l \vec{\nabla} \widehat{\langle w \rangle} \right) = \\ & - \frac{\partial \langle \rho \rangle^M}{\partial t} \left[\left(\langle w \rangle^M \right)^t - \left(\langle w \rangle^l \right)^t \right] \\ & + \rho^l \left\langle \vec{v}^l \right\rangle \cdot \vec{\nabla} \left(\left(\langle w \rangle^M \right)^t - \left(\langle w \rangle^l \right)^t \right) - \nabla \cdot \left[g^l \rho^l D^l \vec{\nabla} \left(\left(\langle w \rangle^M \right)^t - \left(\langle w \rangle^l \right)^t \right) \right] \end{aligned} \quad (5.41)$$

then we deduce the metal's solute composition by postprocessing the obtained solution.

i should multiply solid fraction by HeavisideM before Sortie to correct the visu. no problem for resolution as in Tsolver HeavisideA is taken into account then next time step's T2H will determine a raw solid fraction in the air and the metal

i should create a new FeC tabulation with concentration variation. Once done, revert to 5 times the Concentration parameter in the ChampParametre of Tsolver and T2H

5.5.2 Darcy term in the air

We have seen in the previous chapter that adding the Darcy term into Navier-Stokes system modifies the shape of the equation, dividing all terms by the liquid fraction, g^l (REF VMS SOLVER CHAPTER 4). The presence of this dissipation term in one domain, obliges us to keep it in both domains but "deactivate" it where it is useless, i.e. in the air. This is done by computing a fictitious permeability in the air as function of the air fraction using the Carman-Kozeny model, as used previously for the metal in [eq. \(1.3\)](#). We may speak of level set mixing for the Darcy term. It has a double advantage:

1. the consistency in shape is kept between both domains equations, thus easily deriving the monolithic system;
2. since the monolithic system retains the shape of the monodomain equation, the VMS solver does not require further implementation updates and subsequent validation.

$$\tilde{K} = \frac{\lambda_2^2 g^F}{180 (1 - g^F)^2} \quad (5.42)$$

then from the fluid fraction ([eq. \(5.32\)](#)), we deduce a modified permeability, \tilde{K} . Depending on the values of this quantity, the extent to which the Darcy becomes imposing in Navier-Stokes varies as follows:

- $\tilde{K}^{-1} \rightarrow 0$ (completely permeable), then Darcy's term is negligible in Navier-Stokes resolution,
- $\tilde{K}^{-1} > 0$ (slightly permeable), then fluid flow is greatly dissipated due to a decreasing permeability,
- $\tilde{K}^{-1} \rightarrow \infty$ (non permeable), then no fluid flow may exist.

These 3 cases are graphically represented in [fig. 5.4](#), showing the different values along with the transitions with respect to phases and domains distribution. It is clear that neither in liquid nor air, the flow is dissipated by the presence of the Darcy term in the monolithic system, which is confirmed in REF FIGURE DRAW DARCY/PERMEABILITY FROM LIQUID FRACTION RESULT.

5.5.3 Interface motion and stability

In chapter 2, we have presented the transport equation of the distance function using the velocity solution provided by solving momentum conservation equations. In this

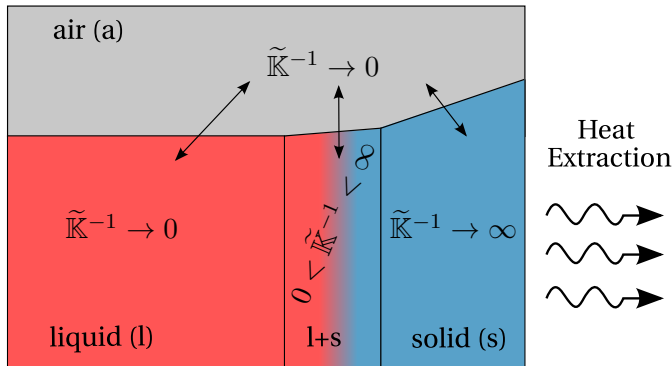


Fig. 5.4 – Schematic representation of an ingot undergoing solidification while shrinking. The inverse of the modified permeability, \tilde{K}^{-1} , falls to zero in the air and liquid phases, indicating that the Darcy term is only activated in the solid and liquid+solid regions. The arrows indicate three different transitions of the Darcy term between the air and metal domains.

section, we discuss some important points regarding the stability of the interface while being transported. When real values are assigned for the mechanical properties, especially density, a ratio of three orders of magnitude exists in the diffuse interface. This high ratio may badly influence the stability of the interface, unless we pay attention to the order of the integration method as well as the time step used in Navier-Stokes resolution.

Integration order influence

Time step influence

In the first tests, we noticed

TRY TIME STEP 0.01 sec (stable) and 0.02 sec (unstable): is CFL the cause ?

Classical coupling

A "classical" coupling comes in the sense of "unmodified" coupling. This approach consists of taking the output of the fluid mechanics solver, then feed it as raw input to level set transport solver. The physical translation would be that the interface motion is dictated by the fluids flow in its vicinity. No treatment whatsoever is done between the two mentioned steps. While conservation principles are best satisfied with this approach, the latter yields some drawbacks, preventing its application in a generic way. For instance, the free liquid surface is not necessarily horizontal at all times and that can lead to the wrong shrinkage profile when solidification is complete.

present the example of unstable interface when the ratio between fluids properties became greater than some value+discussion

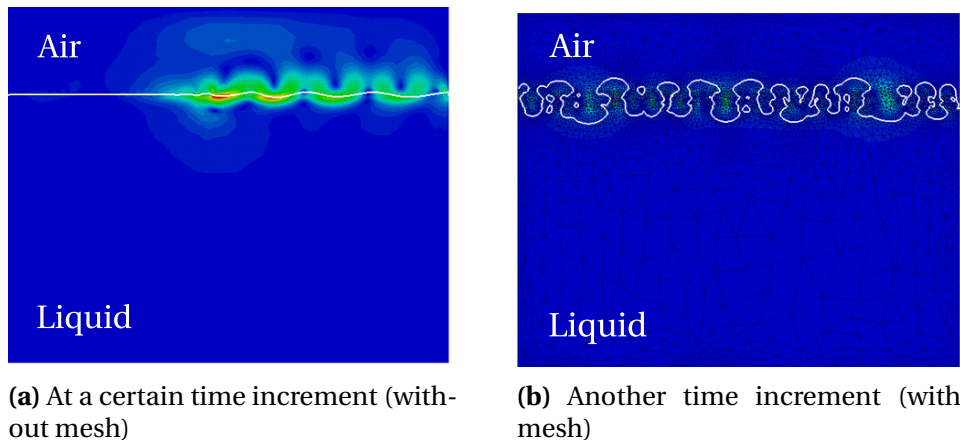


Fig. 5.5 – Interface destabilisation under the effect of high properties ratio across the interface.

Modified coupling

In contrast to a classic coupling, here we attempt to modify the velocity field before feeding to the transport solver. The main motivation for considering this approach is the lack of stability that we observed whenever the mechanical properties of the fluids were different by several orders of magnitude. The algorithm should simultaneously fulfil these requirements:

- support high ratios of fluids density with close viscosities by preserving an non-oscillating interface,
- maintain a horizontal level at the free surface of the melt,
- follow shrinking metal surface profile in solidifying regions,
- satisfy the mass conservation principle, essentially in the metal.

We want to process the original transport velocity by imposing a uniform motion (speed and direction) at the nodes of the free surface, and at the same time, be able to follow the pipe formation at the surface as a result of solidification shrinkage, as shown in [fig. 5.6](#).

How to transport level set using velocity from momentum conservation DIRECTLY or AVERAGED PER ELEMENTS, show examples of instability/stability when using false/nominal air properties

Validation of LS transport: perform test case simulation of buoyancy driven air droplet in water by 2005Nagrath that I also have seen in Shyamprasad's masters report). => I didnt notice: what time step δt did they use ?

The general idea is read the velocity around the interface up to a certain thickness, which may be the same thickness as the diffuse interface defined in [section 2.4.1](#), then compute a volumetric average from all the elements in the thickness. This average

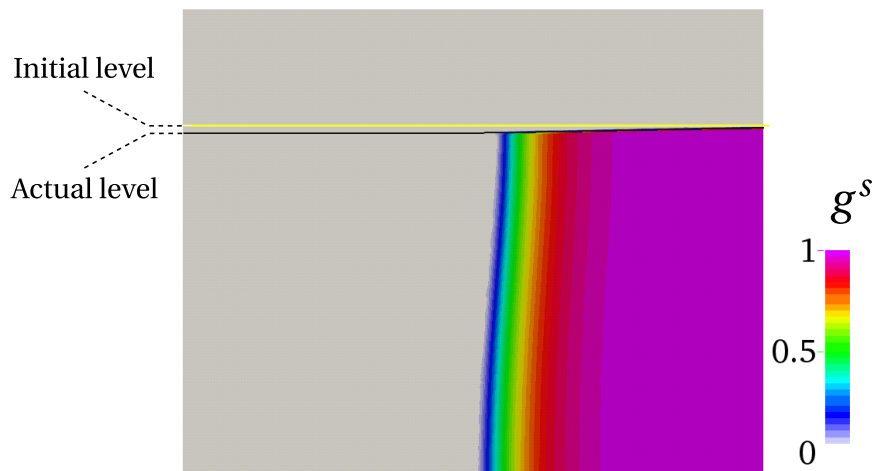


Fig. 5.6 – Snapshot of a solidifying ingot by a cooling flux from the side. The profile of the actual surface changes in solid and mushy regions to adapt the new density while staying perfectly horizontal in the liquid phase.

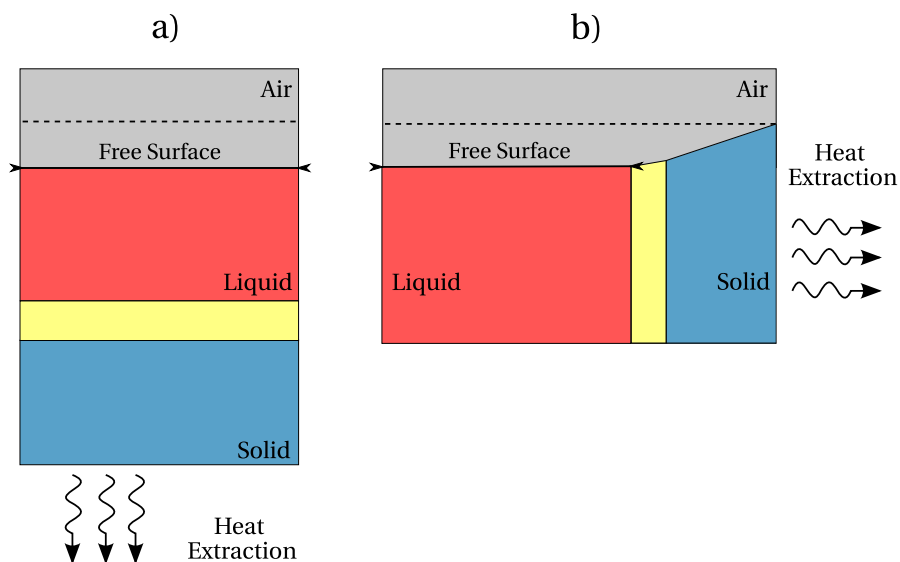


Fig. 5.7 – Treatment of liquid free surface in a) bottom and b) side heat extraction configurations. The dashed line represents the initial level of the free liquid surface.

5.6. 1D application: solidification with inverse segregation

is then given to the transport solver, which will apply the same magnitude and direction to transport the interface. However, as we only need the transport velocity to be uniform within the "100% liquid" elements, it should not be the case for the other elements that belong either to the mushy zone or the solid region, where shrinkage is taking place. Therefore, depending on the heat extraction configuration, two scenarios are possible. If heat extraction is far from the interface, i.e. there is not direct contact as in [fig. 5.7a](#), the surface area remains unchanged at any time, hence all the elements around the interface are "100% liquid". This happens when a bottom cooling is applied to the ingot. In contrast, if a side cooling is applied as shown in [fig. 5.7b](#), the surface area of the interface will be reduced over time as a consequence of the solid front progression. In this case, the average transport velocity should be computed only from the elements belonging to the free surface. The remaining part of the interface which belongs to partial or full solid regions, is transported with Navier-Stokes output, which should be some orders of magnitude less than the velocity imposed at the free surface, as a result of a decreasing permeability.

5.6 1D application: solidification with inverse segregation

5.6.1 Geometry and boundary conditions

A simple but very efficient way of analysing the model is to test it through a 1D flow configuration with energy and species conservation. For this purpose, we take an aluminium-silicon alloy with the same properties used for the thermal solver validation in [table 3.2](#). The major difference with respect to the former validation setup is the air domain that should also be included in the mesh. We consider a 2D rod having as dimensions $0.14\text{ m} \times 0.001\text{ m}$, where initially the air column's height is only 0.04 m and the remainder of the length is for the metal. **FIGURE** shows the geometry, mesh used for this section simulations, while **FIGURE** shows the thermal and mechanical boundary conditions. In the latter, velocity-slip conditions were imposed on the lateral boundaries while a no-slip was used at the bottom where heat is extracted, to ensure a 1D air flow from the free air inlet at the top.

In this case, imposing slip conditions on lateral sides is two-fold: on one hand, we need to ensure that the fluid flow solution remain one-dimensional, hence symmetry on the boundaries solves the issue, while on the other hand during solidification, the resulting feeding flow should be able to transport the interface intersecting with boundary nodes. If boundary velocities are zero, then the interface transport will face problems at these boundary nodes. This is indeed an important and relevant point in

the next 2D test case.

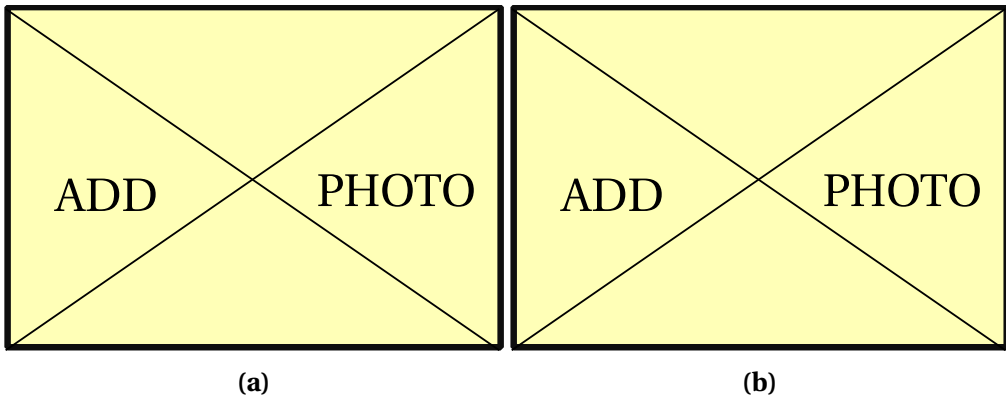


Fig. 5.8 – Geo and boundary conditions

5.6.2 Shrinkage without macrosegregation

The first simulation is the solidification without any segregation, hence a unique solidification path is considered at $w_0 = \text{Al-7 wt.\% Si}$, shown in [fig. 5.10](#). This case is interesting as a reference case, where we can study volume shrinkage and level set behaviour in a simple segregation-free configuration. We first use a homogeneous isotropic mesh of constant size $h = 200 \mu\text{m}$. The liquid and solid phase densities are assumed constant and respectively equal to 2600 kg m^{-3} and 2800 kg m^{-3} . This density difference is equivalent to a ratio of $\beta_{SS} = (\rho^s - \rho^l) / \rho^s$, also termed as *solidification shrinkage* by [Flemings et al. \[1967\]](#). In the current conditions, β_{SS} is constant and equal to 7.14 %. The domain is initially meshed before any resolution, as shown in [fig. 5.9](#), in a way to reduce interpolation errors that may cause coarse elements within the transition of fluids density and dynamic viscosity, reminding that these parameters are crucial for the stability of the velocity solution used later in the transport step. The chosen mixing laws are arithmetic for the density and logarithmic for the viscosity. The choice is based on tests done in former Ph.D. projects at CEMEF. The initial mesh sizes are given in [table 5.1](#).

At a first glance, results show that the interface stability is compromised by a chosen time step for a given mesh size, and that the interface dynamics require attention even before investigating the feeding flow created by solidification. As a demonstration, [fig. 5.11](#) shows different time steps with the same adaptive meshing parameters. For time steps greater than 0.01 s, Navier-Stokes computations did not converge resulting in an high artificial flow quickly destabilising the interface. It should be noted that the frame corresponding to 0.02 s was taken at an earlier time than the two other frames.

5.6. 1D application: solidification with inverse segregation

Table 5.1 – Summary of the different mesh sizes used to generate an adaptive anisotropic mesh, along with the level mixing thickness, ε . Refer to section 2.6.2 for the definition of each mesh parameter.

Mesh parameter	Size [m]
ε	2.5×10^{-4}
$h_{\vec{n}}$	2.5×10^{-5}
$h_{\vec{\tau}}$	2×10^{-4}
h_M	1.5×10^{-4}
h_A	2.5×10^{-4}

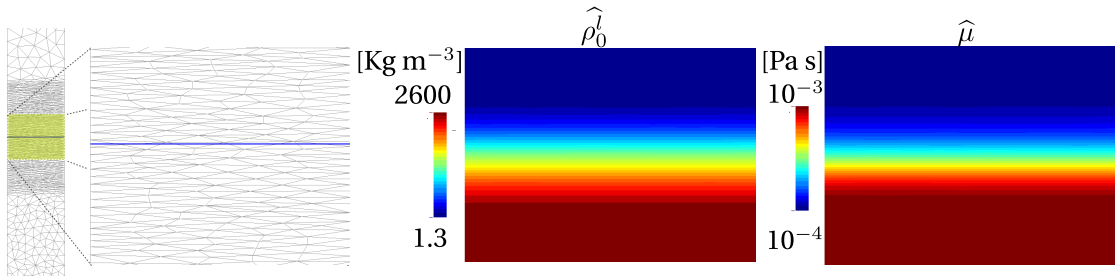


Fig. 5.9 – Snapshots of the initial adapted mesh around the interface with different mesh sizes in the air and the metal. The adapted region is stretched beyond the level set mixing thickness to ensure better interpolation around the interface, in case of emergence of diffusion instabilities. To the right, the reference fluid density and viscosity are plotted in the transition zone, showing a symmetric mixing for the former and a shifted mixing for the latter, as a consequence of the mixing laws. The thick blue line represents the zero iso-value of the distance function.

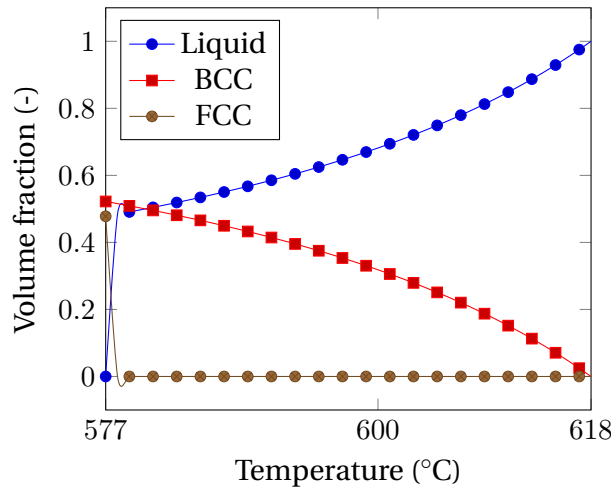


Fig. 5.10 – Unique solidification path at nominal composition for the shrinkage case without macrosegregation.

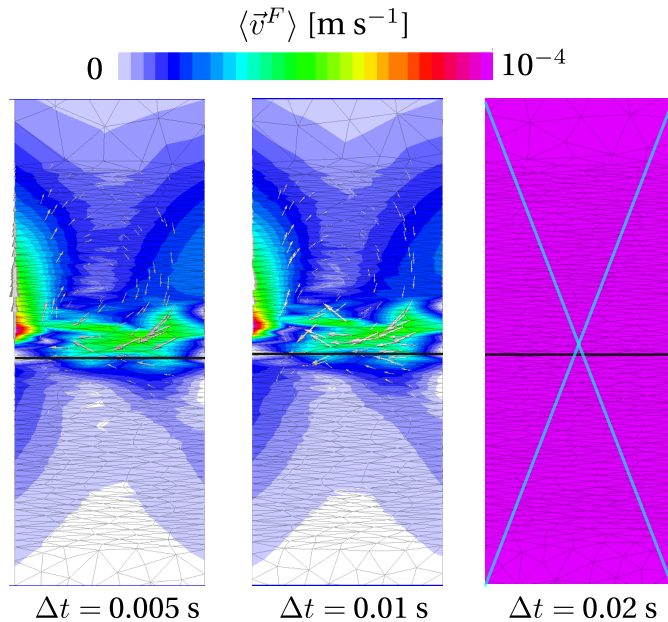


Fig. 5.11 – Three average fluid velocity frames at different time steps: 0.005 s, 0.01 s and 0.02 s. The first and second frame are taken after 50 seconds of cooling while for the last frame, the frame was taken after only 1 second of cooling, thus it is crossed to show non-convergence. The thick black line represents the zero iso-value of the distance function.

Although no solidification has yet started at 100 s, a two-dimensional flow is observed around the interface, while tends to 10^{-8} m s^{-1} elsewhere in the ingot. Figure 5.11 confirms that this flow is still predicted at smaller time steps. This flow seems like a pure numerical response to the properties jump across the interface, namely density and dynamic viscosity. It is also noted that the interface position is not modified by the neighbouring currents, that reach a maximum magnitude of 10^{-4} m s^{-1} . Therefore, the optimal time step for this simulation is set to 0.01 s, and we refer to it as case R, which stands for "real" air.

The fact that properties transition is crucial in the solution stability, is investigated by 2 reference cases, having equal properties (density and dynamic viscosity) but with different time steps, 0.01 (case A1) and 0.1 s (case A2), where "A" stands for artificial. All simulation cases are grouped in table 5.2.

Table 5.2 – Summary of the comparative shrinkage simulations without macrosegregation.

Case	Air viscosity [Pa s]	Air density [kg m^{-3}]	Time step [s]
A1	10^{-3}	2600	0.01
A2	10^{-3}	2600	0.1
R	10^{-4}	1.3	0.01

5.6. 1D application: solidification with inverse segregation

When the air subdomain is given the metal's properties, it becomes denser and more viscous by several orders of magnitude. [Figure 5.12](#), in which cases A1 and A2 are compared, shows no noticeable sign of velocity instability near the interface before 200 s. It can be explained by the fact that the air behaves mechanically like a fluid metal given similar properties, therefore no steep transitions are computed at the interface. However, it is interesting to compare results of [fig. 5.12a](#) and [fig. 5.12b](#) at 600 s. For case A1, the interfaces is slightly skewed due to slower flow at the left side of the interface, while for case A2, the flow disturbs the interface deforming it until the end of solidification, as seen at 1000 s. This shows the importance of the chosen time step in both the Navier-Stokes solver. We can also notice a common issue for all three case, A1, A2 and R, approximately at 400 s, the mushy zone enters within the diffuse interface, affecting the level set transport and thus causing mass conservation problems. These problems are discussed in the next section.

In contrast, [fig. 5.13b](#) shows more viable results as far as the level set transport is concerned. From 200 s to 800 s, the local flow instability (discussed earlier in [fig. 5.11](#)) is sustained, even until after solidification is complete. However, in regions of 100% metal and 100% air the computed velocity is nearly the same order of magnitude as predicted for all three simulations. Finally, in [fig. 5.13b](#), we notice a recirculating air flow in the vicinity of the interface as no metal shrinkage may further occur once solidification is complete, thus air flows freely in and out of the upper boundary with a very low magnitude ($\sim 10^{-7} \text{ m s}^{-1}$), while impinging on the air-metal surface. Regarding the CPU times, cases A1 ran for 14 hours, case A2 took only 2 hours while case R ran for 23.3 hours.

Mass conservation study

The previous computations showed that the mass conservation, which is the consequence of the level set transport, can be lost. In order to better understand the process, we define the metal's mass as a function of the metal's average density and the Heaviside function relative to the metal subdomain, as follows:

$$m^M = \int_{\Omega} H^M \langle \rho \rangle^M \, d\Omega \quad (5.43)$$

Then, the mass conservation can be monitored by processing [eq. \(5.43\)](#) at each time step, and computing the relative mass change by writing:

$$m_{\%}^M = \frac{m^M - m_i^M}{m_i^M} \times 100 \quad (5.44)$$

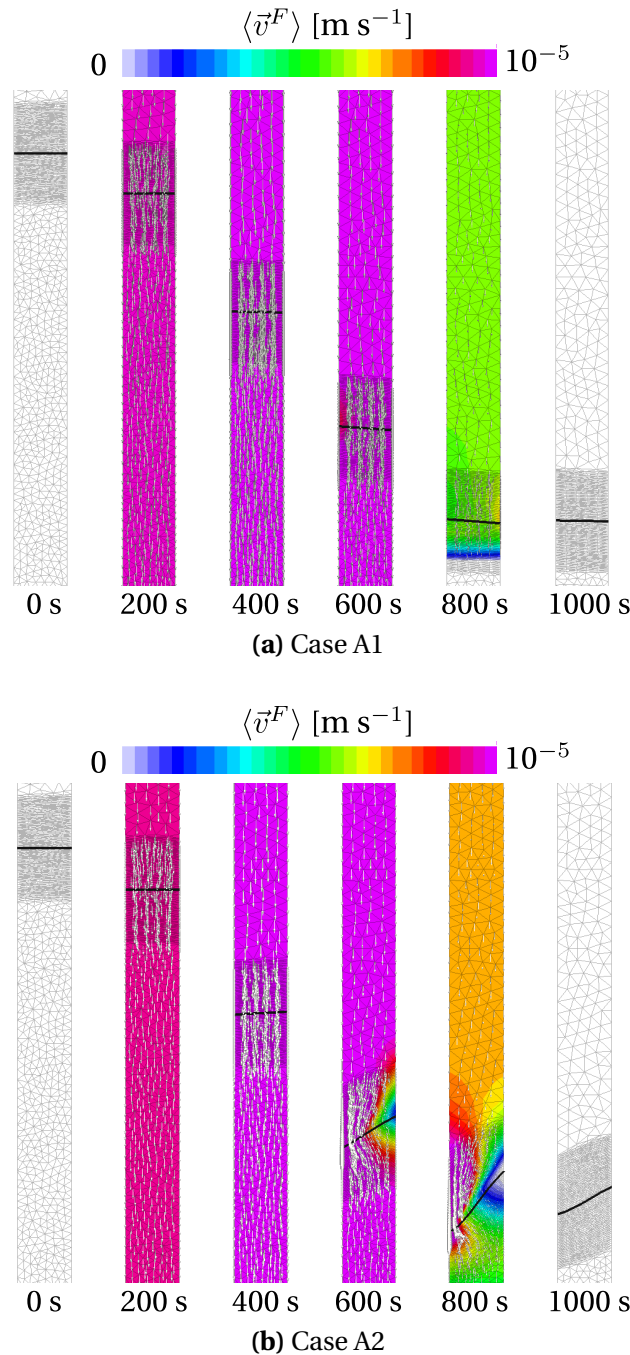


Fig. 5.12 – Comparison of two simulations in several stages of solidification ending shortly after 800 s. The results shows the influence of density and viscosity properties across the level set interface. The plotted field is the average fluid velocity, on which the corresponding nodal vectors are superimposed, pointing towards the solidification front. The thick black line represents the zero iso-value of the distance function.

5.6. 1D application: solidification with inverse segregation

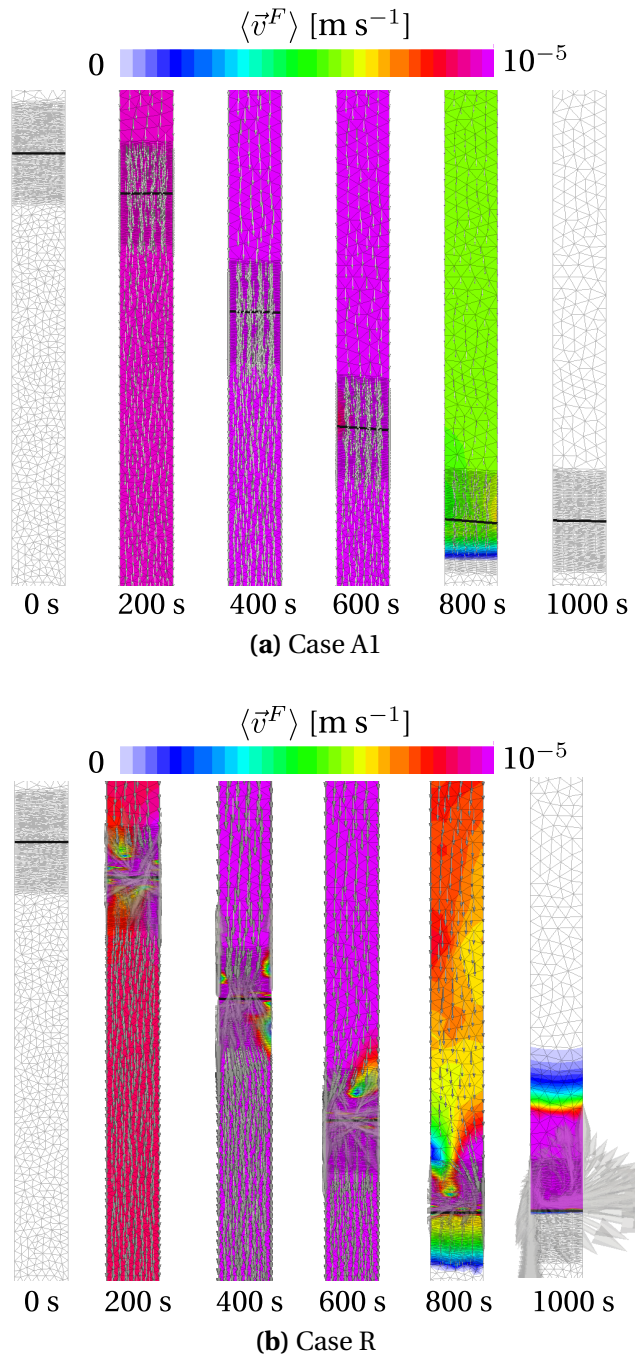


Fig. 5.13 – Comparison of two simulations in several stages of solidification ending shortly after 800 s. The results shows the influence of density and viscosity properties across the level set interface. The plotted field is the average fluid velocity, on which the corresponding nodal vectors are superimposed, pointing towards the solidification front. The thick black line represents the zero iso-value of the distance function. The vectors were made transparent in the transition zone so as not to hide the interface level.

Chapter 5. Macrosegregation with solidification shrinkage

The relative mass change gives us information on the level set transport. As the current case is 1D and phase densities are constant throughout the simulation, mass conservation can be checked by a much simpler than by checking eq. (5.44). Since we know the initial metal's column length, l_0^M , and the expected solidification shrinkage is 7.14 %, we should expect a final length of $l_f^M = (1 - \beta_{SS}) l_0^M = 0.09286$ m. However, this equation is very useful and applicable in 2D and 3D cases of solidification shrinkage.

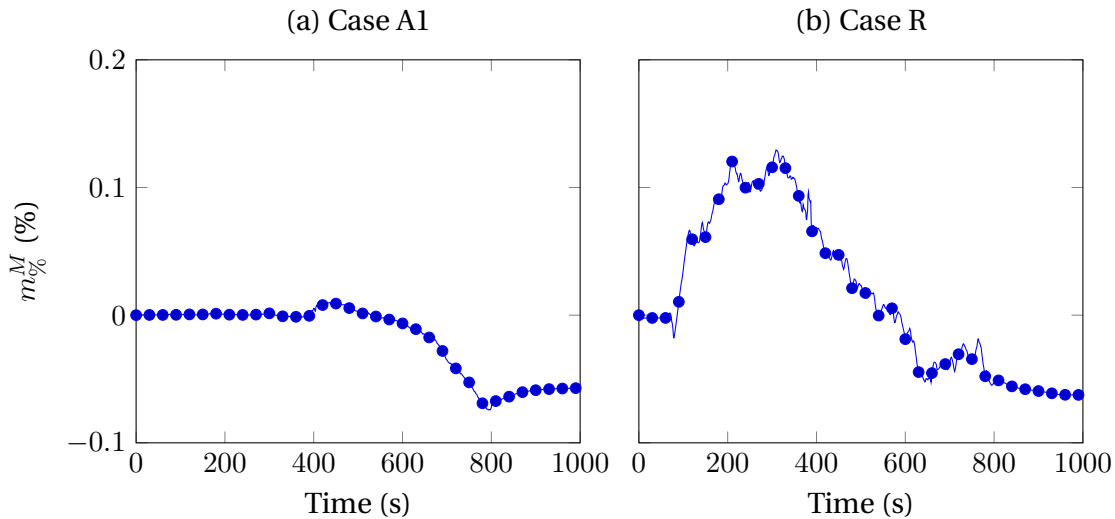


Fig. 5.14 – Variation of the metal's mass versus solidification time in cases A1 and R.

In the previous section, we observed transport problems taking place around 400 s of cooling. Although it was clearly seen in fig. 5.12b, it applies for both cases, whether air properties are equal or different than the liquid's properties across the interface. The mass variation plots in fig. 5.14 confirm these observations. Therefore, we can deduce that regardless of the time step and the level set mixing of properties, transport problems may occur.

The level set method is known to have poor mass conservation properties. However, the mass variation we see in the previous plots is more related to a physical problem: **at which velocity does the interface move?** In our simulations, we systematically considered the Navier-Stokes solution $\langle \vec{v}^F \rangle$, to transport the metal-air interface. This solution is equal to $\langle \vec{v}^l \rangle = g^l \vec{v}^l$ in the metal subdomain. However in reality, between the metal and the air, two interfaces exist: the liquid-air ($l-a$) and solid-air ($s-a$) interfaces, and these interfaces move at different velocities as solidification proceeds. The liquid-air interface exists at early stages of solidification where only liquid is in contact with the air. In later stages, the mushy zone delimited by dendrite tips, reaches the free liquid surface, creating hence these distinct interfaces: a first interface separating

5.6. 1D application: solidification with inverse segregation

interdendritic liquid from the air, and a second interface that separates the dendrites also from the air. The $l-a$ interface is driven by solidification shrinkage and therefore by the real microscopic velocity of the interdendritic liquid, \vec{v}^l . According to [Dantzig et al. \[2009\]](#), this velocity is constant when the solidification shrinkage and the isotherms velocity \vec{v}_T are constant, as states the equation:

$$\vec{v}^l = -\beta_{SS} \vec{v}_T \quad (5.45)$$

As for the $s-a$ interface, its motion is induced by a mechanical deformation of the solid phase either due to thermal shrinkage or external mechanical stresses. The first factor is ubiquitous in any solidification process, while the second factor is process-dependent. In the present work, we remind that the solid phase is assumed fixed and rigid, therefore we consider dendrites to be undeformable during their growth. Unfortunately, this assumption is contradictory with our current situation where the metal keeps shrinking, until an overlap between the level set's diffuse interface and the mushy zone overlap, as shown in [fig. 5.15](#)). At this stage, tracking a single interface induces concept errors, because we are not sure which of the previously mentioned interfaces is being tracked, and hence failing to determine an adequate transport velocity field.

In the light of these facts, we will try to limit as much as possible the interface motion, once the mushy zone has reached the diffuse interface. To do so, we firstly advise to keep a very small thickness interface, in order to delay the previously explained overlap. Moreover, we suggest computing the transport velocity, used in [eq. \(2.59\)](#), at each node j as follows:

$$\vec{v} = \begin{cases} \left\langle \vec{v}^l \right\rangle_j & \text{if } g_j^l > g^{BL} \\ 0 & \text{otherwise} \end{cases} \quad (5.46)$$

where g^{BL} is the threshold for the liquid fraction, below which we consider that the interface should not be transported. [Figure 5.16](#) shows the mass variation for three blocking fractions: 0, 50, 75 and 99 percent. The first value corresponds the case where the Navier-Stokes solution is directly passed to the transport solver. For the last value, the portion of the interface in contact with the low solid fraction part of the mushy zone becomes immobile. It is clearly seen that the consequence on the mass conservation is not very good, as the mass increases up to 3% while the eutectic front is consuming the liquid within the mushy zone, while no further shrinkage is allowed.

In [fig. 5.17](#), we plot again the same curves as in [fig. 5.16](#), but keeping the values of

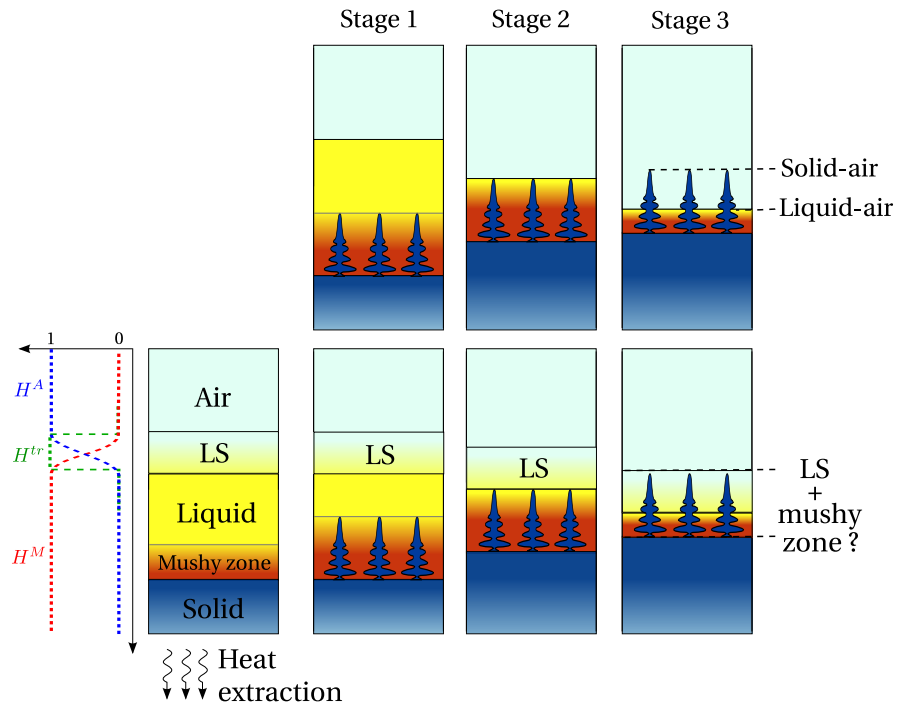


Fig. 5.15 – Schematic describing the physical (first row) and numerical (second row) process of moving an interface between air and metal subdomains, in three intermediate stages of solidification.

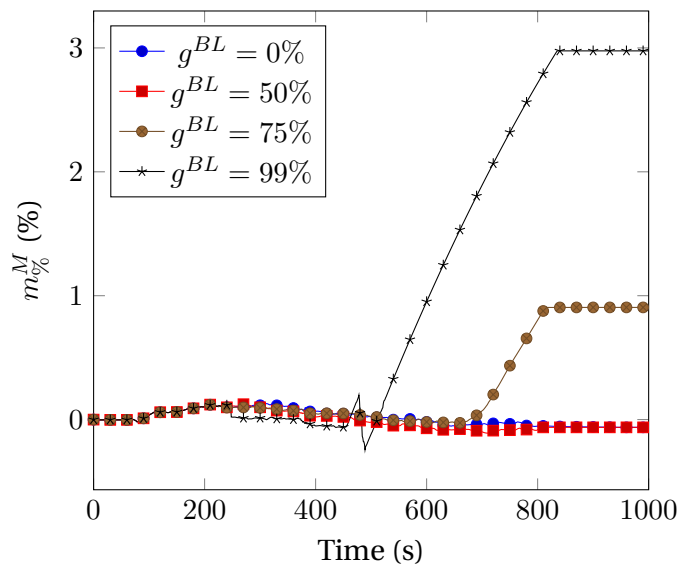


Fig. 5.16 – Relative mass change versus time for different blocking fractions g^{BL} in the transport solver.

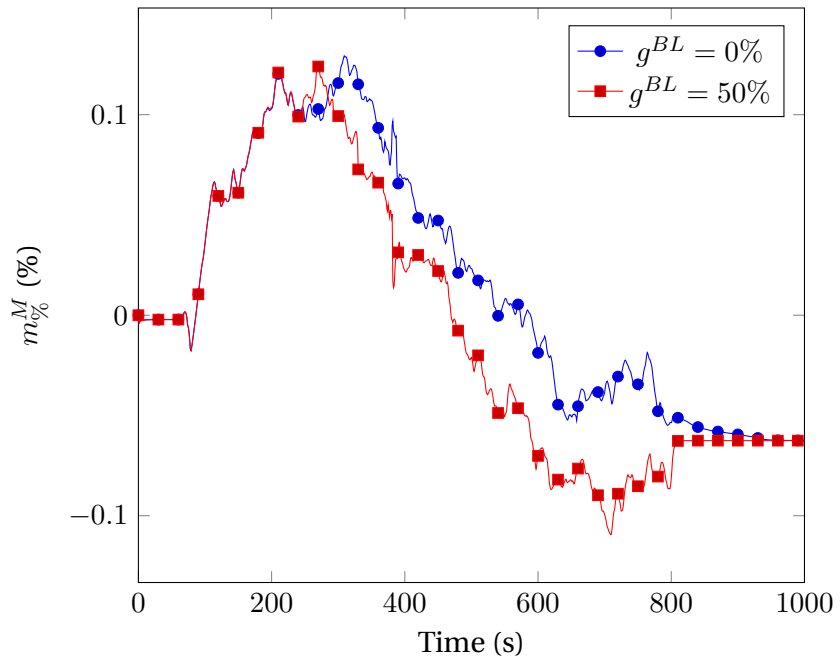


Fig. 5.17 – Relative mass change versus time only for 0% and 50% blocking fractions.

$g^{BL}=0\%$ and $g^{BL}=50\%$.. We notice that both values produce the same results until about 300 s. Then, when the mushy zone reaches the interface region, differences appear as a consequence of the reduced transport for the higher blocking fraction. However, it should be pointed out that the differences between 300 s and 800 s are not important because the permeability predicted by the Carman-Kozeny model, falls to zero quickly for liquid fractions less than about 60%.

In the current application, it is not clear whether the idea of the blocking fraction is useful or not, since the feeding flow occurs in a single direction and solidification takes place far from the interface. Therefore, it is interesting to test again in the coming 2D and 3D applications to see if it yields advantages on the final shape of the interface.

5.6.3 Shrinkage with macrosegregation

in this section, we consider species conservation equation, in addition to energy conservation and fluid momentum conservation equations, used in the previous section to predict solidification shrinkage. The interesting point here is to study the formation of macrosegregation in a one-dimensional configuration and the effect of solidification shrinkage on it. As shown in chapter 2, our approach to solve the energy equation relies on tabulations of various solidification paths. In this case, we will generate a simple tabulation based on a phase diagram with linear liquidus and solidus lines,

Chapter 5. Macrosegregation with solidification shrinkage

whose properties are reminded in [table 5.3](#)

Table 5.3 – Main properties of the linearised phase diagram for Al-Si alloys.

Parameter	Symbol	Value	Unit
Nominal composition	$\langle w \rangle_0$	7	wt.%
Liquidus temperature	T_l	618	°C
Eutectic temperature	T_E	577	°C
Segregation coefficient	k	0.13	—
Liquidus slope	m_l	-6.5	K wt.% ⁻¹

Using the values from [table 5.3](#), a python program generates a *CimLib* compatible tabulation assuming lever rule as microsegregation law, with a 0.1 wt.% step for average composition within an offset of 20% around the nominal value. For temperature, a cooling range between T_E and 630 °C is considered with a step of 1 °C. It is noted that for this application, the phase enthalpies are deduced from constant specific heat of each phase as well as constant latent heat.

In order to understand better the effect of shrinkage combined with macrosegregation, we plot in [fig. 5.18](#), the cooling curves from 4 different simulations:

- Gray curve - case G0: pure diffusion solidification with $\rho^l = \rho^s$ (no level set) used previously in chapter 2 for validation; we use it as a reference case,
- Green curve - case G: convection-diffusion solidification with $\rho^l = \rho^s$ (with level set) at a constant average composition
- Blue curve - case B: convection-diffusion solidification with $\rho^l \neq \rho^s$ (with level set) at a constant average composition; this curve is plotted in [fig. 5.18a](#) and [fig. 5.18b](#),
- Red curve - case R (not to be confused with case R defined in the previous section): convection-diffusion solidification with $\rho^l \neq \rho^s$ (with level set) and macrosegregation.

Shrinkage effect on temperature

If we focus first on [fig. 5.18a](#), we first compare solidification cases G and G0, both with equal phase densities, hence no shrinkage. This first comparison shows that the introduction of the level set method, compared to a monodomain configuration, heats up the overall sample temperature by about 5 °C, causing solidification to finish a few seconds later than predicted in case G0. This is because we set a very high initial temperature in the air, 800 °C, to prevent a brutal diffusive flux that may lead

5.6. 1D application: solidification with inverse segregation

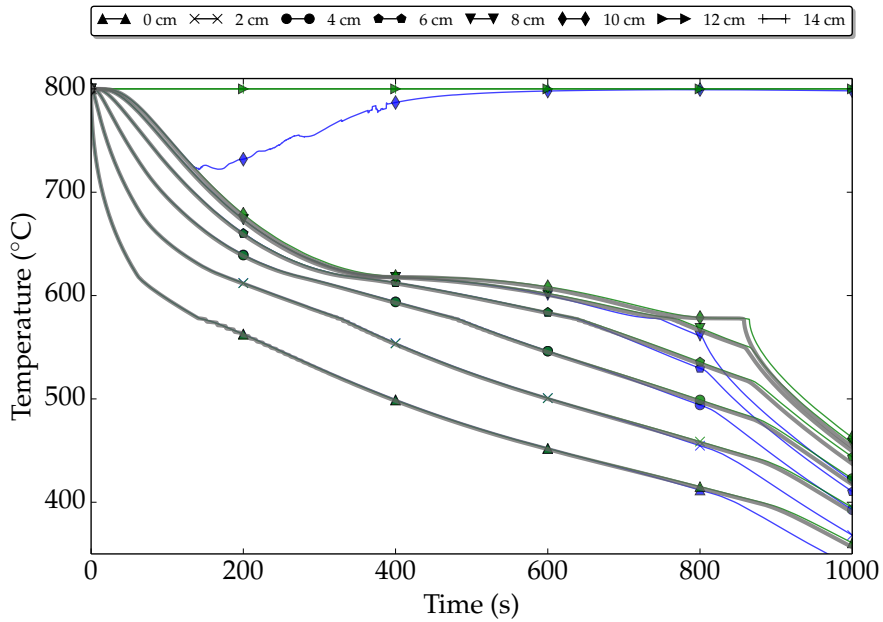
to surface solidification in the metal. As the sample cools down, the air conductivity ($10^{-2} \text{ W m}^{-1} \text{ K}^{-1}$) is not low enough to prevent a small diffusion flux in the metal's direction. However, since in both cases the cooling trend is predicted, we will keep the same thermal diffusion properties in the air, so as not to use unreal conductivity values, but we keep in mind that the current approach delays the solidification.

The second comparison is done between cases G and B, both using the level set approach but only case B considers solidification shrinkage. We notice that blue curve temperature of the sixth eulerian sensor rises steadily from 180 s to 600 s reaching a constant temperature of 800°C , the air's temperature. This rise confirms the metal has shrunk in length (volume in 3D), becoming less than 10 cm, hence replaced by air that entered through the open top boundary. The sensors at 12 cm and 14 cm are not shown in this figure as the simulation done for the pure diffusion without level set, the air subdomain does not exist. Another interesting difference resulting from shrinkage is that solidification ends sooner by about 70 s, compared to the pure diffusion case. As mass is almost perfectly conserved in both cases, cooling flux is the only factor that may accelerate the cooling. The imposed cooling boundary condition is a Fourier-type with the same heat transfer coefficient h_{ext} in both cases. However, a shrinkage flow transports energy in its direction, i.e. towards the solidification front, and thus raising slightly the temperature in regions close to the cool wall. Therefore, the Fourier flux proportional to the temperature difference $(T - T_{\text{ext}})$ increases and the sample solidifies earlier.

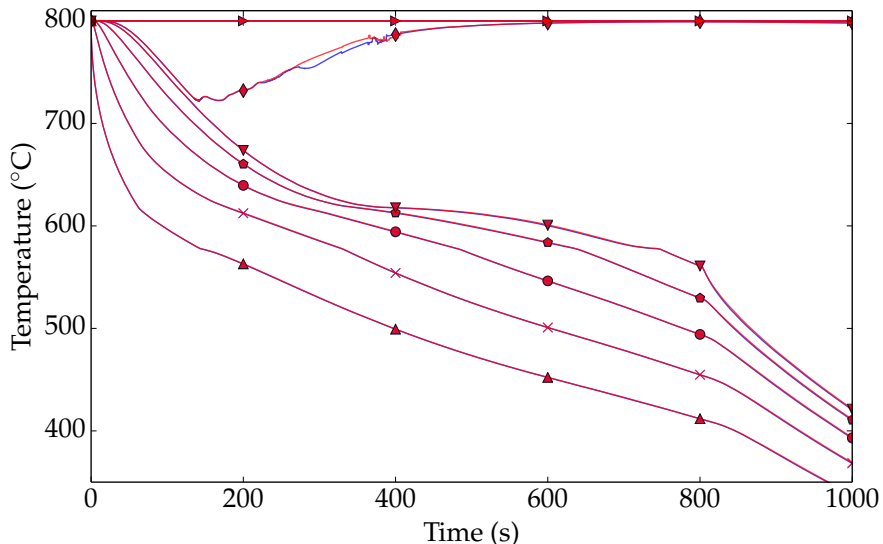
Finally, [fig. 5.18b](#) compares cases B and R, both with unequal phase densities but only predicting macrosegregation in the latter case. Differences are not striking, as temperatures along the metal sample are the same. We spot however a difference at the 10 cm probe, where a slight rise in temperature is observed with respect to the case without macrosegregation.

Shrinkage effect on average composition

[Figure 5.19](#) shows snapshots at different times of the shrinkage flow caused by the density difference between liquid and solid phases. By solid phases, we mean the primary solid phase assumed in a dendritic structure, then the primary and secondary solid phases form together the eutectic that we see starting at 150 s in [fig. 5.19](#). We can see that some solute segregation has already initiated in the mushy zone at 100 s. However, the average composition reaches a positive peak of $\langle w \rangle = \text{Al-7.5 wt.\% Si}$ (CHANGE VALUE ACCORDING TO PLOT) with the initiation and progression of the eutectic front. The sudden transformation of the remaining liquid in the mushy zone into eutectic solid, triggers a local velocity increase (real intrinsic velocity) as each



(a) Solidification shrinkage effect: grey curves correspond to a pure diffusion in a metal monodomain case, green curves consider the latter case but with level set (metal and air subdomains) while blue curves correspond to a shrinkage-driven flow case. All cases are solved without macrosegregation.



(b) Macrosegregation effect: blue curves represent the same simulation corresponding to the shrinkage-driven flow without macrosegregation, while the red curves correspond to a simulation of shrinkage-driven flow with macrosegregation.

Fig. 5.18 – Cooling curves at different fixed positions from 0 to 10 cm (initial metal length) and from 10 cm to 14 cm (initial air length) where we show (a) the effect of solidification shrinkage on temperature history without any macrosegregation then we show (b) the effect of macrosegregation on temperature in the presence of solidification shrinkage.

5.6. 1D application: solidification with inverse segregation

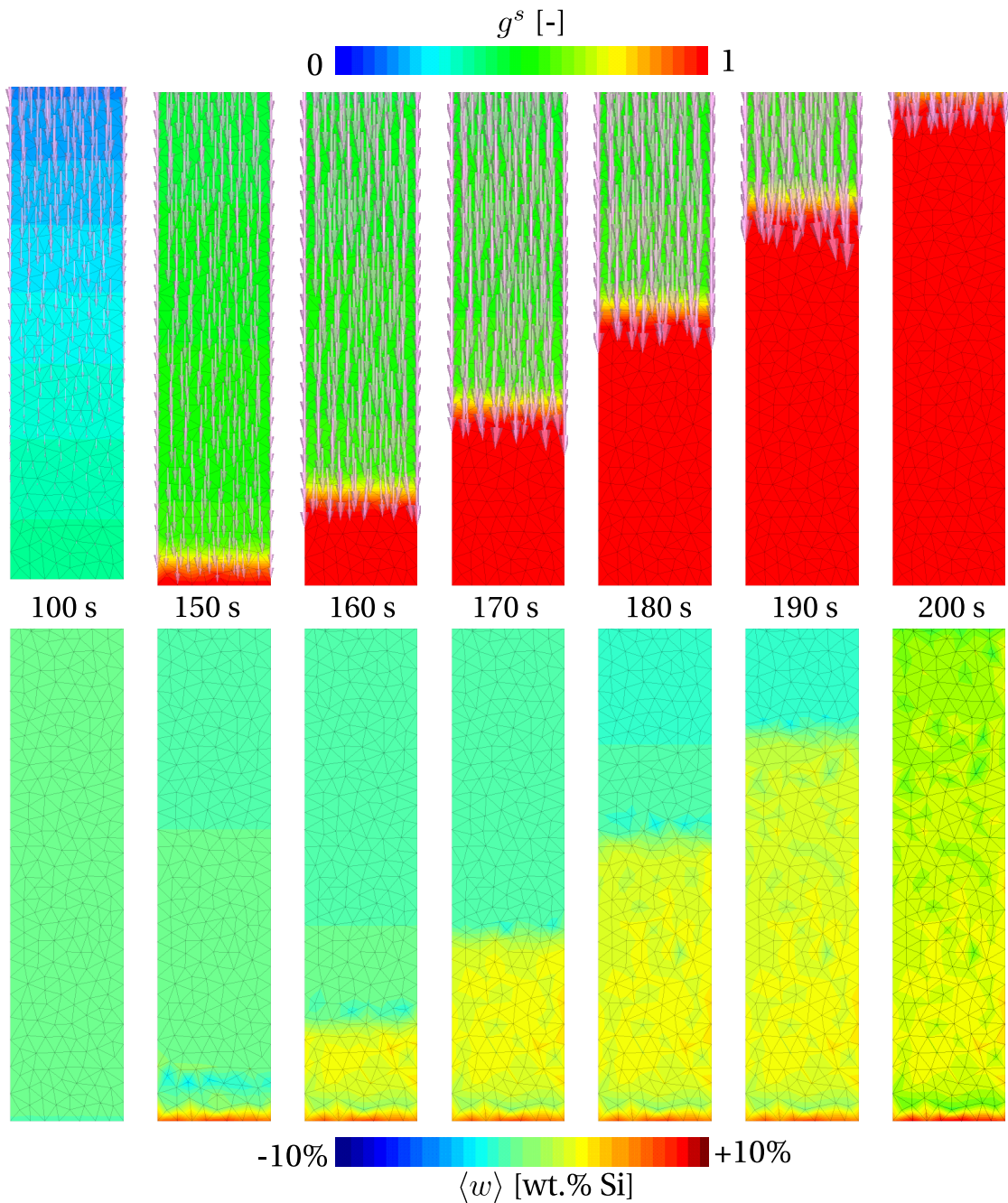


Fig. 5.19 – Zoom on the lower part, approximately 1.5 cm of the alloy close to the cooling boundary condition. The upper row of figures show the evolution of volume solid fraction, when eutectic transformation takes place. The vectors represent the direction of the average velocity field, with a length proportional to the magnitude. The lower row of figures show for the same time increments, the solute redistribution, clearly changing behind the eutectic front.

Chapter 5. Macrosegregation with solidification shrinkage

node's density varies from ρ^l to ρ^s in a single time step, at eutectic temperature. The velocity increase, shown later in [fig. 5.21](#), causes species transport in the opposite direction of solidification, hence solute "freezes" in the eutectic structure leading to positive macrosegregation in the first solidified nodes. This phenomenon is better known as inverse segregation. As the transport continues in the same direction, solute is progressively depleted in the remaining liquid, causing negative macrosegregation at nodes located between 2 cm and 7 cm from the cold wall. [Figure 5.19](#) shows only the first 1.5 cm of the solidifying sample, therefore a complete segregation profile is plotted along the sample length in [fig. 5.20a](#), showing thus the negative macrosegregation as previously explained. However, from 7 cm to the metal-air interface, the average composition rises as clearly shown in [fig. 5.20a](#). This looks more like a numerical instability than a physical rise in concentration. Bearing in mind that a reduced solute diffusion coefficient is imposed in the air subdomain $1.5 \times 10^{-12} \text{ m}^2 \text{ s}^{-1}$ compared to $1.5 \times 10^{-9} \text{ m}^2 \text{ s}^{-1}$ in the metal, we investigate into this instability by proposing two test cases: first, we try to limit the solute advection in the transition zone where flow instabilities may form as seen previously in the segregation-free sample but keeping equal solute diffusion coefficients in both domains to $1.5 \times 10^{-9} \text{ m}^2 \text{ s}^{-1}$, while for the second test case, we combine both low solute diffusion and low solute advection. The average composition results of these two test cases are respectively plotted in [fig. 5.20b](#) and [fig. 5.20c](#). These results (second plot in [fig. 5.20](#)) clearly show that just by reducing solute advection in the mixing zone reduce the amplitude of the composition instability. In contrast, changing solute diffusion properties for the air coupled with reduced solute advection (third plot in [fig. 5.20](#)) offers no further stability in the segregation profile, which should normally stay below the nominal value near the interface.

5.6. 1D application: solidification with inverse segregation

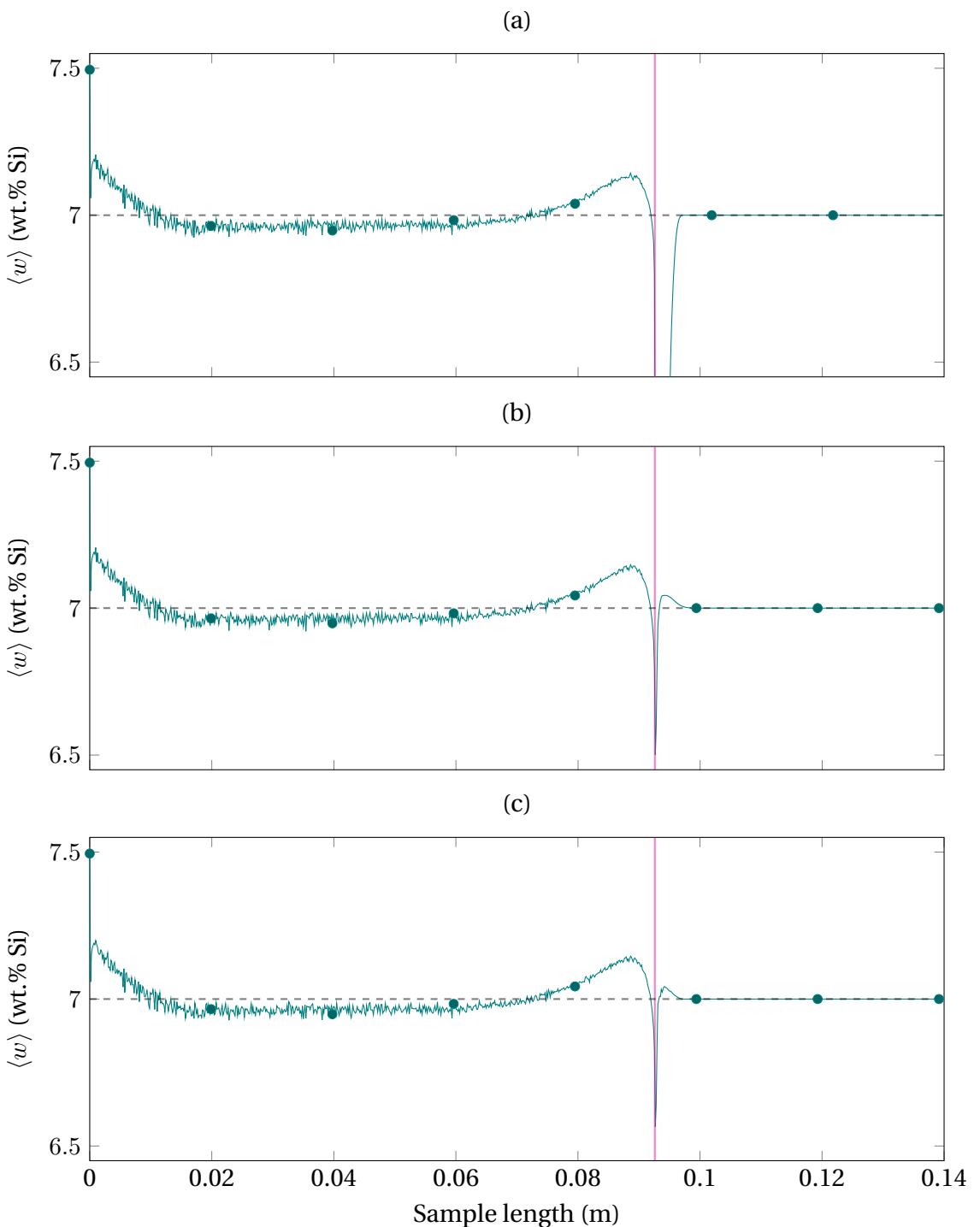


Fig. 5.20 – Plot of the average composition as function of length, along a vertical line passing through the center of the sample at 1000 s, with (a) low solute solute diffusion in the air but unmodified solute advection (minimum composition reaches 2.2 wt.% Si but not shown), (b) reduced solute advection in the level set transition zone or (c) a combination of the previous techniques. The solid magenta line shows the position of the interface after solidification while the black dashed line shows the nominal average composition of the alloy.

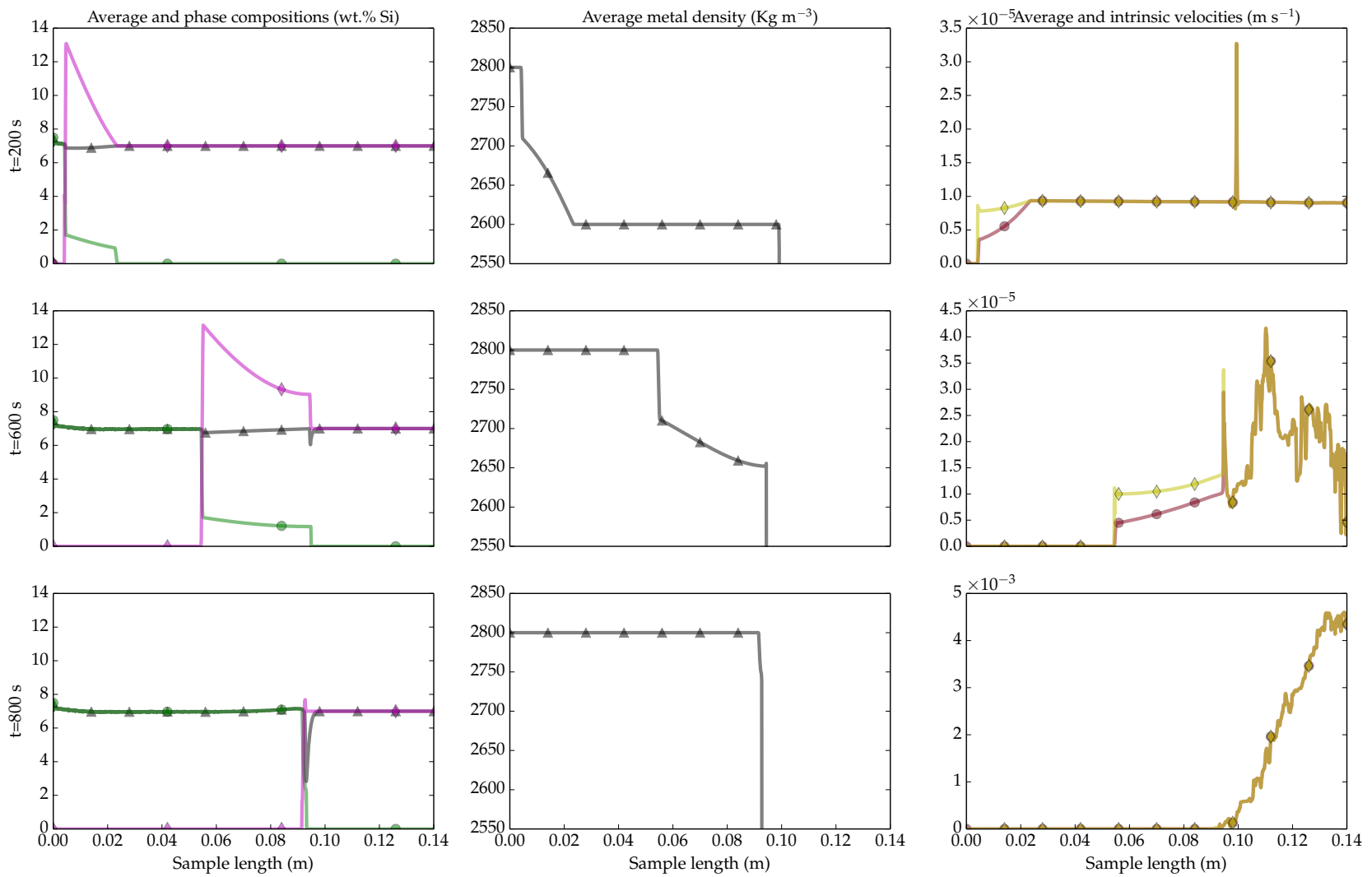


Fig. 5.21 – Group of plots where each row is a given time increment ($t=200\text{ s}$, $t=600\text{ s}$ and $t=800\text{ s}$) of the 1D solidification shrinkage simulation with macrosegregation, while each column one or more physical quantities are plotted along a vertical line passing through the center of the sample. Plots are titled with the corresponding plotted quantities.

5.7. 2D application: controlled solidification benchmark

The plots in [fig. 5.21](#) give important information on the segregation shown in [fig. 5.19](#).
CONTINUE COMMENTING ON [fig. 5.21](#).

Solute mass conservation

Show solute mass conservation with equal or low solute diffusion in air

5.7 2D application: controlled solidification benchmark

This type of applications is very known to the solidification literature and very important in understanding and predicting macrosegregation produced by liquid convection, solid grains settling and volume shrinkage. An molten alloy is put in a rectangular crucible with controlled cooling flux on one or two sides to the crucible. The importance of the experiment lies in the thermal convection forces arising from temperature gradients, but also solutal buoyancy forces arising from liquid concentration gradients. Depending on the density of each chemical species, these convection forces may either be in the same or opposite direction, changing the final macrosegregation pattern. [Hebditch et al. \[1974\]](#) suggested one of the first experiments working on Sn-Zn and Sn-Pb alloys. A part of their results is shown in [fig. 5.22](#). More recently, an experimental benchmark was performed by [Hachani et al. \[2012\]](#) to obtain more accurate composition results with different Sn-Pb and Pb-Sn alloys. In the current section, we are interested in the latter experiment, especially in the prediction of the metal's shrunk surface together with the final macrosegregation.

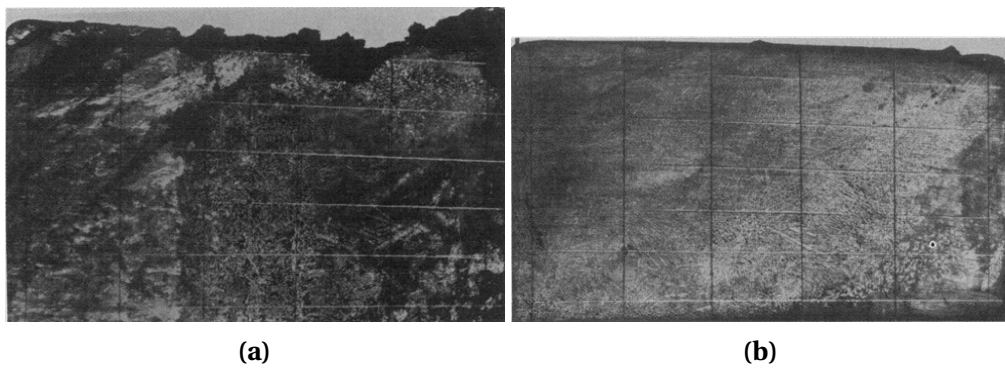


Fig. 5.22 – Final macrosegregation patterns in (a) Sn-5 wt.% Zn and (b) Sn-5 wt.% Pb castings, with a visible sign of volume shrinkage at the top. The rectangular grid on both alloys is used to measure concentration at grid points [[Hebditch et al. 1974](#)].

5.7.1 Absence of convection

We first try to simulate the solidification process by neglecting thermasolutal dependence of phase densities in the Navier-Stokes solver. By doing so, no convection forces should arise during solidification, hence the generated flow is only due to the difference between solid and liquid densities, that is the shrinkage driving force.

5.8 3D application: reduced-gravity solidification

As presented in the introductory chapter, the aim of the CCEMLCC project is to "reach a better understanding of surface defects formed during processing of steels from the liquid state" [Gandin 2014]. Among the several scientific topics being studied, the interaction between skin macrosegregation and thermomechanical deformation is investigated through chill cooling experiments. The idea is to have the molten steel in a containerless environment, which could be done by several ways: electromagnetic levitation, onboard parabolic flights or sounding rockets and finally in a real microgravity context as in the ISS. Heat is extracted from the sample by contact with a ceramic (Si_3N_4) substrate at room temperature (hence the term "chill cooling"), that collides into the alloy at a controlled speed. This contact situation generating high thermal gradients is comparable to casting processes between the molten alloy and the moulds. For ground-based experiments, EML is the exclusive technique to achieve a chill cooling experiment. However, it is technically difficult to achieve levitation without currents in the spherical sample, generated by means of electromagnetic stirring (Lorentz forces) on the one hand but also by thermal convection on the other hand. In reduced-gravity conditions, the dynamics of the phenomena behind fluid motion are less significant. The current application is therefore compared to chill cooling experiments performed in parabolic flights and sounding rockets with reduced gravitational forces ($\|\vec{g}\| \in [10^{-1}; 10^{-5}] \text{ m s}^{-2}$).

5.8.1 Previous work

TEMPUS experiment on parabolic flight

The TEMPUS experiment came as a first alternative for EML experiments in which accurate thermophysical and rheological characterisation were difficult to achieve. The flight consists of several cycles of free fall, a reduced-gravity environment is hence created, allowing to use only a single RF coil to stabilise the position of the droplet, while the substrate comes into contact with the molten sample from above it. An axial

pyrometer measures the sample temperature during the process. Also, a high-speed camera records the solidification process, producing frames as shown in [fig. 5.24](#). This is useful to measure the front growth speed. Each parabola cycle lasts for 50 s, offering an effective low gravity ($\|\vec{g}\| \approx 10^{-1} \text{ m s}^{-2}$) for about 20 s.

TEXUS sounding rocket

TEXUS-46 is the name of the sounding rocket mission that carries the experimental setup, but for simplicity we will refer to the latter as being the TEXUS experiment. The setup is shown in [fig. 5.23](#). The main difference with respect to parabolic flight experiments, TEXUS features solidification in near-zero gravitational fields and for extended periods of time (3 minutes). We do not have an exact measurement of the gravitational field magnitude, but it is several orders less than Earth's gravity magnitude ($\|\vec{g}\| \in [10^{-5}; 10^{-8}] \text{ m s}^{-2}$).

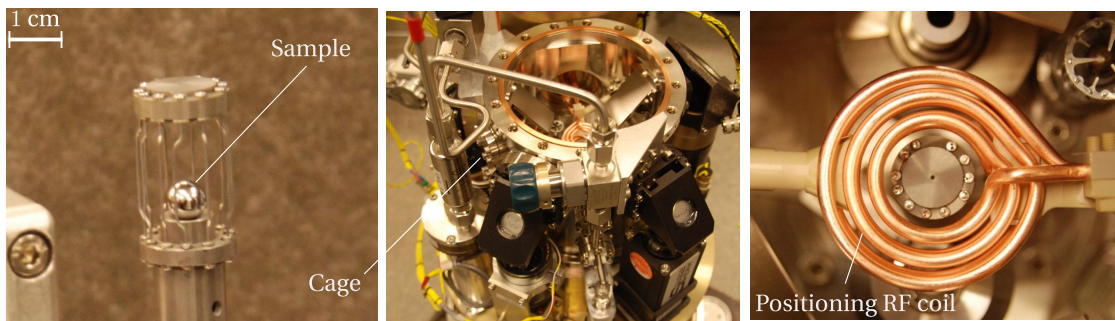


Fig. 5.23 – Three frames describing the experimental setup used to achieve reduced-gravity solidification onboard a sounding rocket flight, showing the initial alloy sample, the cage and the positioning coil. The setup is similar to the one used for TEMPUS experiments.

Numerical contribution

A former numerical contribution was done by [Rivaux \[2011\]](#) at CEMEF as mentioned in the first chapter. His model considered both the steel droplet and the ceramic chill in a Lagrangian formulation, i.e. each object is modelled using a separate deformable mesh. Conservation equations of mass, energy, chemical species and momentum were solved in the metal domain, while the energy conservation was the sole equation solved on the chill mesh. The mechanical problem was divided into two parts: fluid and mechanics and solid mechanics. For the first part, the momentum conservation in the liquid phase was solved using an incompressible P1/P1 SUPG-PSPG formulation of Navier-Stokes equations, i.e. without any contraction for the liquid phase neither

Chapter 5. Macrosegregation with solidification shrinkage

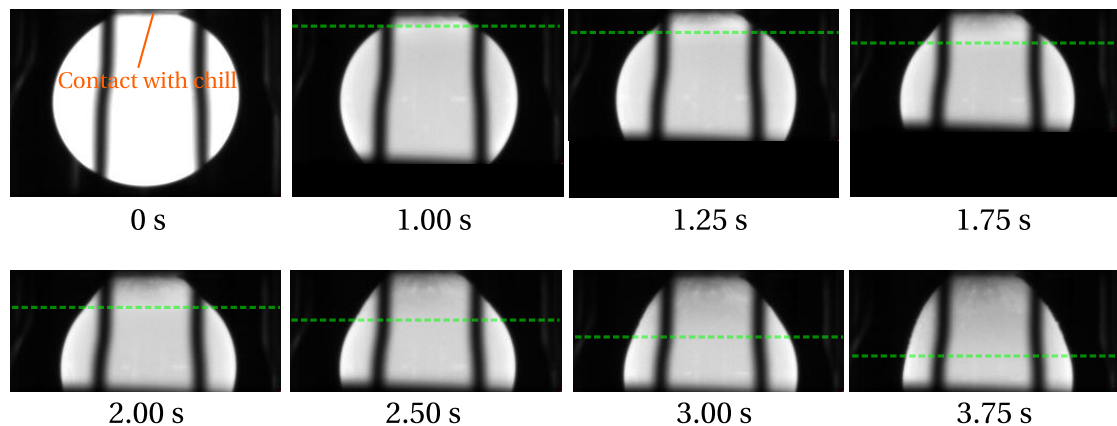


Fig. 5.24 – Image sequence given by a high speed camera onboard a TEMPUS parabolic flight, showing the solidification progress between 0 s (when contact with the chill is initiated) to 3.75 s in a Fe-0.9 wt.% C-0.2 wt.% Si steel droplet. The progress of the solidification front is marked by the green dashed line. In some frames, the droplet is partially hidden by the narrow opening of the sample holder facing the camera.

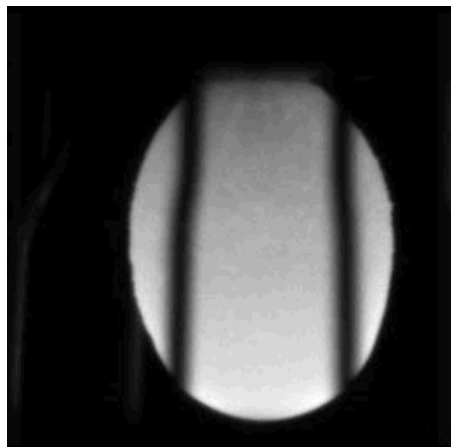


Fig. 5.25 – Camera image from the TEMPUS 2014 experiment, showing the fully solidified droplet with a deformed shape after 10 s.

solidification shrinkage at the solid-liquid interface. The second part, solid mechanics, was solved using P1+/P1 formulation to predict solid deformation caused by the solid's thermal contraction as well as solidification shrinkage, using an elastic-viscoplastic behaviour. The simulation results showed that the total droplet deformation that has been observed in the experiments is not primarily due to solid deformation. The density jump between the solid and liquid phases at the solidification front is actually predominant. High speed camera images endorse this observation, where the droplet underwent a continuous spherical-to-elliptic shape change while the solidification front travelled away from the contact point. Another interesting point to comment is the computation of solidification shrinkage in the solid resolution, although this type of shrinkage does not generate stresses in the solidifying alloy, compared to thermal shrinkage for instance.

5.8.2 Computational configuration

Geometry and mesh

The simulation considers only 1/4 of the droplet-substrate-gas system, given the axial symmetry of the problem. Furthermore, the substrate is implicitly taken into account via a boundary condition, explained in the next section. This is sufficient in the current context, because we are only interested in the energy transfer from the droplet to the substrate.

The steel sample is not perfectly spherical initially as surface oscillations perturb the equilibrium shape. Such perturbations may be attributed to Lorentz forces creating by the positioning coil. The droplet hence is compared to an ellipsoid having a vertical minor axis of 5.68 mm and a horizontal major axis of 6.6 mm, as shown in [fig. 5.26](#). The bottom is a planar surface (diameter of 2 mm, where the contact is initiated). Also in [fig. 5.26](#), the alloy is immersed in a gas medium (argon), such that both subdomains form together 1/4 of a cylinder having 8 mm in radius and 8 mm in height (not fully shown in the figure).

The mesh is then automatically adapted to the moving interface using *Remesh2*. We adopt the same remeshing strategy applied for 1D cases, whereby a fixed mesh size is imposed in the metal subdomain to limit as much as possible information diffusion due to remeshing, this is specially important for the average composition field. The corresponding parameters are given by [table 5.4](#). Remeshing is performed each second.

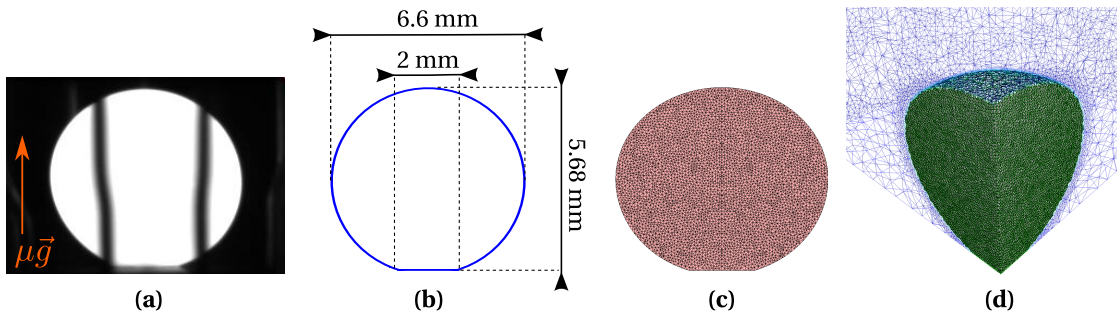


Fig. 5.26 – (a) The camera frame before the onset of solidification gives the essential information to (b) rebuild the droplet geometry then (c) a standalone 2D mesh used to obtain (d) the final immersed 3D mesh.

Table 5.4 – Summary of the different mesh sizes used to generate an adaptive isotropic mesh, along with the level mixing thickness, ε . Refer to section 2.6.2 for the definition of each mesh parameter.

Mesh parameter	Size [m]
ε	1.5×10^{-4}
$h_{\vec{n}} = h_{\vec{\tau}}$	2×10^{-5}
h_M	1×10^{-4}
h_A	6×10^{-4}

Initial and boundary conditions

The thermal boundary conditions are set as follows: Heat loss by radiation is experimentally avoided, therefore it is not considered in our model, hence all boundaries are considered adiabatic, except for the metal-substrate contact area, as previously mentioned. This surface is modelled by a Fourier condition with $T_{\text{ext}}=25^{\circ}\text{C}$ and an effective exchange coefficient h_{ext} of $6 \times 10^4 \text{ W m}^{-2} \text{ K}^{-1}$. The h_{ext} coefficient's value has been determined by running multiple simulations with different values in the aim of predicting a front speed as closer as possible to the experimental measurements plotted in fig. 5.27, as explained in the coming sections.

For the velocity-pressure boundary conditions, fig. 5.29 shows that a no-slip condition is imposed on the droplet-substrate surface, since this area solidifies in the first place without further fluid motion, as shows fig. 5.24. It is noted that the first solidified shell may experimentally deform under thermal contraction stresses, but we do not consider it hereafter. For the rest of the domain, we impose the normal velocity component to zero on both symmetry faces, while keeping free tangential components. The remaining boundaries, namely the top and the outer surface of the argon gas (cylinder generatrix), have free velocity components. However, such condition may

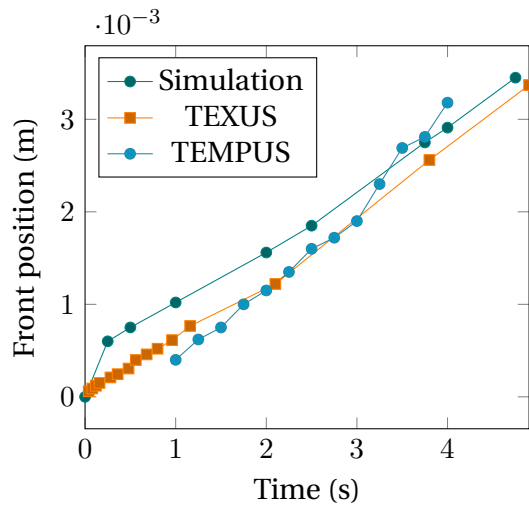


Fig. 5.27 – Position of solidification front versus time for the binary alloy simulation compared to the experimental findings of the TEXUS-46 flight in 2009 and TEMPUS 2014 measurements [Gandin 2014].

cause instability in the level set transport solver, as seen in [fig. 5.28](#). This problem has been reported by [Basset 2006], showing a limitation in the imposed boundary conditions between Navier-Stokes solver and level set transport. Therefore, we limit these instabilities by imposing a no-slip condition, thus allowing the argon to flow in the computational domain through the generatrix. The cylinder height was taken big enough to prevent any flow damping near the droplet's north pole, which may spuriously alter its final shape. The pressure condition for the argon gas is left free for all boundaries. The adopted time step is 0.01 s.

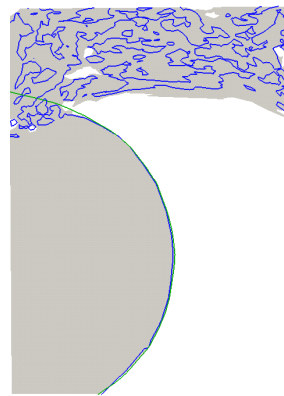


Fig. 5.28 – 2D view showing a transport instability at the top. The green line is the initial metal-gas interface, while the blue line represents the transported zero-level of the distance.

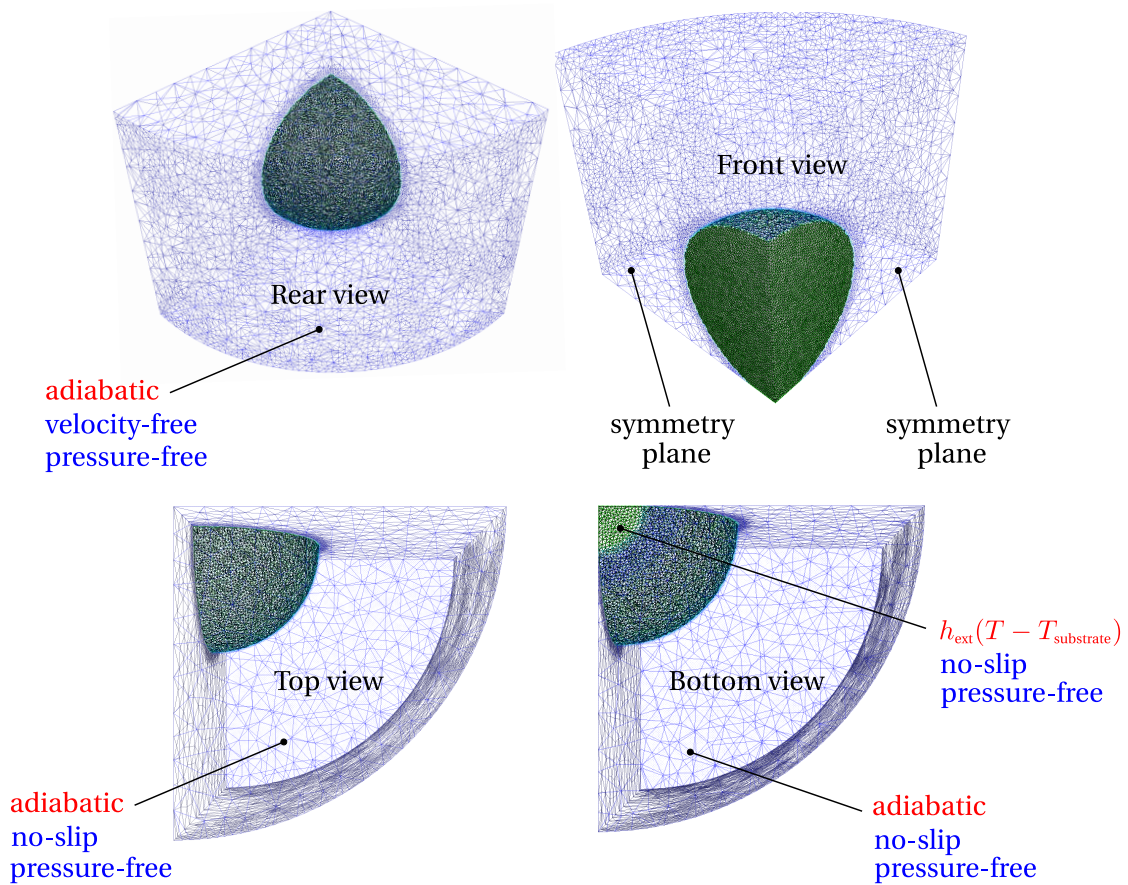


Fig. 5.29 – 3D views showing the thermal (in red) and mechanical (in blue) boundary conditions used in reduced-gravity simulations.

Table 5.5 – Nominal composition (wt.%) of the experimental *b1* steel and its simulation equivalent alloys.

Alloy	C	Si	Mn	Al	S	P
<i>b1</i>	0.105	0.268	0.636	0.0067	0.009	0.0189
Binary <i>b1</i>	0.105	-	-	-	-	-
Ternary <i>b1</i>	0.105	0.268	-	-	-	-
Quaternary <i>b1</i>	0.105	0.268	0.636	-	-	-

Choice of alloy

Various steel grades were considered in the CCEMLCC project. Each grade was assigned to a specific experiment. We limit our study to the steel assigned for TEXUS missions, the grade is designated as "b1" alloy. Its nominal composition is given in [table 5.5](#). As our approach relies on thermodynamic tabulations, we show in the next section that we can take into account the multicomponent alloy to predict segregation, by considering first only one species, hence a binary Fe-C alloy. In a later step, we consider a ternary Fe-C-Si alloy. Finally, we consider a quaternary Fe-C-Mn-Si alloy.

By performing the same reduced-gravity simulation while varying the alloy from binary to quaternary, we can study how the varying solidification paths (as a consequence of macrosegregation) may affect the final droplet shape, as the shrinkage profile is directly related to the solid fraction and its evolution with time.

Parametric study: final shape prediction

In this subsection, we focus on obtaining a comparable final shape of the droplet between the experiment and simulation. To do so, we vary 2 main important parameters: first, the heat transfer coefficient of the metal-substrate contact surface controls the heat extraction and hence the solidification rate. Second parameter is the magnitude of the gravitational field, which has a great influence on the fluid flow inside the molten droplet. The importance of this parametric study is two-fold:

1. in our model, the energy equation solved with the level set methodology considers only heat conduction and advection in the gas subdomain, hence no account for the heat dissipated by radiation (which is an ongoing PhD project at CEMEF). Therefore a trial-and-error strategy is necessary to determine an optimal value of h_{ext} to ensure that the solidification rate is the same as in the experiment,
2. from a hydrodynamics perspective, a containerless molten droplet levitated under reduced-gravity conditions is maintained nearly spherical under the action of surface tension forces. Other forces due to tangential surface tension gradients (Marangoni force) or Lorentz force may also exist. Although possible to implement by the CSF method, accounting numerically for surface tension adds complexity to the model by imposing a time step constraint. However, if we neglect this force, the droplet will tend to collapse if gravity acceleration is fast enough. Consequently, a parametric study helps us determine this gravity threshold, in the absence of surface tension.

A series of test simulations were launched in the aim of getting comparable results with the experiment. Several values of h_{ext} were tested in the interval $[10^2; 10^6]$, while the gravity acceleration influence was tested for values lying in the interval $[10^{-6}; 10^{-2}]$. The best match for the final shape while preserving a front propagation speed close to 0.7 mm s^{-1} , was obtained by setting simultaneously $h_{\text{ext}}=6 \times 10^4 \text{ W m}^{-2} \text{ K}^{-1}$ and $\|\vec{g}\|=5 \times 10^{-5} \text{ m s}^{-2}$. To demonstrate the effect of varying these parameters, we present a parametric study in [table 5.6](#), where only the most relevant cases are studied.

Table 5.6 – Summary of the parametric study for the conductive heat transfer coefficient (H) and the magnitude of the gravity vector (G, not to be confused with thermal gradient). The cases are defined by fixing each parameter to a reference value then varying the latter parameter. The reference values, $H_0=6 \times 10^4$ and $G_0=5 \times 10^{-5}$, ensure a good compromise when compared to the experimental solidification rate and final droplet shape.

Case	$h_{\text{ext}} [\text{W m}^{-2} \text{ K}^{-1}]$	$\ \vec{g}\ [\text{m s}^{-2}]$
H1G0	10^3	5×10^{-5}
H2G0	10^4	5×10^{-5}
H3G0	10^5	5×10^{-5}
H4G0	10^6	5×10^{-5}
H0G1	6×10^4	10^{-3}
H0G2	6×10^4	10^{-4}
H0G3	6×10^4	10^{-5}
H0G4	6×10^4	10^{-6}

Mesh influence

Adaptive iso versus adaptive aniso on mass conservation

5.8.3 Texus binary alloy

Now that the optimal computational configuration is known, we proceed to simulate the solidification of the binary alloy given previously in [table 5.5](#).

5.8.4 Texus ternary alloy

5.8.5 Texus quaternary alloy

5.8.6 TODO

Compare mass conservation between anisotropic mesh (up to 20% loss) and isotropic fixed (up to 3% only)

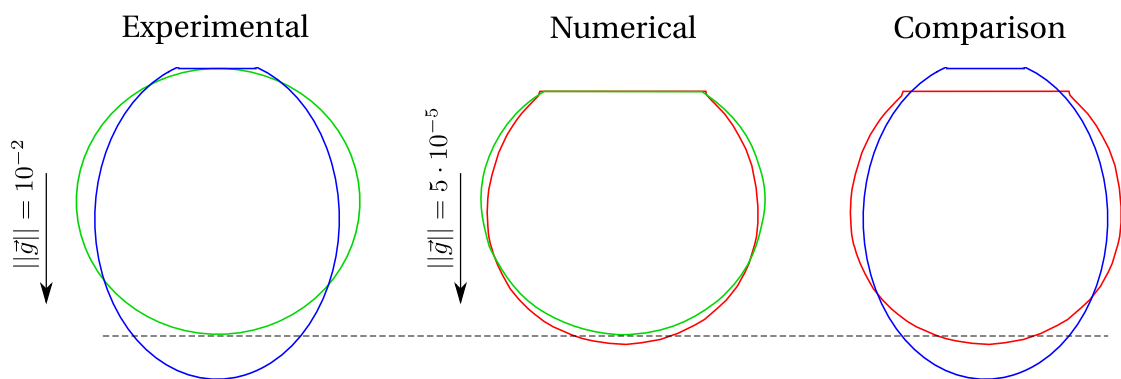


Fig. 5.30 – Comparison between experimental (TEMPUS) and numerical (TEXUS) results showing the initial profile in both cases in green, while the final deformed profile is the blue line obtained experimentally, the red line predicted numerically. The direction of the gravitational fields points downwards, depicted by the arrow (note that the vector length is not scaled to its magnitude).

Compare results of binary, ternary and quaternary tabulations then simplified quaternary

Bibliography

[Andersson et al. 2002]

Andersson, J.-O., Helander, T., Höglund, L., Shi, P., and Sundman, B. (2002). “Thermo-Calc & DICTRA, computational tools for materials science”. *Calphad*, 26 (2), pp. 273–312. URL: <http://www.sciencedirect.com/science/article/pii/S0364591602000378> (cited on pages 62, 65, 87).

[Arnold et al. 1984]

Arnold, D. N., Brezzi, F., and Fortin, M. (1984). “A stable finite element for the stokes equations”. *CALCOLO*, 21 (4), pp. 337–344. URL: <http://link.springer.com/article/10.1007/BF02576171> (cited on page 70).

[Auburtin et al. 2000]

Auburtin, P., Wang, T., Cockcroft, S. L., and Mitchell, A. (2000). “Freckle formation and freckle criterion in superalloy castings”. *Metallurgical and Materials Transactions B*, 31 (4), pp. 801–811. URL: <http://link.springer.com/article/10.1007/s11663-000-0117-9> (cited on page 91).

[Auburtin 1998]

Auburtin, P. B. L. (1998). “Determination of the influence of growth front angle on freckle formation in superalloys”. PhD thesis. Vancouver, BC, Canada: University of British Columbia. URL: https://circle.ubc.ca/bitstream/handle/2429/8676/ubc_1998-345084.pdf?sequence=1 (cited on page 83).

[Babuška 1971]

Babuška, I. (1971). “Error-bounds for finite element method”. *Numerische Mathematik*, 16 (4), pp. 322–333. URL: <http://link.springer.com/article/10.1007/BF02165003> (cited on page 70).

[Barbosa et al. 1991]

Barbosa, H. J. C. and Hughes, T. J. R. (1991). “The finite element method with Lagrange multipliers on the boundary: circumventing the Babuška-Brezzi condition”. *Computer Methods in Applied Mechanics and Engineering*, 85 (1), pp. 109–128. URL: <http://www.sciencedirect.com/science/article/pii/004578259190125P> (cited on page 70).

Bibliography

[Basset 2006]

Basset, O. (2006). "Simulation numérique d'écoulements multi-fluides sur grille de calcul". PhD Thesis. École Nationale Supérieure des Mines de Paris. URL: <https://tel.archives-ouvertes.fr/tel-00376484> (cited on pages 35, 149).

[Beckermann et al. 2000]

Beckermann, C., Gu, J. P., and Boettinger, W. J. (2000). "Development of a freckle predictor via rayleigh number method for single-crystal nickel-base superalloy castings". *Metallurgical and Materials Transactions A*, 31 (10), pp. 2545–2557. URL: <http://link.springer.com/article/10.1007/s11661-000-0199-7> (cited on pages 78, 83).

[Beckermann et al. 1999]

Beckermann, C., Diepers, H. J., Steinbach, I., Karma, A., and Tong, X (1999). "Modeling Melt Convection in Phase-Field Simulations of Solidification". *Journal of Computational Physics*, 154 (2), pp. 468–496. URL: <http://www.sciencedirect.com/science/article/pii/S0021999199963234> (cited on page 30).

[Beckermann 2002]

Beckermann, C. (2002). "Modelling of macrosegregation: applications and future needs". *International Materials Reviews*, 47 (5), pp. 243–261. URL: <http://www.maneyonline.com/doi/abs/10.1179/095066002225006557> (cited on page 9).

[Bellet et al. 2009]

Bellet, M. et al. (2009). "Call for contributions to a numerical benchmark problem for 2D columnar solidification of binary alloys". *International Journal of Thermal Sciences*, 48 (11), pp. 2013–2016. URL: <http://www.sciencedirect.com/science/article/pii/S129007290900177X> (cited on page 44).

[Boden et al. 2008]

Boden, S., Eckert, S., Willers, B., and Gerbeth, G. (2008). "X-Ray Radioscopic Visualization of the Solutal Convection during Solidification of a Ga-30 Wt Pct In Alloy". *Metallurgical and Materials Transactions A*, 39 (3), pp. 613–623. URL: <http://link.springer.com/article/10.1007/s11661-007-9462-5> (cited on page 84).

[Boettinger et al. 2002]

Boettinger, W. J., Warren, J. A., Beckermann, C., and Karma, A. (2002). "Phase-Field Simulation of Solidification1". *Annual Review of Materials Research*, 32 (1), pp. 163–194. URL: <http://dx.doi.org/10.1146/annurev.matsci.32.101901.155803> (cited on page 28).

[Bogno et al. 2013]

Bogno, A., Nguyen-Thi, H., Reinhart, G., Billia, B., and Baruchel, J. (2013). "Growth and interaction of dendritic equiaxed grains: In situ characterization by synchrotron X-ray

radiography". *Acta Materialia*, 61 (4), pp. 1303–1315. URL: <http://www.sciencedirect.com/science/article/pii/S1359645412008026> (cited on page 6).

[Brackbill et al. 1992]

Brackbill, J. U., Kothe, D. B., and Zemach, C (1992). "A continuum method for modeling surface tension". *Journal of Computational Physics*, 100 (2), pp. 335–354. URL: <http://www.sciencedirect.com/science/article/pii/002199919290240Y> (cited on page 30).

[Brezzi 1974]

Brezzi, F. (1974). "On the existence, uniqueness and approximation of saddle-point problems arising from lagrangian multipliers". *ESAIM: Mathematical Modelling and Numerical Analysis - Modélisation Mathématique et Analyse Numérique*, 8 (R2), pp. 129–151. URL: <https://eudml.org/doc/193255> (cited on page 70).

[Brooks et al. 1982]

Brooks, A. N. and Hughes, T. J. R. (1982). "Streamline upwind/Petrov-Galerkin formulations for convection dominated flows with particular emphasis on the incompressible Navier-Stokes equations". *Computer Methods in Applied Mechanics and Engineering*, 32 (1–3), pp. 199–259. URL: <http://www.sciencedirect.com/science/article/pii/0045782582900718> (cited on page 34).

[Buffet et al. 2010]

Buffet, A. et al. (2010). "Measurement of Solute Profiles by Means of Synchrotron X-Ray Radiography during Directional Solidification of Al-4 wt% Cu Alloys". *Materials Science Forum*, 649, pp. 331–336. URL: <http://www.scientific.net/MSF.649.331> (cited on pages 5, 6).

[Carlson et al. 2002]

Carlson, K. D., Lin, Z., Hardin, R. A., and Beckermann, C. (2002). "Modeling Of Porosity Formation And Feeding Flow In Steel Casting". *Proceedings of the 56th SFSA Technical and Operating Conference*. Steel Founders' Society of America. URL: <http://goo.gl/p9ftCp> (cited on page 10).

[Carozzani et al. 2012]

Carozzani, T., Digonnet, H., and Gandin, C.-A. (2012). "3D CAFE modeling of grain structures: application to primary dendritic and secondary eutectic solidification". *Modelling and Simulation in Materials Science and Engineering*, 20 (1), p. 015010. URL: <http://iopscience.iop.org/0965-0393/20/1/015010> (cited on page 92).

[Carozzani et al. 2013]

Carozzani, T. et al. (2013). "Direct Simulation of a Solidification Benchmark Experiment". *Metallurgical and Materials Transactions A*, 44 (2), pp. 873–887. URL: <http://link.springer.com/article/10.1007/s11661-012-1465-1> (cited on pages 44, 58, 60, 92, 93).

Bibliography

[Carozzani et al. 2014]

Carozzani, T., Gandin, C.-A., and Digonnet, H. (2014). “Optimized parallel computing for cellular automaton-finite element modeling of solidification grain structures”. *Modelling and Simulation in Materials Science and Engineering*, 22 (1), p. 015012. URL: <http://iopscience.iop.org/0965-0393/22/1/015012> (cited on page 92).

[Carozzani 2012]

Carozzani, T. (2012). “Développement d’un modèle 3D Automate Cellulaire-Éléments Finis (CAFE) parallèle pour la prédiction de structures de grains lors de la solidification d’alliages métalliques”. PhD Thesis. Ecole Nationale Supérieure des Mines de Paris. URL: <http://pastel.archives-ouvertes.fr/pastel-00803282> (cited on pages 13, 58).

[Chen et al. 1997]

Chen, S., Merriman, B., Osher, S., and Smereka, P. (1997). “A Simple Level Set Method for Solving Stefan Problems”. *Journal of Computational Physics*, 135 (1), pp. 8–29. URL: <http://www.sciencedirect.com/science/article/pii/S0021999197957211> (cited on page 28).

[Chen 2014]

Chen, S. (2014). “Three dimensional Cellular Automaton - Finite Element (CAFE) modeling for the grain structures development in Gas Tungsten / Metal Arc Welding processes”. PhD Thesis. Ecole Nationale Supérieure des Mines de Paris. URL: <https://pastel.archives-ouvertes.fr/pastel-01038028> (cited on page 28).

[Choudhary et al. 2007]

Choudhary, S. K. and Ganguly, S. (2007). “Morphology and Segregation in Continuously Cast High Carbon Steel Billets”. *ISIJ International*, 47 (12), pp. 1759–1766 (cited on page 3).

[Clyne et al. 1981]

Clyne, T. W. and Kurz, W. (1981). “Solute redistribution during solidification with rapid solid state diffusion”. *Metallurgical Transactions A*, 12 (6), pp. 965–971. URL: <http://link.springer.com/article/10.1007/BF02643477> (cited on page 19).

[Combeau et al. 2009]

Combeau, H., Založník, M., Hans, S., and Richy, P. E. (2009). “Prediction of Macrosegregation in Steel Ingots: Influence of the Motion and the Morphology of Equiaxed Grains”. *Metallurgical and Materials Transactions B*, 40 (3), pp. 289–304. URL: <http://link.springer.com/article/10.1007/s11663-008-9178-y> (cited on page 2).

[Combeau et al. 1996]

Combeau, H., Drezet, J.-M., Mo, A., and Rappaz, M. (1996). “Modeling of microsegregation in macrosegregation computations”. *Metallurgical and Materials Transactions A*,

- 27 (8), pp. 2314–2327. URL: <http://link.springer.com/article/10.1007/BF02651886> (cited on page 19).
- [Copley et al. 1970]**
Copley, S. M., Giamei, A. F., Johnson, S. M., and Hornbecker, M. F. (1970). “The origin of freckles in unidirectionally solidified castings”. *Metallurgical Transactions*, 1 (8), pp. 2193–2204. URL: <http://link.springer.com/article/10.1007/BF02643435> (cited on page 81).
- [Courtois et al. 2014]**
Courtois, M., Carin, M., Masson, P. L., Gaied, S., and Balabane, M. (2014). “A complete model of keyhole and melt pool dynamics to analyze instabilities and collapse during laser welding”. *Journal of Laser Applications*, 26 (4), p. 042001. URL: <http://scitation.aip.org/content/lia/journal/jla/26/4/10.2351/1.4886835> (cited on page 29).
- [Coupez 2000]**
Coupez, T. (2000). “Génération de maillage et adaptation de maillage par optimisation locale”. *Revue Européenne des Éléments*, 9 (4), pp. 403–423. URL: <http://www.tandfonline.com/doi/abs/10.1080/12506559.2000.10511454> (cited on page 40).
- [Coupez 1991]**
Coupez, T. (1991). *Grandes transformations et remaillage automatique*. EMP. URL: <http://www.theses.fr/1991ENMP0615> (cited on page 40).
- [Dantzig et al. 2009]**
Dantzig, J. A. and Rappaz, M. (2009). *Solidification*. EPFL Press (cited on pages 6, 10, 19, 20, 22, 24, 48, 133).
- [Darcy 1856]**
Darcy, H. (1856). *Les fontaines publiques de la ville de Dijon : exposition et application des principes à suivre et des formules à employer dans les questions de distribution d'eau*. V. Dalmont (Paris). URL: <http://gallica.bnf.fr/ark:/12148/bpt6k624312> (cited on page 7).
- [Desbiolles et al. 2003]**
Desbiolles, J.-L., Thévoz, P., Rappaz, M., and Stefanescu, D. (2003). “Micro-Macrosegregation Modeling in Casting: A Fully Coupled 3D Model”. TMS Publ., pp. 245–252 (cited on page 83).
- [Desmaison et al. 2014]**
Desmaison, O., Bellet, M., and Guillemot, G. (2014). “A level set approach for the simulation of the multipass hybrid laser/GMA welding process”. *Computational Materials Science*, 91, pp. 240–250. URL: <http://www.sciencedirect.com/science/article/pii/S092702561400278X> (cited on page 28).

Bibliography

[Dijkstra 1959]

Dijkstra, E. W. (1959). "A note on two problems in connexion with graphs". *Numerische Mathematik*, 1 (1), pp. 269–271. URL: <http://link.springer.com/article/10.1007/BF01386390> (cited on page 38).

[DLR 2014]

DLR (2014). *ElectroMagnetic Levitation*. <http://goo.gl/e5JhiA> (cited on page 13).

[Doré et al. 2000]

Doré, X., Combeau, H., and Rappaz, M. (2000). "Modelling of microsegregation in ternary alloys: Application to the solidification of Al–Mg–Si". *Acta Materialia*, 48 (15), pp. 3951–3962. URL: <http://www.sciencedirect.com/science/article/pii/S1359645400001774> (cited on page 44).

[Du et al. 2001]

Du, Q., Li, D., Li, Y., Li, R., and Zhang, P. (2001). "Simulating a double casting technique using level set method". *Computational Materials Science*, 22 (3–4), pp. 200–212. URL: <http://www.sciencedirect.com/science/article/pii/S0927025601001902> (cited on page 28).

[Du et al. 2007]

Du, Q., Eskin, D. G., and Katgerman, L. (2007). "Modeling Macrosegregation during Direct-Chill Casting of Multicomponent Aluminum Alloys". *Metallurgical and Materials Transactions A*, 38 (1), pp. 180–189. URL: <http://link.springer.com/article/10.1007/s11661-006-9042-0> (cited on page 44).

[Easton et al. 2011]

Easton, M., Davidson, C., and StJohn, D. (2011). "Grain Morphology of As-Cast Wrought Aluminium Alloys". *Materials Transactions*, 52 (5), pp. 842–847 (cited on page 6).

[Ettrich et al. 2014]

Ettrich, J. et al. (2014). "Modelling of transient heat conduction with diffuse interface methods". *Modelling and Simulation in Materials Science and Engineering*, 22 (8), p. 085006. URL: <http://iopscience.iop.org/0965-0393/22/8/085006> (cited on page 33).

[Felicelli et al. 1991]

Felicelli, S. D., Heinrich, J. C., and Poirier, D. R. (1991). "Simulation of freckles during vertical solidification of binary alloys". *Metallurgical Transactions B*, 22 (6), pp. 847–859. URL: <http://link.springer.com/article/10.1007/BF02651162> (cited on pages 7, 80, 83).

[Felicelli et al. 1998]

Felicelli, S. D., Poirier, D. R., and Heinrich, J. C. (1998). "Modeling freckle formation in three dimensions during solidification of multicomponent alloys". *Metallurgical and*

Materials Transactions B, 29 (4), pp. 847–855. URL: <http://link.springer.com/article/10.1007/s11663-998-0144-5> (cited on page 83).

[Ferreira et al. 2004]

Ferreira, I. L., Garcia, A., and Nestler, B. (2004). “On macrosegregation in ternary Al–Cu–Si alloys: numerical and experimental analysis”. *Scripta Materialia*, 50 (4), pp. 407–411. URL: <http://www.sciencedirect.com/science/article/pii/S1359646203007346> (cited on page 8).

[Ferreira et al. 2009]

Ferreira, I., Moutinho, D., Gomes, L., Rocha, O., and Garcia, A. (2009). “Modeling and experimental analysis of macrosegregation during transient solidification of a ternary Al–6wt%Cu–1wt%Si alloy”. *Philosophical Magazine Letters*, 89 (12), pp. 769–777. URL: <http://dx.doi.org/10.1080/09500830903292320> (cited on page 8).

[Flemings et al. 1967]

Flemings, M. C. and Nereo, G. E. (1967). “Macrosegregation: Part I”. *Transactions of the Metallurgical Society of AIME*, 239, pp. 1449–1461 (cited on pages 7, 83, 126).

[Flemings et al. 1968a]

Flemings, M. C., Mehrabian, R., and Nereo, G. E. (1968a). “Macrosegregation: Part II”. *Transactions of the Metallurgical Society of AIME*, 242, pp. 41–49 (cited on pages 7, 83).

[Flemings et al. 1968b]

Flemings, M. C. and Nereo, G. E. (1968b). “Macrosegregation: Part III”. *Transactions of the Metallurgical Society of AIME*, 242, pp. 50–55 (cited on pages 7, 83).

[Flemings 1974]

Flemings, M. C. (1974). “Solidification processing”. *Metallurgical Transactions*, 5 (10), pp. 2121–2134. URL: <http://link.springer.com/article/10.1007/BF02643923> (cited on page 3).

[Gada et al. 2009]

Gada, V. H. and Sharma, A. (2009). “On Derivation and Physical Interpretation of Level Set Method-Based Equations for Two-Phase Flow Simulations”. *Numerical Heat Transfer, Part B: Fundamentals*, 56 (4), pp. 307–322. URL: <http://dx.doi.org/10.1080/10407790903388258> (cited on page 30).

[Gandin et al. 2003]

Gandin, C. A., Guillemot, G., Appolaire, B., and Niane, N. T. (2003). “Boundary layer correlation for dendrite tip growth with fluid flow”. *Materials Science and Engineering: A*, 342 (1–2), pp. 44–50. URL: <http://www.sciencedirect.com/science/article/pii/S0921509302002617> (cited on pages 92, 97).

Bibliography

[Gandin 2000]

Gandin, C. A. (2000). "From constrained to unconstrained growth during directional solidification". *Acta Materialia*, 48 (10), pp. 2483–2501. URL: <http://www.sciencedirect.com/science/article/pii/S1359645400000707> (cited on page 54).

[Gandin 2014]

Gandin, C.-A. (2014). *Project ESA-MAP CCEMLCC phase #2 – Final Report* (cited on pages 144, 149).

[Genereux et al. 2000]

Genereux, P. D. and Borg, C. A. (2000). "Characterization of Freckles in a High Strength Wrought Nickel Superalloy". Warrendale, PA: K.A. Green, M. McLean, S. Olson, J.J. Schirra, TMS (The Minerals, Metals, and Materials Society), pp. 19–27. URL: http://www.tms.org/superalloys/10.7449/2000/Superalloys_2000_19_27.pdf (cited on page 83).

[Giamei et al. 1970]

Giamei, A. F. and Kear, B. H. (1970). "On the nature of freckles in nickel base superalloys". *Metallurgical Transactions*, 1 (8), pp. 2185–2192. URL: <http://link.springer.com/article/10.1007/BF02643434> (cited on pages 10, 83).

[Gibou et al. 2003]

Gibou, F., Fedkiw, R., Caflisch, R., and Osher, S. (2003). "A Level Set Approach for the Numerical Simulation of Dendritic Growth". *Journal of Scientific Computing*, 19 (1-3), pp. 183–199. URL: <http://link.springer.com/article/10.1023/A%3A1025399807998> (cited on page 28).

[Gouttebroze 2005]

Gouttebroze, S. (2005). "Modélisation 3d par éléments finis de la macroségrégation lors de la solidification d'alliages binaires". PhD thesis. École Nationale Supérieure des Mines de Paris. URL: <https://pastel.archives-ouvertes.fr/pastel-00001885/document> (cited on pages 13, 76).

[Gruau et al. 2005]

Gruau, C. and Coupez, T. (2005). "3D tetrahedral, unstructured and anisotropic mesh generation with adaptation to natural and multidomain metric". *Computer Methods in Applied Mechanics and Engineering*, Unstructured Mesh Generation 194 (48–49), pp. 4951–4976. URL: <http://www.sciencedirect.com/science/article/pii/S0045782505000745> (cited on page 40).

[Guo et al. 2003]

Guo, J. and Beckermann, C. (2003). "Three-Dimensional Simulation of Freckle Formation During Binary Alloy Solidification: Effect of Mesh Spacing". *Numerical Heat Transfer, Part A: Applications*, 44 (6). <http://dx.doi.org/10.1080/716100512>, pp. 559–576. URL:

<http://user.engineering.uiowa.edu/~becker/documents.dir/GuoFreckle.pdf>
(cited on page 83).

[Hachem et al. 2010]

Hachem, E., Rivaux, B., Kloczko, T., Digonnet, H., and Coupez, T. (2010). "Stabilized finite element method for incompressible flows with high Reynolds number". *Journal of Computational Physics*, 229 (23), pp. 8643–8665. URL: <http://www.sciencedirect.com/science/article/pii/S0021999110004237> (cited on page 72).

[Hachani et al. 2012]

Hachani, L. et al. (2012). "Experimental analysis of the solidification of Sn–3 wt.%Pb alloy under natural convection". *International Journal of Heat and Mass Transfer*, 55 (7–8), pp. 1986–1996. URL: <http://www.sciencedirect.com/science/article/pii/S0017931011007009> (cited on pages 8, 60, 143).

[Hachem 2009]

Hachem, E. (2009). "Stabilized finite element method for heat transfer and turbulent flows inside industrial furnaces". PhD Thesis. École Nationale Supérieure des Mines de Paris. URL: <https://tel.archives-ouvertes.fr/tel-00443532> (cited on page 72).

[Harlow et al. 1965]

Harlow, F. H. and Welch, J. E. (1965). "Numerical Calculation of Time-Dependent Viscous Incompressible Flow of Fluid with Free Surface". *Physics of Fluids (1958-1988)*, 8 (12), pp. 2182–2189. URL: <http://scitation.aip.org/content/aip/journal/pof1/8/12/10.1063/1.1761178> (cited on page 28).

[Hebditch et al. 1974]

Hebditch, D. J. and Hunt, J. D. (1974). "Observations of ingot macrosegregation on model systems". *Metallurgical Transactions*, 5 (7), pp. 1557–1564. URL: <http://link.springer.com/article/10.1007/BF02646326> (cited on pages 8, 60, 143).

[Hirt et al. 1981]

Hirt, C. W and Nichols, B. D (1981). "Volume of fluid (VOF) method for the dynamics of free boundaries". *Journal of Computational Physics*, 39 (1), pp. 201–225. URL: <http://www.sciencedirect.com/science/article/pii/0021999181901455> (cited on page 28).

[Hirt 1971]

Hirt, C. W. (1971). "An arbitrary Lagrangian-Eulerian computing technique". *Proceedings of the Second International Conference on Numerical Methods in Fluid Dynamics*. Ed. by M. Holt. Lecture Notes in Physics 8. Springer Berlin Heidelberg, pp. 350–355. URL: http://link.springer.com/chapter/10.1007/3-540-05407-3_50 (cited on page 27).

[Hysing et al. 2009]

Hysing, S. et al. (2009). "Quantitative benchmark computations of two-dimensional bubble dynamics". *International Journal for Numerical Methods in Fluids*, 60 (11), pp. 1259–

Bibliography

1288. URL: <http://onlinelibrary.wiley.com/doi/10.1002/fld.1934/abstract> (cited on page 35).

[Jannoun 2014]

Jannoun, G. E. (2014). "Space-Time accurate anisotropic adaptation and stabilized finite element methods for the resolution of unsteady CFD problems". PhD thesis. Ecole Nationale Supérieure des Mines de Paris. URL: <https://pastel.archives-ouvertes.fr/tel-01146245/document> (cited on page 40).

[Karagadde et al. 2014]

Karagadde, S., Yuan, L., Shevchenko, N., Eckert, S., and Lee, P. D. (2014). "3-D microstructural model of freckle formation validated using in situ experiments". *Acta Materialia*, 79, pp. 168–180. URL: <http://www.sciencedirect.com/science/article/pii/S1359645414004984> (cited on page 91).

[Karma et al. 1996]

Karma, A. and Rappel, W.-J. (1996). "Phase-field method for computationally efficient modeling of solidification with arbitrary interface kinetics". *Physical Review E*, 53 (4), R3017–R3020. URL: <http://link.aps.org/doi/10.1103/PhysRevE.53.R3017> (cited on page 28).

[Khan et al. 2014]

Khan, M. I., Mostafa, A. O., Aljarrah, M., Essadiqi, E., and Medraj, M. (2014). "Influence of Cooling Rate on Microsegregation Behavior of Magnesium Alloys". *Journal of Materials*, 2014, e657647. URL: <http://www.hindawi.com/journals/jma/2014/657647/abs/> (cited on page 19).

[Kobayashi 1988]

Kobayashi, S. (1988). "Solute redistribution during solidification with diffusion in solid phase: A theoretical analysis". *Journal of Crystal Growth*, 88 (1), pp. 87–96. URL: <http://www.sciencedirect.com/science/article/pii/S0022024898900100> (cited on page 19).

[Kohler 2008]

Kohler, F. (2008). "Peritectic solidification of Cu-Sn alloys: microstructure competition at low speed". PhD Thesis. EPFL (cited on page 83).

[Lee et al. 2002]

Lee, P. D., Atwood, R. C., Dashwood, R. J., and Nagaumi, H. (2002). "Modeling of porosity formation in direct chill cast aluminum–magnesium alloys". *Materials Science and Engineering: A*, 328 (1–2), pp. 213–222. URL: <http://www.sciencedirect.com/science/article/pii/S0921509301016872> (cited on page 91).

[Lesoult et al. 2001]

Lesoult, G. et al. (2001). "Equi-axed growth and related segregations in cast metallic

- alloys". *Science and Technology of Advanced Materials*, 2 (1), p. 285. URL: <http://iopscience.iop.org/1468-6996/2/1/A55> (cited on page 8).
- [Lesoult 2005]**
Lesoult, G. (2005). "Macrosegregation in steel strands and ingots: Characterisation, formation and consequences". *Materials Science and Engineering: A*, International Conference on Advances in Solidification Processes 413–414, pp. 19–29. URL: <http://www.sciencedirect.com/science/article/pii/S0921509305010063> (cited on pages 3, 7).
- [Liu 2005]**
Liu, W. (2005). "Finite Element Modelling of Macrosegregation and Thermomechanical Phenomena in Solidification Processes". PhD thesis. École Nationale Supérieure des Mines de Paris. URL: <http://pastel.archives-ouvertes.fr/pastel-00001339> (cited on pages 13, 76).
- [Maitre 2006]**
Maitre, E. (2006). "Review of numerical methods for free interfaces". Les Houches, France. URL: <http://goo.gl/Re6f3a> (cited on page 28).
- [Martorano et al. 2003]**
Martorano, M. A., Beckermann, C., and Gandin, C.-A. (2003). "A solutal interaction mechanism for the columnar-to-equiaxed transition in alloy solidification". *Metallurgical and Materials Transactions A*, 34 (8), pp. 1657–1674. URL: <http://link.springer.com/article/10.1007/s11661-003-0311-x> (cited on page 19).
- [Mesri et al. 2009]**
Mesri, Y., Digonnet, H., and Coupez, T. (2009). "Advanced parallel computing in material forming with CIMLib". *European Journal of Computational Mechanics/Revue Européenne de Mécanique Numérique*, 18 (7-8), pp. 669–694. URL: <http://www.tandfonline.com/doi/abs/10.3166/ejcm.18.669-694> (cited on page 14).
- [Mosbah 2008]**
Mosbah, S. (2008). "Multiple scales modeling of solidification grain structures and segregation in metallic alloys". PhD thesis. École Nationale Supérieure des Mines de Paris. URL: <https://tel.archives-ouvertes.fr/tel-00349885/document> (cited on page 13).
- [Ni et al. 1991]**
Ni, J. and Beckermann, C. (1991). "A volume-averaged two-phase model for transport phenomena during solidification". *Metallurgical Transactions B*, 22 (3), pp. 349–361. URL: <http://link.springer.com/article/10.1007/BF02651234> (cited on pages 19, 20, 22).
- [Onodera et al. 1959]**
Onodera, S. and Arakida, Y. (1959). "Effect of Gravity on the Macro-Segregation of Larger

Bibliography

Steel Ingots”, pp. 358–368. URL: <http://eprints.nmlindia.org/3079/1/358-368.PDF> (cited on page 108).

[Osher et al. 2003]

Osher, S. and Fedkiw, R. (2003). “Signed Distance Functions”. *Level Set Methods and Dynamic Implicit Surfaces*. Applied Mathematical Sciences 153. Springer New York, pp. 17–22. URL: http://link.springer.com/chapter/10.1007/0-387-22746-6_2 (cited on page 39).

[Osher et al. 1988]

Osher, S. and Sethian, J. A. (1988). “Fronts propagating with curvature-dependent speed: Algorithms based on Hamilton-Jacobi formulations”. *Journal of Computational Physics*, 79 (1), pp. 12–49. URL: <http://www.sciencedirect.com/science/article/pii/0021999188900022> (cited on pages 28, 29).

[Peng et al. 1999]

Peng, D., Merriman, B., Osher, S., Zhao, H., and Kang, M. (1999). “A PDE-Based Fast Local Level Set Method”. *Journal of Computational Physics*, 155 (2), pp. 410–438. URL: <http://www.sciencedirect.com/science/article/pii/S0021999199963453> (cited on pages 31, 37).

[Pickering 2013]

Pickering, E. J. (2013). “Macrosegregation in Steel Ingots: The Applicability of Modelling and Characterisation Techniques”. *ISIJ International*, 53 (6), pp. 935–949 (cited on pages 83, 100).

[Poirier 1987]

Poirier, D. R. (1987). “Permeability for flow of interdendritic liquid in columnar-dendritic alloys”. *Metallurgical Transactions B*, 18 (1), pp. 245–255. URL: <http://link.springer.com/article/10.1007/BF02658450> (cited on page 7).

[Pollock et al. 1996]

Pollock, T. M. and Murphy, W. H. (1996). “The breakdown of single-crystal solidification in high refractory nickel-base alloys”. *Metallurgical and Materials Transactions A*, 27 (4), pp. 1081–1094. URL: <http://link.springer.com/article/10.1007/BF02649777> (cited on page 91).

[Prescott et al. 1994]

Prescott, P. J., Incropera, F. P., and Gaskell, D. R. (1994). “Convective Transport Phenomena and Macrosegregation During Solidification of a Binary Metal Alloy: II—Experiments and Comparisons With Numerical Predictions”. *Journal of Heat Transfer*, 116 (3), pp. 742–749. URL: <http://dx.doi.org/10.1115/1.2910930> (cited on page 8).

[Prosperetti 2002]

Prosperetti, A. (2002). “Navier-Stokes Numerical Algorithms for Free-Surface Flow Com-

putations: An Overview". *Drop-Surface Interactions*. Ed. by M. Rein. CISM International Centre for Mechanical Sciences 456. Springer Vienna, pp. 237–257. URL: http://link.springer.com/chapter/10.1007/978-3-7091-2594-6_8 (cited on page 28).

[Ramirez et al. 2003]

Ramirez, J. C. and Beckermann, C. (2003). "Evaluation of a rayleigh-number-based freckle criterion for Pb-Sn alloys and Ni-base superalloys". *Metallurgical and Materials Transactions A*, 34 (7), pp. 1525–1536. URL: <http://link.springer.com/article/10.1007/s11661-003-0264-0> (cited on pages 7, 83, 84, 91).

[Rappaz et al. 2003]

Rappaz, M., Bellet, M., and Deville, M. (2003). *Numerical Modeling in Materials Science and Engineering*. Springer Series in Computational Mathematics. Springer Berlin Heidelberg (cited on pages 7, 22, 45, 48, 111).

[Rivaux 2011]

Rivaux, B. (2011). "Simulation 3D éléments finis des macroségrégations en peau induites par déformations thermomécaniques lors de la solidification d'alliages métalliques". PhD Thesis. École Nationale Supérieure des Mines de Paris. URL: <http://pastel.archives-ouvertes.fr/pastel-00637168> (cited on pages 13, 58, 72, 76, 145).

[Saad et al. 2015]

Saad, A., Gandin, C.-A., Bellet, M., Shevchenko, N., and Eckert, S. (2015). "Simulation of Channel Segregation during Directional Solidification of In – 75 wt.% Ga – Qualitative Comparison with In-Situ Observations". *accepted in Metallurgical Transactions A*, (cited on page 10).

[Sarazin et al. 1992]

Sarazin, J. R. and Hellawell, A. (1992). "Studies of Channel-Plume Convection during Solidification". *Interactive Dynamics of Convection and Solidification*. Ed. by S. H. Davis, H. E. Huppert, U. Müller, and M. G. Worster. NATO ASI Series 219. Springer Netherlands, pp. 143–145. URL: http://link.springer.com/chapter/10.1007/978-94-011-2809-4_22 (cited on page 10).

[Schneider et al. 1997]

Schneider, M. C., Gu, J. P., Beckermann, C., Boettinger, W. J., and Kattner, U. R. (1997). "Modeling of micro- and macrosegregation and freckle formation in single-crystal nickel-base superalloy directional solidification". *Metallurgical and Materials Transactions A*, 28 (7), pp. 1517–1531. URL: <http://link.springer.com/article/10.1007/s11661-997-0214-3> (cited on pages 10, 83).

[Sethian 1996]

Sethian, J. A. (1996). "A fast marching level set method for monotonically advancing

Bibliography

fronts". *Proceedings of the National Academy of Sciences*, 93 (4), pp. 1591–1595. URL: <http://www.pnas.org/content/93/4/1591> (cited on page 38).

[Shakoor et al. 2015]

Shakoor, M., Scholtes, B., Bouchard, P.-O., and Bernacki, M. (2015). "An efficient and parallel level set reinitialization method - Application to micromechanics and microstructural evolutions". *Applied Mathematical Modelling (submitted)*, (cited on page 39).

[Shah et al. 1989]

Shah, N. A. and Moore, J. J. (1989). "Effect of thermal conditions and alloying constituents (Ni, Cr) on macrosegregation in continuously cast high-carbon (0.8 Pct), low-alloy steel". *Metallurgical Transactions B*, 20 (6), pp. 893–910. URL: <http://link.springer.com/article/10.1007/BF02670195> (cited on page 7).

[Shevchenko et al. 2013]

Shevchenko, N., Boden, S., Gerbeth, G., and Eckert, S. (2013). "Chimney Formation in Solidifying Ga-25wt pct In Alloys Under the Influence of Thermosolutal Melt Convection". *Metallurgical and Materials Transactions A*, 44 (8), pp. 3797–3808. URL: <http://link.springer.com/article/10.1007/s11661-013-1711-1> (cited on pages 83–86, 91, 93).

[Strotos et al. 2008]

Strotos, G., Gavaises, M., Theodorakakos, A., and Bergeles, G. (2008). "Numerical investigation of the cooling effectiveness of a droplet impinging on a heated surface". *International Journal of Heat and Mass Transfer*, 51 (19–20), pp. 4728–4742. URL: <http://www.sciencedirect.com/science/article/pii/S001793100800149X> (cited on page 33).

[Sun et al. 2004]

Sun, Y. and Beckermann, C. (2004). "Diffuse interface modeling of two-phase flows based on averaging: mass and momentum equations". *Physica D: Nonlinear Phenomena*, 198 (3–4), pp. 281–308. URL: <http://www.sciencedirect.com/science/article/pii/S0167278904003689> (cited on page 30).

[Sussman et al. 1994]

Sussman, M., Smereka, P., and Osher, S. (1994). "A Level Set Approach for Computing Solutions to Incompressible Two-Phase Flow". *Journal of Computational Physics*, 114 (1), pp. 146–159. URL: <http://www.sciencedirect.com/science/article/pii/S0021999184711557> (cited on pages 35–37).

[Suzuki et al. 1973]

Suzuki, K. and Miyamoto, T. (1973). "The Mechanism of Formation of the V Segregation in Steel Ingots". *Tetsu-to-Hagane*, 59 (3), pp. 431–445 (cited on page 7).

[Swaminathan. et al. 1993]

Swaminathan., C. R. and Voller, V. R. (1993). "On The Enthalpy Method". *International Journal of Numerical Methods for Heat & Fluid Flow*, 3 (3), pp. 233–244. URL: <http://www.emeraldinsight.com/journals.htm?articleid=1665561&show=abstract> (cited on page 44).

[Süli 2000]

Süli, E. (2000). *Lecture Notes on Finite Element Methods for Partial Differential Equations* (cited on page 48).

[Tan et al. 2007]

Tan, L. and Zabaras, N. (2007). "A level set simulation of dendritic solidification of multi-component alloys". *Journal of Computational Physics*, 221 (1), pp. 9–40. URL: <http://www.sciencedirect.com/science/article/pii/S0021999106002737> (cited on page 28).

[TCBIN 2006]

TCBIN (2006). *TCBIN: TC Binary Solutions Database*. Stockholm, SE (cited on page 87).

[TCFE6 2010]

TCFE6 (2010). *TCFE6: a thermodynamic database for different kinds of steels and Fe-based alloys*. Stockholm, SE. URL: <http://goo.gl/qiD3kE> (cited on pages 62, 65).

[Tezduyar et al. 2000]

Tezduyar, T. E. and Osawa, Y. (2000). "Finite element stabilization parameters computed from element matrices and vectors". *Computer Methods in Applied Mechanics and Engineering*, 190 (3–4), pp. 411–430. URL: <http://www.sciencedirect.com/science/article/pii/S0045782500002115> (cited on page 76).

[Tezduyar et al. 1992]

Tezduyar, T. E., Mittal, S., Ray, S. E., and Shih, R. (1992). "Incompressible flow computations with stabilized bilinear and linear equal-order-interpolation velocity-pressure elements". *Computer Methods in Applied Mechanics and Engineering*, 95 (2), pp. 221–242. URL: <http://www.sciencedirect.com/science/article/pii/0045782592901416> (cited on pages 72, 76).

[Thuinet et al. 2004]

Thuinet, L. and Combeau, H. (2004). "Prediction of macrosegregation during the solidification involving a peritectic transformation for multicomponent steels". *Journal of Materials Science*, 39 (24), pp. 7213–7219. URL: <http://link.springer.com/article/10.1023/B%3AJMSC.0000048734.34597.1e> (cited on page 44).

[Tiller et al. 1953]

Tiller, W. A., Jackson, K. A., Rutter, J. W., and Chalmers, B (1953). "The redistribution of solute atoms during the solidification of metals". *Acta Metallurgica*, 1 (4), pp. 428–437.

Bibliography

URL: <http://www.sciencedirect.com/science/article/pii/0001616053901266>
(cited on page 6).

[Tourret et al. 2009]

Tourret, D. and Gandin, C. A. (2009). "A generalized segregation model for concurrent dendritic, peritectic and eutectic solidification". *Acta Materialia*, 57 (7), pp. 2066–2079.
URL: <http://www.sciencedirect.com/science/article/pii/S1359645409000184>
(cited on page 19).

[Vigneaux 2007]

Vigneaux, P. (2007). "Méthodes Level Set pour des problèmes d'interface en microfluidique". PhD thesis. Université Sciences et Technologies - Bordeaux I. URL: <https://tel.archives-ouvertes.fr/tel-00189409/document> (cited on page 38).

[Ville et al. 2011]

Ville, L., Silva, L., and Coupez, T. (2011). "Convected level set method for the numerical simulation of fluid buckling". *International Journal for Numerical Methods in Fluids*, 66 (3), pp. 324–344. URL: <http://onlinelibrary.wiley.com/doi/10.1002/fld.2259/abstract> (cited on page 37).

[Voller et al. 1989]

Voller, V. R., Brent, A. D., and Prakash, C. (1989). "The modelling of heat, mass and solute transport in solidification systems". *International Journal of Heat and Mass Transfer*, 32 (9), pp. 1719–1731. URL: <http://www.sciencedirect.com/science/article/pii/0017931089900549> (cited on page 114).

[Wanqi et al. 1989]

Wanqi, J. I. E. and Yaohe, Z. (1989). "Formation of hot-top segregation in steel ingot and effect of steel compositions". *Metallurgical Transactions B*, 20 (5), pp. 723–730. URL: <http://link.springer.com/article/10.1007/BF02655930> (cited on page 8).

[Wang et al. 1993]

Wang, C. Y. and Beckermann, C. (1993). "A multiphase solute diffusion model for dendritic alloy solidification". *Metallurgical Transactions A*, 24 (12), pp. 2787–2802. URL: <http://link.springer.com/article/10.1007/BF02659502> (cited on page 19).

[WSA 2014]

WSA (2014). *World Steel Association: Statistics archive*. URL: <http://www.worldsteel.org/statistics/statistics-archive.html> (cited on page 11).

[Xu et al. 1991]

Xu, D. and Li, Q. (1991). "Gravity- and Solidification-Shrinkage-Induced Liquid Flow in a Horizontally Solidified Alloy Ingot". *Numerical Heat Transfer, Part A: Applications*, 20 (2), pp. 203–221. URL: <http://dx.doi.org/10.1080/10407789108944817> (cited on page 7).

Bibliography

[Yuan et al. 2012]

Yuan, L. and Lee, P. D. (2012). "A new mechanism for freckle initiation based on microstructural level simulation". *Acta Materialia*, 60 (12), pp. 4917–4926. URL: <http://www.sciencedirect.com/science/article/pii/S1359645412003205> (cited on page 91).

[Zabaras et al. 2004]

Zabaras, N. and Samanta, D. (2004). "A stabilized volume-averaging finite element method for flow in porous media and binary alloy solidification processes". *International Journal for Numerical Methods in Engineering*, 60 (6), pp. 1103–1138. URL: <http://onlinelibrary.wiley.com/doi/10.1002/nme.998/abstract> (cited on page 76).